Dual-Mode Laser for a Photonic Local Oscillator in the Submillimeter Band and The Molecular Composition of an Oxygen-Rich Asymptotic Giant Branch Star

Dissertation

zur

Erlangung des Doktorgrades (Dr. rer. nat.)

der

Mathematisch-Naturwissenschaftlichen Fakultät

der

Rheinischen Friedrich-Wilhelms-Universität Bonn

vorgelegt von

Hyunjoo Kim

aus

Youngkwanggun/Republik Korea

Bonn, im November 2006

Angefertigt mit Genehmigung der Mathematisch-Naturwissenschaftlichen Fakultät der Rheinischen Friedrich-Wilhelms-Universität Bonn.

1. Referent:	Prof. Dr. Karl M. Menten
2. Referent:	Prof. Dr. Frank Bertoldi
Tag der Promotion:	13. Februar 2007
Publication: 2007	

Abstract

Generation of local oscillator power at Terahertz frequencies with conventional techniques is difficult and expensive. In this thesis, I demonstrate steps towards a THz source using the photonic local oscillator technique for submillimeter astronomy. An LT-GaAs photomixer illuminated by two laser signals generates a beat frequency through photoconductive mixing, equal to the difference of two laser frequencies which can be tuned from a few hundred GHz to around a few THz. To generate two frequencies in the same laser for a photonic LO, I have investigated the use of a Ti:Sapphire ring cavity laser. To generate dual-mode operation in the multi-mode laser, two intracavity solid Fabry-Perot etalons were installed. To characterize the spectral width of the photomixing product, the beat frequency was monitored with a commercial photodetector at 34 GHz. The spectral width of the beat frequency was less than 10 kHz. The output power from the LT-GaAs photomixer was found to increase linearly with the applied bias voltage. Unexpectedly large fluctuations in the output power were measured, due to dual-mode intensity variations from the Ti:Sapphire ring cavity laser. The reasons for these power fluctuations are thermal variations of the resonator cavity, mechanical variations, dust particles, air fluctuations, and mode competition. To reduce these power fluctuations, a power stabilization system using volume holographic gratings (VHGs) was developed, which greatly reduced the power fluctuations.

I helped develop a 460/810 GHz dual-channel receiver, called the First Light APEX Submillimeter Heterodyne instrument (FLASH), for the Atacama Pathfinder Experiment (APEX) telescope located at Llano de Chajnantor in Chile′s Atacama desert. Using FLASH and the APEX-2A receivers, a large number of molecular transitions toward the Long Period Variable (LPV) star IK Tau were observed. Thirty four transitions of 12 molecular species, including maser lines, were detected. To determine the spatial distribution of the ^{12}CO$(3-2)$ emission, mapping observations were performed. Assuming local thermodynamic equilibrium (LTE), the rotational temperatures of molecules and the molecular abundances were obtained. By comparing the abundance of the individual molecules to those reported in the literature, we found an improvement over previously available observed abundances. To constrain the physical conditions in the circumstellar envelope, emission from the SO_2 and CO molecules were modeled using a Monte Carlo method. From the model fits we could estimate the molecular column density and the kinetic temperature of the envelope.

Contents

List of Tables

List of Figures

1. Introduction

1.1. Millimeter and Submillimeter-Wave Astronomy

Astronomical observations in the electromagnetic spectrum are made in the radio, infrared, visible light, ultraviolet, X-ray, and γ-ray bands. For a long time, man was restricted to visible light, but this situation was changed in 1931 when Karl Jansky showed that radiation at a wavelength of 14.6 m, received by him with a direction-sensitive antenna array, was emitted by some extraterrestrial radiation source.

The submillimeter band has recently gained widespread attention in the astronomical community. Spectroscopy at millimeter through far-infrared wavelengths is being used to probe the interstellar medium of our and neighboring galaxies and, moreover, promises to become an essential tool for unraveling the redshift distribution and physical nature of objects even at large look-back times. In particular, the millimeter and submillimeter bands contain spectral and spatial information on the circumstellar envelopes of evolved stars and on the early stages of star formation in gas clouds. One can immediately see the importance of the submillimeter band to star-formation studies and evolved star studies by noting that the temperatures of the dense interstellar gas range from about 10 K in the cooler regions to 100 K or 200 K in the hotter and usually denser parts. The corresponding frequency ($h\nu \sim kT$) range is from about 200 GHz to 4 THz. This same range contains many interesting molecular rotation and atomic fine-structure transitions.

1.2. Receivers at Millimeter and Submillimeter Wavelengths

Millimeter and submillimeter-wave systems are becoming increasingly important in many scientific applications like radio astronomy, remote sensing, plasma diagnostics, radar, and communication systems. In fact, the submillimeter-wave region of the electromagnetic spectrum (300 GHz to 3000 GHz) remains one of the newest and least explored areas of astronomy today. The development of usable detectors goes hand in hand with the astronomical exploration of this region.

Heterodyne conversion uses a local oscillator (LO) to mix a submillimeter or radio frequency (RF) signal to an intermediate frequency (IF). A radio telescope for the millimeter and submillimeter regime consists of an antenna, a receiver system, a spectrometer, controller, and software. Figure 1.1 shows a schematic diagram of the receiving system of a heterodyne receiver. The antenna with its feed collects the submillimeter or radio power from space. The signal is guided into the receiver through a quasi-optical system. Here it is converted into a lower frequency signal (IF) by a mixer, and then it is amplified. Finally, it reaches the spectrometer.

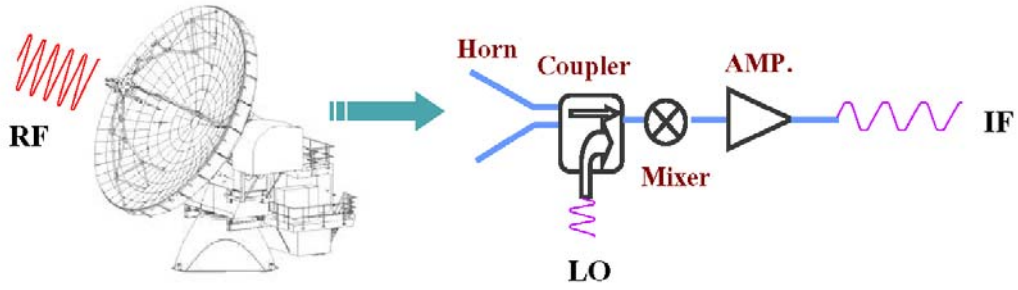

Figure 1.1.: Schematic overview of a heterodyne receiver.

1.3. FLASH Receiver for the APEX Telescope

Observations at millimeter and submillimeter wavelengths do have their limitations. Compared to radio systems, they suffer from greater atmospheric opacity, limiting their range of operation. For instance, ground-based astronomical observations can be carried out only in windows defined by favorable atmospheric transmission. Millimeter and submillimeter waves are attenuated by precipitation, have higher scattering losses, and are absorbed in the atmosphere by water vapor and oxygen. For these reasons, submillimeter telescopes are placed at high altitude sites with dry air. The best places for submillimeter telescopes are known to be Mauna Kea in Hawaii, the Atacama desert in Chile, and the South Pole.

The Max-Planck Institute for Radioastronomy collaborated with the European Southern Observatory (ESO) and the Onsala Space Observatory (OSO) to build the Atacama Pathfinder Experiment (APEX) telescope, placed on Llano de Chajnantor in Chile's Atacama desert (see figure 1.2). Since 2003, we have been developing the first-light APEX submillimeter heterodyne instrument (FLASH) (Heyminck et al. 2006). FLASH is a dual-frequency, closed-cycle cooled heterodyne receiver, operating in the 460 GHz and the 810 GHz atmospheric window. For a dual-frequency receiver, the main requirement is to optimally match both frequency channels to the telescope simultaneously. The optics of both channels follows a Gaussian telescope setup, which provides both linear scaling of the beam size and frequency-independent waist position. The LO signal is provided by two Gunn-diode oscillators driven multiplier chains. The LO beams are guided to the SIS mixers through the LO guiding optics (see figure 1.3). The mixers are fixed-tuned double-side band (DSB) superconductor insulator superconductor (SIS) mixers. Typical receiver noise temperatures are 200 K at 460 GHz and 400 K at 810 GHz, respectively.

1.4. Photonic Local Oscillator

Millimeter and submillimeter-wave heterodyne mixers based on SIS junctions have used as an LO source a combination of solid-state oscillators, such as Gunn diodes and YIG oscillators that can deliver power levels in excess of 1 mW up to 350 GHz. Improvements of several technologies necessary for the fabrication of backward-wave oscillators (BWO) have resulted in considerable improvements in the characteristics of these monochromatic sources. These tubes, which offer a 20 %

Figure 1.2.: The APEX 12 m telescope on the Llano de Chajnantor plateau in Chile.

tuning range at 500 GHz, are currently available and can deliver 25 mW of power at the fundamental frequency. Tubes with equivalent capabilities at 1 THz are presently under construction. These LO sources (Gunn oscillators, YIG oscillators, and BWO oscillators) have a limited frequency coverage, especially at submillimeter wavelength where a broad frequency coverage is highly prized for submillimeter-wave SIS receivers in the radio telescopes. Recently, THz photomixers have generated a difference frequency of two lasers at millimeter and submillimeter wavelength by photoconductive mixing. Photomixers are a promising source of coherent power generation at THz frequencies. Low-temperature growth (LTG or LT) GaAs is used as a photomixer by focusing laser beams on an array of submicron interdigitated electrodes on the top surface. The electrodes are biased at a large potential and are coupled directly to a spiral or slot antenna (Carlstrom & Zmuidzinas 1996), which radiates the continuous wave (CW) mixing product.

Optical Source : the Laser

Photomixing uses a coherent source of near-infrared radiation (NIR). Sources such as two NIR lasers are tuned to frequencies that differ by an amount in the THz region. Optical sources often considered for the photomixer are the semiconductor diode laser, gas laser, and solid-state laser. Optical sources for the photomixer should be frequency stabilized and have narrow spectral width. To adopt the photonic LO in the submillimeter astronomical receivers, the lasers should have the following characteristic:

(a) wide tunability

(b) high power

(c) narrow spectral linewidth

(d) high frequency stability.

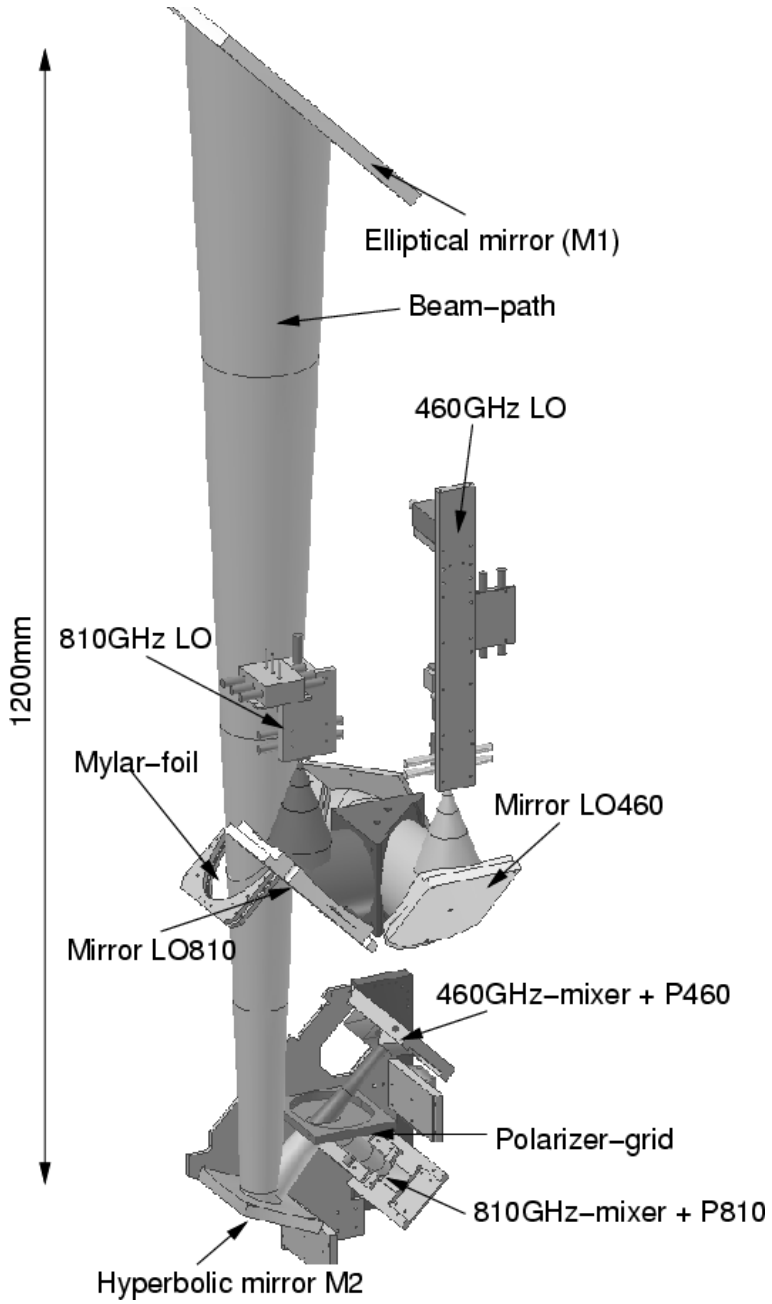

Figure 1.3.: Schematics of the FLASH optics. The telescope signal is re-imaged by the mirrors M1 and M2, forming a Gaussian telescope. Between these mirrors, it is combined with the LO-signals. The signal is then split by a polarizer and finally matched by individual parabolic mirrors to the mixer-horn antennas (Heyminck et al. 2006).

1.5. Motivation

1.5.1. Dual-Mode Operation using the Ti:Sapphire Laser for the Photomixing

Our THz-laboratory is experimenting with several NIR laser sources, mainly with tunable semiconductor diode lasers. To obtain enough power, optical amplifiers are applied and then one has to deal with the usual instabilities from unwanted optical feedback.

Another possibility is the application of a Ti:Sapphire laser pumped by, for example, an Argon or a doubled $Nd : YVO_4$ laser. This laser type belongs to the vibronic lasers involving a spectrally very broad and high-gain laser medium based an fluorescence. The Ti:Sapphire laser is commercially available in a ring resonator configuration, which makes it insensitive to any optical feedback disturbance, both in the pump radiation path as well as in the output path. In this research, it has been proven that a Ti:Sapphire laser can run at two frequencies at the same time with enough power for our present LT-GaAs photomixer, without an additional optical amplifier. However, the peak intensities of the two modes change continuously due to mode competition, air fluctuations, thermal fluctuations, and mechanical vibrations. For this reason, power stabilization using volume holographic gratings (VHGs) was implemented.

In section 2, the Ti:Sapphire laser is characterized and the dual-mode operation using the Ti:Sapphire laser described; in section 3 the monitoring of the mixing product is presented; in section 4 the output power generated in the LT-GaAs photomixer, and in section 5 the dual-mode power stabilization scheme are presented.

1.5.2. Molecular Line Observation by using the FLASH and APEX-2A Receivers

Since 2003 I have participated in building the dual frequency channel receiver, FLASH, operating in the 460 GHz and the 810 GHz atmospheric windows for APEX. Commissioning of APEX began in mid 2004, and regular science operation has been performed since July 2005.

Molecular lines are probes of the physical and chemical conditions in the interstellar clouds, protostellar stellar envelopes, circumstellar shells around Asymptotic Giant Branch (AGB) stars, and photon-dominated regions (e.g., Wyrowski et al. (1997)). To know the molecular composition of the circumstellar envelope around the AGB star IK Tau, many molecular species were observed at several frequencies using the FLASH and the APEX-2A receivers. In section 6, I present the observational results and describe the scientific analysis.

2. The Characterization of the Ti:Sapphire Ring Cavity Laser and the Dual-Mode Laser

2.1. Introduction

The prospect of using photonic techniques to generate GHz and THz frequency radiation sources by mixing the signals from two near infrared lasers on a suitable photomixer is currently often discussed in the literature. These frequency sources find their potential applications in telecommunications, luggage screening, tomography, and in astronomy among others. In astronomy they can be used as widely tunable local oscillator sources in heterodyne receivers. But this application requires, unlike other applications, an outstanding stability of power output and frequency. Among the available near infrared lasers are semiconductor lasers and solid state lasers that operate either in the spectral areas around 800 nm or around 1500 nm. Which region is chosen depends on the cut-off frequency of the photonic material of the photomixer. Presently, we are working on GaAs type mixers and, hence, on lasers in the 800 nm region. Here the Ti:Sapphire laser is a powerful alternative to the semiconductor lasers and amplifiers we have been using so far. The Ti:Sapphire laser has a wide gain profile between roughly 660 nm and 1180 nm with output power up to several hundred mW.

Tunable single-mode lasers are widely used in spectroscopic, optical, and quantum-optics experiments. In the visible and near infrared spectral ranges, the Ti:Sapphire lasers are commercially available (Zimmermann et al. 1995). The Ti:Sapphire ring cavity laser is well known for its broadband gain profile and can be widely tuned by frequency-tuning components such as birefringent filters and solid or air-spaced etalons. In the case of a long resonator laser, it has a narrowed spectral width and the mode spacing is close. For example, the Coherent 899-01 CW Ti:Sapphire ring cavity laser with birefringent filter has a 1.6 m cavity length and $\sim$ 184 MHz mode spacing. For single-mode operation, an additional frequency filtering component such as an etalon is required because the birefringent filter has a $\sim$ 1.7 THz FWHM passband. With such a broad passband, the optical gain competition phenomena can suppress most modes (Reilly et al. 2002).

The main purpose of the work presented here was to investigate the possibility to take advantage of the properties of the Ti:Sapphire laser in order to generate two frequencies in the same laser. This technique can optimize the frequency stability of the difference frequency because of the common-mode rejection (Tani et al. 2004) as mechanical, atmospheric, and temperature variations are practically the same for both laser frequencies.

In the next schemes, it is experimentally demonstrated that this can be realized by mode filtering of two closely spaced modes in the ring cavity.

2.2. Theory of the Laser

The LASER (Light Amplification by Stimulated Emission of Radiation) is a device that generates and/or amplifies electromagnetic radiation such as light. The laser performs light amplification by stimulated emission and multiple reflection of light between mirrors. Lasers are sources of highly directional, monochromatic, and coherent light.

A laser essentially consists of three components:

1) The gain medium that amplifies an incoming electromagnetic wave. The gain medium can be a solid, a semiconductor, a liquid, a gaseous medium, or even a relativistic electron beam. The medium determines the spectral range where the laser is active.

2) The pump source that excites the gain medium into higher quantum-mechanical levels in order to achieve the population inversion.

3) The optical resonator or cavity, which is mostly composed of two opposite mirrors with the gain medium in-between. The resonator stores part of the induced emission that is concentrated within a few resonator modes. In the case of a laser oscillator, the laser photons which are emitted by the pumped gain medium can pass repeatedly through the cavity. On each pass, the emission of other photons is stimulated in a way that the stimulating photon and the emitted photon have identical phases. This leads to amplified coherent radiation and explains the highly directional properties of laser beams (Demtröder 1996).

The wavelength where the laser is active is mainly determined by the gain profile of the laser medium and the resonance conditions in the laser cavity. Figure 2.1 shows how the gain profile and the mode spacing of the cavity can look like for a typical laser. In the simple case of a standing wave resonator with flat mirrors, the mode spacing will be

$$\Delta\nu = \frac{c}{2nd} \tag{2.1}$$

where c is the speed of light in free space, n is the refractive index of the medium between the mirrors, and d is the length of the cavity. Note that d may consists of a series of different media with different refractive index.

2.2.1. Coherence Time

The coherence time quantifies the degree of temporal coherence of light. Coherence theory defines it as the time over which the field correlation function decays. This correlation (or coherence) function is (RPPhotonics 2006).

$$g(\tau) = \frac{< E^*(t)E(t+\tau) >}{< E^*(t)E(t) >} \tag{2.2}$$

where $E(t)$ is the complex electric field at a certain time. This function is 1 for $\tau = 0$ and usually decays monotonically for larger time delays τ. For an arbitrary shape of this function, the coherence time can be defined by

$$\tau_{\text{coh}} = \int_{-\infty}^{+\infty} |g(\tau)|^2 d\tau \tag{2.3}$$

The stationary electromagnetic wave with coherence time τ_{coh} has a bandwidth $\Delta\nu_{\text{FWHM}} \cong 1/\tau_{\text{coh}}$ (Cerullo & Nisoli 2001). The width of each peak frequency is exactly the reciprocal of the coherence

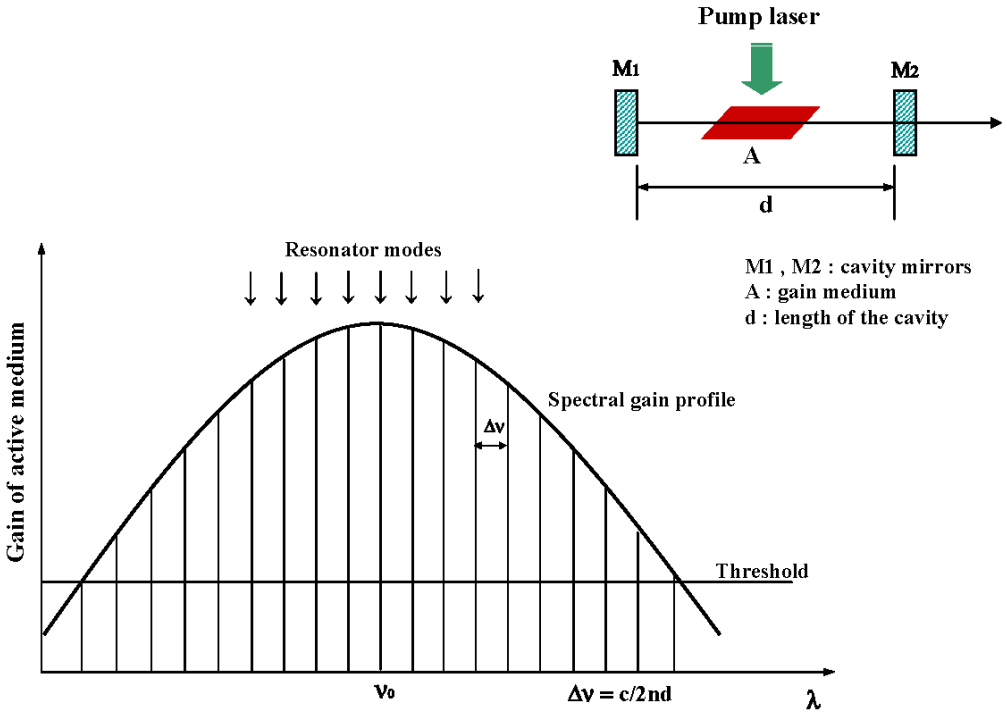

Figure 2.1.: Gain profile of the laser transition with resonator eigenfrequencies of axial modes. Modified from Demtröder (1996).

time (Yang et al. 2006). The coherence length is related to the coherence time τ_{coh} by $L_{\mathrm{coh}} = c\tau_{\mathrm{coh}}$ (Davis 1996).

Therefore, the coherence time and the coherence length are described as:

$$\tau_{\mathrm{coh}} = \frac{1}{\Delta\nu_{\mathrm{FWHM}}} \tag{2.4}$$

$$L_{\mathrm{coh}} = c\tau_{\mathrm{coh}} = \frac{c}{\Delta\nu_{\mathrm{FWHM}}}. \tag{2.5}$$

2.2.2. Laser Amplification

The internal spontaneous emission from the gain medium is regeneratively amplified inside the ring cavity and transmitted through the output mirror (or coupler). For example, the Ti:Sapphire ring cavity laser has an output mirror with 97 % reflectivity. The magnitude of the round-trip gain in the cavity and laser linewidth depends on the cavity mirror reflectivity. The round-trip time is given by

$$t_{\mathrm{rt}} = \frac{2L}{c} \tag{2.6}$$

where L is cavity length and c is the speed of light in free space.

Like all laser oscillators, the Ti:Sapphire laser emission is based on regenerative feedback. A representative configuration (as shown in figure 2.2) of the regenerative amplifier is comprised of two mirrors with a gain medium in-between them. One of the mirrors is partly reflective and serves as the output mirror. Part of the photons produced in the gain medium are reflected back and forth between the mirrors. The gain medium will amplify the number of photons at each passage.

The regenerative gain formula can be written as (Siegman 1986)

$$G = -\frac{T_1 T_2..}{\sqrt{r_1 r_2..}} \times \frac{\sqrt{g_{\mathrm{rt}}(\omega)}}{1 - g_{\mathrm{rt}}(\omega)}. \tag{2.7}$$

where $g_{\mathrm{rt}}(\omega)$ is the round-trip gain inside the cavity, T_1 and T_2 are the transmitted intensity from the resonator mirrors as losses, and r_1 and r_2 are the reflectivities of the resonator mirrors. In general, the gain of regenerative amplification is proportionally increased with the mirror reflectivity of the resonator, especially the output mirror, and the round-trip cavity length.

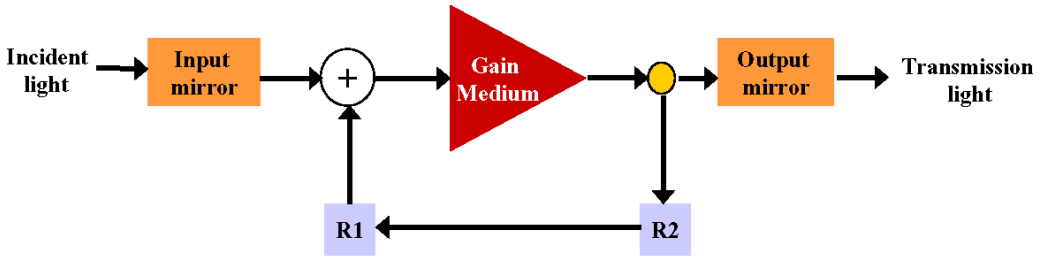

Figure 2.2.: Feedback diagram describing a regenerative laser cavity (Siegman 1986).

2.2.3. Mode Competition

Laser cavities have the potential of oscillating in a large number of different modes, including different axial and transverse modes, different directions as in ring cavities, and even different senses of polarization. For the Ti:Sapphire laser discussed here, a Faraday rotator and Brewster windows at the crystal were used to select modes with one direction and one polarization. The remaining modes have different gains, losses, and saturation parameters, and compete for the available population inversion in the laser cavity (Siegman 1986).

In a homogeneous gain profile, the resonator mode next to the center of the gain profile starts oscillating when the pump power exceeds threshold. Then, its intensity grows faster than that of the other modes. This causes partial saturation of the whole gain profile. But the saturation decreases the gain for the other weaker modes and their amplification is down slowed. Further, the increasing difference in amplification favors the strongest mode (Demtröder 1996). In the homogeneously broadened type of ring cavity laser shown in figure 2.3, two oppositely traveling waves at the same frequency propagate in the cavity. The cross saturation effect between two oppositely traveling waves will be larger than the self-saturation effect by a factor of two (Siegman 1986).

In the case of two-mode competition in the ring cavity, the expression can be written as (Siegman 1986).

$$\frac{dI_1}{dt} = [\alpha_1 - \beta_1 I_1 - \theta_{12} I_2] \times I_1 \tag{2.8}$$

$$\frac{dI_2}{dt} = [\alpha_2 - \beta_2 I_2 - \theta_{21} I_1] \times I_2 \tag{2.9}$$

where the coefficients α_1 and α_2 are the small-signal or unsaturated gains minus losses for each mode, and the coefficients β_i and θ_{ij} are the self- and cross-saturation coefficients, respectively.

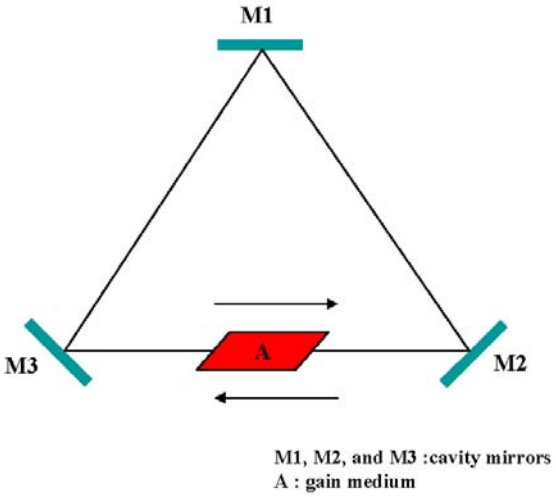

Figure 2.3.: Feedback mode competition between oppositely directed waves in the ring cavity. Modified from Siegman (1986).

2.2.4. Ti:Sapphire Oscillator

The first Ti:Sapphire laser was built by Moulton (1982). Ti:Sapphire is sapphire (Al_2O_3) doped with titanium (Ti^{3+}) to create local impurities of $Ti^{3+}Al_2O_3$. Doping levels of up to 0.5 weight% can be achieved. It has several very desirable characteristics which make it ideal as a high-power amplifier material, including a very high damage threshold ($\approx$8 to 10 $J\,cm^{-2}$), a high saturation fluorescence ($\approx 0.9\ J\,cm^{-2}$), a high thermal conductivity (46 $W\,mK^{-1}$ at 300 K), and a suitable peak gain cross section of $\sigma_g \approx 2.7 \times 10^{-19} cm^2$ (Backus et al. 1998). Moulton (1982) has observed the fluorescence decay at room temperature to be exponential, with a photon lifetime of the excited state of 3.15$\pm$0.05 μs.

The Ti:Sapphire crystal has a 4-level energy band, which is typical for solid-state laser materials. The energy diagram as shown in figure 2.4 depicts the absorption and emission bands of the $3d^1 Ti^{3+}$ ion. In the diagram, the $^2T_2$ level is the ground state, while the ^2E level is the excited state. The

closely spaced vibrational sublevels broaden the electron energy levels. The Ti:Sapphire laser is called a vibronic laser because the laser transitions are electronic-vibrational transitions from an electronically excited state to the ground state. The output range (emission band) is from around 660 nm to 1180 nm. This makes the Ti:Sapphire laser the most widely tunable laser of its class. A population inversion is created in the ^{2}E state through optical pumping. The laser action originates from the decay of vibrationally excited levels from the ^{2}E state into the ground state.

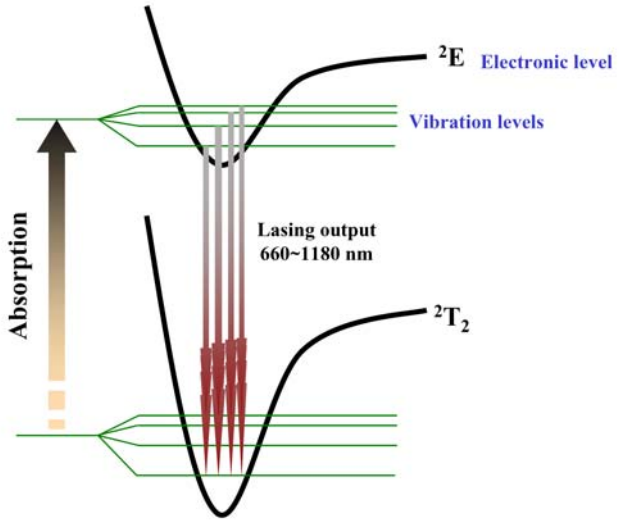

Figure 2.4.: The energy-level diagram of the Ti:Sapphire crystal.

Absorption transitions of Sapphire crystals doped with Titanium (Ti^{3+}) ions occur over a broad range of wavelengths from 400 nm to 600 nm, as shown in figure 2.5. The emission band extends from around 660 nm to 1180 nm, as shown in figure 2.6. The tuning range is affected by mirror coatings, loss in the laser cavity, pump laser, and pump mode quality.

The surfaces of the Ti:Sapphire crystals are typically made with *Brewster-cut* surfaces. This means that the crystals are cut at an angle relative to the long axis of the crystal. The reflection losses on the *Brewster-cut* surfaces are minimized for light incident on the crystal with a polarization perpendicular to the surfaces.

2.3. Mode Selection Component

Multi-mode lasers need additional wavelength selective elements inside or outside the laser resonator to ensure single-mode, or in this particular case, dual-mode operation. Lyot filters, prisms, gratings, and Fabry-Perot etalons are commonly used to obtain single-mode or dual-mode operation. In this experiment, the Fabry-Perot etalons were used because the Faby-Perot etalons can make a narrowest filtering bandwidth. For perfect selection, however, high suppression of the unwanted modes and high transmission of the wanted mode by the filter are required. The external mode selection

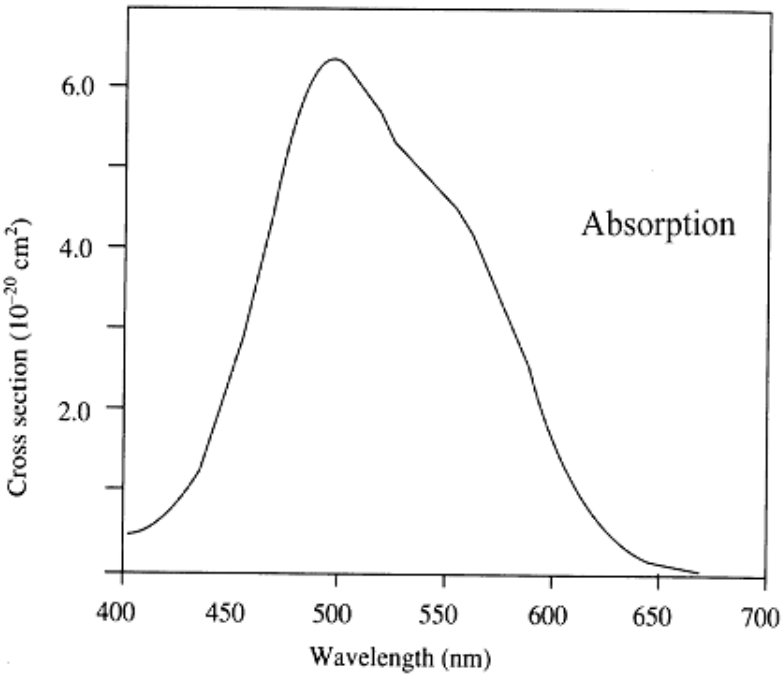

Figure 2.5.: Absorption profile for Ti transitions from $^2T_2$ to ^2E. Modified from Verdeyen (1995).

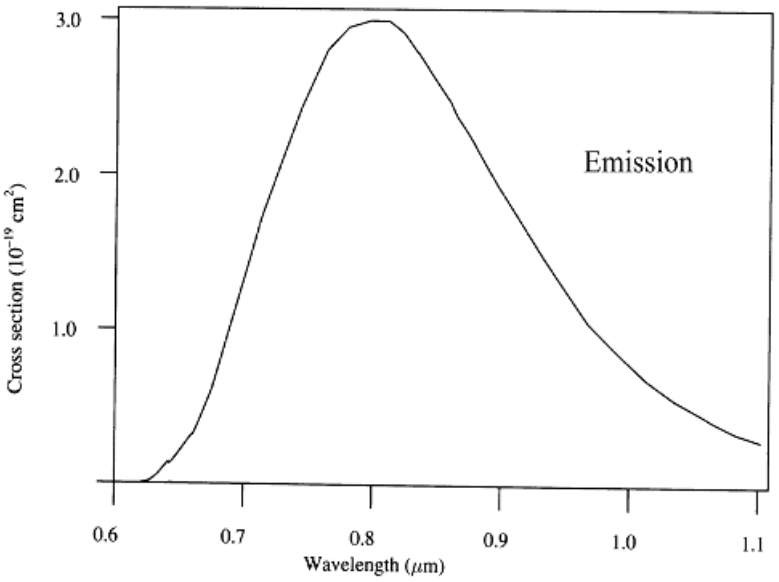

Figure 2.6.: Emission profile for Ti transitions from ^2E to $^2T_2$. Modified from Verdeyen (1995).

technique has the disadvantage that it does not suppress the unwanted modes. The internal mode selection filters completely suppress the unwanted modes when the losses exceed the gain (Demtröder 1996).

We have used Fabry-Perot etalons in combination with a Lyot filter (or birefringent filter) for the internal mode selection. First, these filters are described theoretically and then the mode selection setup is explained.

2.3.1. Fabry-Perot Etalon

Fabry-Perot etalons are made of two reflecting mirrors facing each other. The space between mirrors can be either solid (glass, quartz, etc.) or air. A Fabry-Perot etalon is an optical interferometer in which a beam of light undergoes multiple reflections between two reflecting surfaces, and whose resulting optical transmission (or reflection) is periodic in wavelength. The optical transmission and reflection are determined by the length of the etalon and its index of refraction.

1. Transmission of a Fabry-Perot Etalon

The plane-parallel etalon acts as a frequency filter or interferometer through the superposition of multiple reflections from the partially reflecting dielectric interface of the etalon. The etalon performs a simple transfer function changing optical frequency into transmitted intensity. Figure 2.7 shows the multiple reflection and transmission of the etalon.

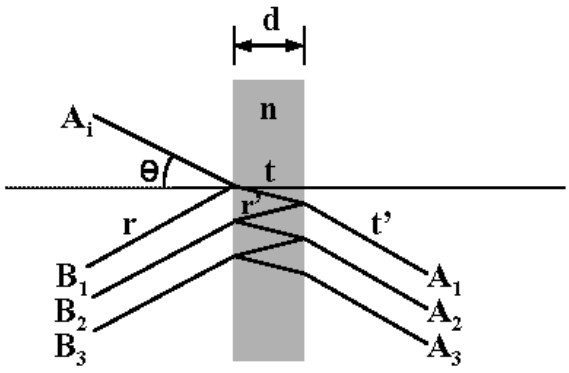

Figure 2.7.: Multiple beams transmitted and reflected from a plane parallel plate of thickness d. A_i is the amplitude of the incident field, B_1 is the reflected amplitude from the first interface, A_1 is the partially transmitted amplitude from the second interface, and r and t are the coefficients of amplitude reflection and transmission.

The multiple output beams differ in phase due to the different path lengths traversed by each of the beams. The optical phase acquired by the light on one round trip through the etalon is given by,

$$\phi = 4\frac{\pi n d \cos(\theta)}{\lambda} \tag{2.10}$$

ϕ is the optical path difference of neighboring transmitted rays, θ is the angle of incidence in the etalon, λ is the wavelength, d is the physical cavity thickness, and n is the index of refraction.

The transmitted intensity (the derivation of the equation is given in Appendix A) is as follows:

$$I = I_0 \frac{(1-R_1)(1-R_2)}{(1-\sqrt{R_1R_2})^2 + 4\sqrt{R_1R_2}\sin^2(\phi/2)} \tag{2.11}$$

where I is the transmitted intensity (same as I_t), I_0 is the incident intensity (same as I_i) when the ray was transmitted through different refraction index etalon on both surfaces. R_1, R_2 are the reflectance of each mirror surface. Maximum transmittance (the location of transmission peaks) occurs for frequencies which satisfy the equation.

$$f_m = \frac{mc}{2nd\cos(\theta)} \tag{2.12}$$

where m is any integer. A typical transmission curve is shown in figure 2.8.

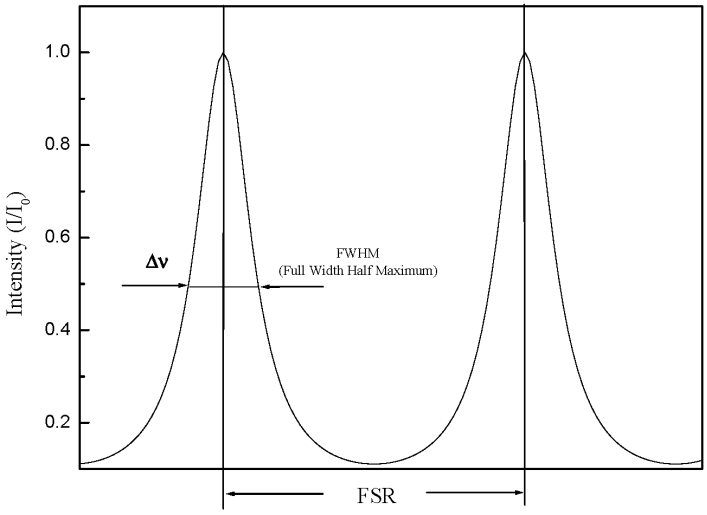

Figure 2.8.: Typical transmission curve of the etalon.

2. Free Spectral Range (FSR)

The wavelength of maximum transmission occurs periodically, and the spacing between maximum transmission peaks is called the free spectral range (FSR). At normal incidence, the FSR of an ideal etalon depends on the index of refraction (n) and the cavity thickness (d). The product of these two values, nd, is known as the optical path length (OPL). The FSR equation is the following:

$$FSR = \frac{c}{2nd\cos(\theta)} \tag{2.13}$$

3. Finesse (F)

The finesse F is simply the ratio of resonance peak spectral separation over the peaks′ spectral width. It connects the spectral resolution (called the Q-factor in oscillators) of the etalon to the cavity losses. Figure 2.9 shows the transmission curves for various reflection coefficients of the mirrors. There is a connection between the width of a resonance peak and the value of reflection. When losses are mainly due to the mirrors′ reflectivity, a simple relation gives the value for finesse as follows,

$$F_R = \frac{FSR}{\Delta\nu_{\mathrm{FWHM}}} = \frac{\pi(R_1R_2)^{1/4}}{1-\sqrt{R_1R_2}} \tag{2.14}$$

where F_R is called the reflectivity finesse, $\Delta\nu_{\mathrm{FWHM}}$ is the peaks′ spectral width, and R_1 and R_2 are the mirrors reflectivities. For practical etalons, their reflectivity finesse is not the only finesse that expresses the quality of the etalon. The so-called total finesse F_T can be written as the root mean square of the theoretical cavity finesses F_C (which is directly related to F_R but includes cavity losses due to the mirrors), the surface accuracy finesse F_S, the parallelism finesse F_P, the beam divergence finesse F_θ, and the diffraction finesse F_D. So, F_T is expressed as shown in table 2.1.

$F_T = \dfrac{1}{\sqrt{\left(\frac{1}{F_C^2}+\frac{1}{F_P^2}+\frac{1}{F_S^2}+\frac{1}{F_\theta^2}+\frac{1}{F_D^2}\right)}}$	Total *finesse*
$\mathrm{F_C} = \dfrac{\pi(R_1R_2)^{1/4}e^{-\alpha d/2}}{1-\sqrt{R_1R_2}e^{-\alpha d}}$	Theoretical cavity *finesse* coefficient due to mirrors reflectivity and cavity losses
$\mathrm{F_P} = \dfrac{\lambda}{\sqrt{3}\beta CA}$	Surface parallelism *finesse* coefficient
$\mathrm{F_S} = \dfrac{M}{2}\dfrac{\lambda}{633\,nm}$	Spherical deviation *finesse* coefficient
$\mathrm{F_\theta} = \dfrac{\lambda}{d\tan^2\Theta}$	Incident beam divergence dependant *finesse* coefficient
$\mathrm{F_D} = \dfrac{CA^2}{2d\lambda}$	Diffraction limited *finesse* coefficient

Table 2.1.: Fabry-Perot etalon finesse with the surface accuracy and parallelism. α is the linear cavity loss coefficient, αd is the roundtrip loss, β is the tilt angle between surfaces (typically 1 arcsec), CA is the etalon aperture diameter, d is the distance between mirrors, M is the surface flat accuracy in fraction of wavelength (for $\lambda/100$; $M = 100$), and Θ is the incident beam divergence (Doric & Neron 2005).

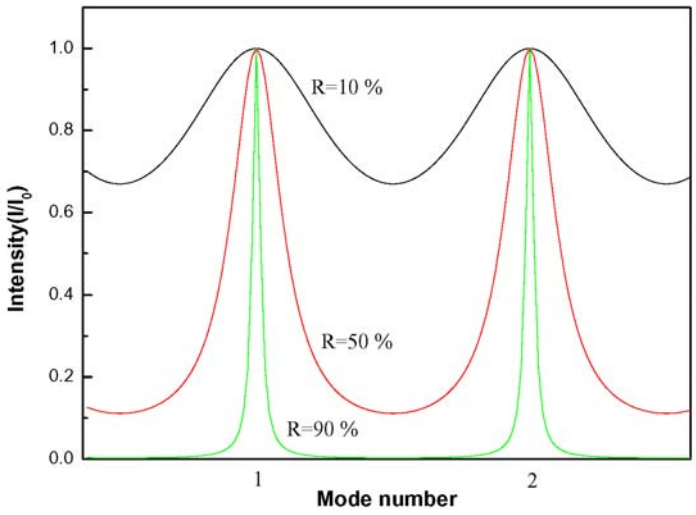

Figure 2.9.: The transmission curves for various reflection coefficients of the mirrors when R_1 and R_2 are identical.

4. Full Width Half Maximum (FWHM)

Conceptually, finesse can be thought of as a number of interfering beams within the etalon. A high finesse indicates a high number of interfering beams, resulting in a more complete interference process and, therefore, higher spectral resolution. Spectral resolution is defined as $FSR/\Delta\nu_{\mathrm{FWHM}}$ where $\Delta\nu_{\mathrm{FWHM}}$ is the minimum resolvable bandwidth or full width at half maximum peak intensity (FWHM) of an interference fringe generated when a perfectly monochromatic light source is transmitted by an etalon. The minimum resolvable bandwidth is hence defined as:

$$\Delta\nu_{\mathrm{FWHM}} = \frac{FSR}{finesse} \tag{2.15}$$

The highest possible resolution (smallest minimum resolvable bandwidth) is achieved when an etalon has the smallest FSR and the highest finesse appropriate for the incident light source.

5. Effect of Thermal Expansion

One important factor for the frequency stability of Fabry-Perot interferometers is the thermal expansion of the etalon material. The frequency drifting characteristics of a Fabry-Perot etalon can be qualified by temperature coefficient η of the optical cavity length, which is given by

$$\eta = \alpha + (\frac{1}{n})(\frac{dn}{dT}) \tag{2.16}$$

where α is the thermal expansion coefficient of the etalon in unit of ppm/°C (ppm : part per million), n is the refractive index, and T is temperature. Thus, the temperature dependence of the resonant wavelength of the etalon is expressed by

$$\frac{d\lambda}{dT} = \lambda\eta \tag{2.17}$$

We can also expect that the change in length of the etalon separation ($D(T)$) due to a change in temperature from an initial temperature T_0 to a temperature T (Photonics 2006) is.

$$\frac{dD}{dT} = D(T_0)[1+\alpha(T-T_0)] \tag{2.18}$$

And for the index of refraction,

$$\frac{dn}{dT} = n(T_0)[1+\beta(T-T_0)] \tag{2.19}$$

Therefore, the temperature dependence of the FSR and the peak locations (ν) are as follows: (Photonics 2006)

$$\frac{dFSR}{dT} = FSR(T_0)[1-(\alpha+\beta)(T-T_0)] \tag{2.20}$$

$$\frac{d\nu}{dT} = \nu_0(T_0)[1-(\alpha+\beta)(T-T_0)] \tag{2.21}$$

where β is the thermal refractive index coefficient in ppm/°C. Also, the frequency shift per °C can be given by the following relation (Doric & Neron 2005),

$$\frac{d\nu}{dT} = \frac{c}{\lambda_0}(\frac{1}{n}\frac{dn}{dT}+\alpha) \tag{2.22}$$

where c is the speed of light in free space, and λ_0 is the peak wavelength of the etalon. The parameters of temperature variation effect of the fused silica and air are described in table 2.2, and FSR variation versus temperature in the 1.6 m air-spaced cavity is shown in figure 2.10. As shown in the figure, the changed FSR is 200 Hz / 1 °C.

	Symbol	Unit	Fused silica	Air
Refractive index (λ=1.55 nm)	n		1.44415	1.0003
Thermal expansion coefficient	α	$[ppm/°C]$	0.55	0.1
Thermal refractive index coefficient	β	$[ppm/°C]$	6.57	1.0
Temperature dependence of refractive index	$\frac{dn}{dT}$	$[\boldsymbol{ppm/°C}]$	8.4	-0.9
Frequency shift vs. temperature	$\frac{d\nu}{dT}$	$[\boldsymbol{GHz/°C}]$	-1.23	~0.17
Wavelength shift vs. temperature	$\frac{d\lambda}{dT}$	$[\boldsymbol{nm/°C}]$	0.01	-0.001

Table 2.2.: Parameters with the temperature variation effect of the cavity materials (Doric & Neron 2005).

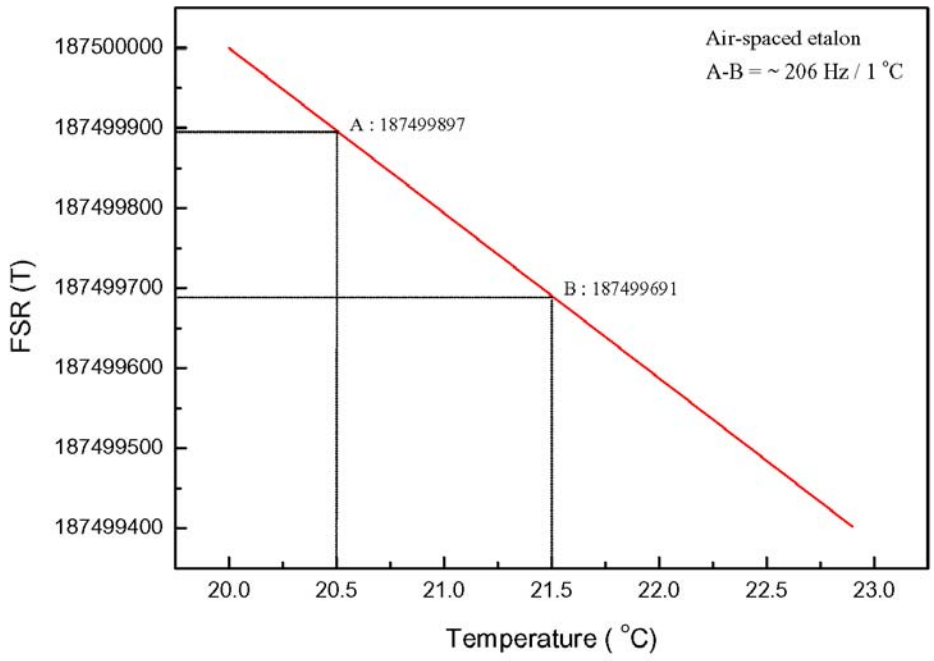

Figure 2.10.: The calculated FSR variation with the temperature of the cavity material for a 1.6 m air-spaced cavity.

2.3.2. Birefringent Filter

A birefringent crystal has a preferred direction called the optical axis. The crystal has a different index of refraction for light polarized parallel to the optical axis than it has for light polarized perpendicular to the optical axis. We assume that the optical axis is in the $x-y$ plane and send a beam of photons in the z-direction. Photons polarized perpendicular to the optic axis are called ordinary and are in the state o, and photons polarized parallel to the optic axis are called extraordinary and are in the state e (see figure 2.11). The wave propagation in a birefringent uniaxial crystal can be expressed as (Meschede 2004)

$$\frac{1}{n^2(\theta)} = \frac{\cos^2\theta}{n_o^2} + \frac{\sin^2\theta}{n_e^2}. \tag{2.23}$$

This equation describes the index ellipsoid of the refractive index in a birefringent uniaxial crystal, which is shown in figure 2.11 (right side). n_o is the refractive index of the ordinary ray, and n_e is the refractive index of the extraordinary ray.

The principle of the birefringent filter (or Lyot filter) is that light originating in a single polarization state can be made to interfere with itself. An optically anisotropic and birefringent material can be used to produce a relative delay between ordinary and extraordinary rays aligned along the fast and slow axes of the crystal because a birefringent medium has two different refractive indices, n_o and n_e, depending on the plane of light propagation through the medium. The FSR of the birefringent

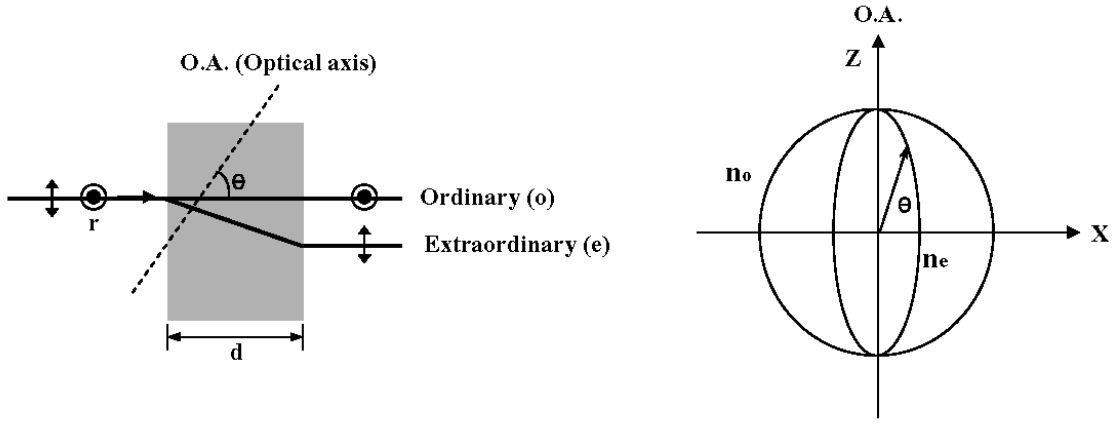

Figure 2.11.: (Left) Ordinary and extraordinary rays in birefringence, (Right) The index ellipsoid.

filter is given by

$$FSR = \frac{c}{\Delta n d}, \tag{2.24}$$

where Δn is the difference in refractive index between the fast and slow axes $\Delta n = n_o - n_e$, d is the thickness of the birefringent medium. The parameters of important birefringence materials are described in table 2.3. The transmission of the birefringent filter is (Meschede 2004)

$$T(\lambda) = \frac{I_T}{I_0} = T_0[\cos^2(\frac{\Delta n \pi d}{\lambda}) + \sin^2(\frac{\Delta n \pi d}{\lambda})\cos^2 2\phi], \tag{2.25}$$

where ϕ is the phase difference caused by a single retarder given by

$$\phi = \frac{2\pi \Delta n d}{\lambda}. \tag{2.26}$$

Material	n_o	n_e	Δn	$\alpha_{\max}$
Quartz	1.5442	1.5533	0.0091	0.5°
Calcite	1.6584	1.4864	-0.1720	6.2°
$LiNbO_3$	2.304	2.215	0.0890	2.3°

Table 2.3.: Birefringence of important materials at $\lambda = 589\,nm$ and $T = 20°$C, α is the angle between the dielectric displacement and the incident angle (Meschede 2004).

The maximum transmission occurs when the incident light is plane-polarized at an azimuth of $\pm 45°$ to the fast axis and the retardation of the plate is $\frac{\lambda}{4}$. If a $\frac{\lambda}{4}$ retarder is illuminated with polarized light, the emerging beam will usually be elliptically polarized. Circular polarization is a special case occurring when the optical axis is at $\pm 45°$ to the input polarization and the retardation

is exactly $\frac{\lambda}{4}$. Thus, the phase difference between the fast and slow axes from the output of the filter becomes $\frac{\pi}{4}$. Therefore, the transmission of a birefringent filter can be described as

$$T(\lambda) = T_0 \cos^2(\frac{\pi \Delta n d}{\lambda}). \tag{2.27}$$

When N elementary birefringent plates with different thickness d are used in series, the total transmission T is the product of the individual transmissions T_m:

$$T(\lambda) = \prod_{m=1}^{N} T_{0m} \cos^2(\frac{\pi \Delta n d_m}{\lambda}) \tag{2.28}$$

The typical birefringent filter is shown in figure 2.12. The typical filter consists of three plates with a d:2d:4d thickness ratio, and the typical transmission curves are shown in figure 2.13.

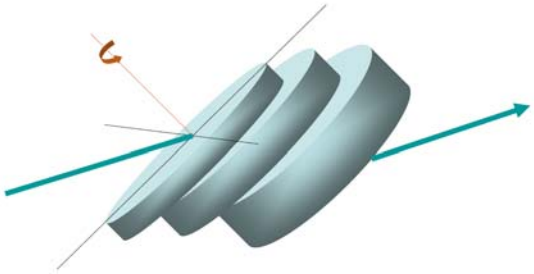

Figure 2.12.: A typical birefringent filter configuration. The birefrinent filter consists of three plates with a thickness ratio of 1:2:4. Wavelength is tuned by rotating the stack.

2.3.3. Mode Selection Principle

The Ti:Sapphire ring cavity laser has an extremely wideband lasing profile. To select two modes in the multi-mode ring cavity laser, two types of mode selection components are inserted into the ring cavity. We can use the birefringent filter with a broadband filtering bandwidth. For the next step, the Fabry-Perot etalon with a very narrow filtering bandwidth is used to select two modes. Figure 2.14 shows the schematic configuration for the filtering principle.

In this experiment, the birefringent filter with a FWHM of 1.7 THz limits the number of modes to a band of only a few hundred GHz width. This is due to the mode competition that suppressed the weaker modes. The practical bandwidth also depends on the threshold gain of the laser itself, loss in the cavity, and mode competition.

To select two modes, two intracavity etalons are installed. The expected difference frequency of the two modes is determined by the thin etalon, which have a FSR of 100 GHz and a FWHM of 40 GHz in this work (see figure 2.15 (top)). The thick etalon suppresses the rest of the modes under the transmission curve of the thin etalon. Because the difference frequency between the ring cavity modes is about 184 MHz and plenty of modes normally exist under the transmission curve of the thin

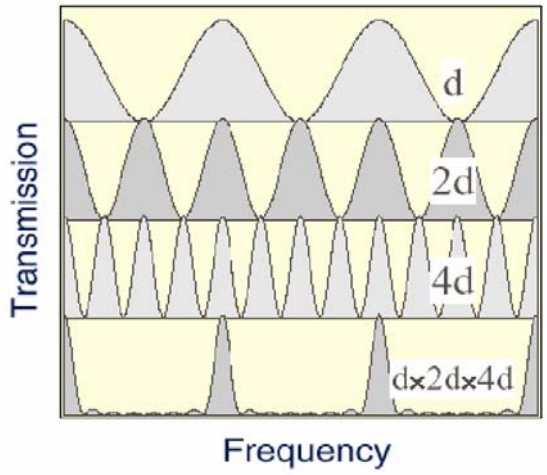

Figure 2.13.: Typical transmission curves of the birefringent filter from Meschede (2004).

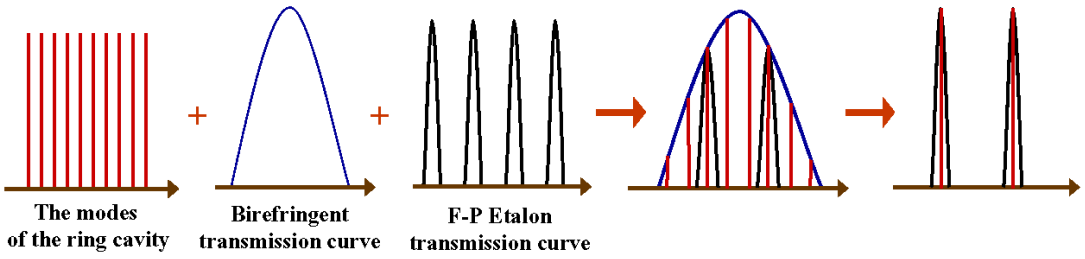

Figure 2.14.: Schematic figure of the two modes filtering.

etalon as shown in figure 2.15 (bottom). Without the thick etalon, we cannot select only one mode. Finally, two modes can be achieved with the combination of the two etalons, as shown in figure 2.16. Note that the peaks of the transmission curves can be tuned with respect to each other by tilting.

2.4. Dual-Mode Laser Operation

2.4.1. Experimental Set-up

An optical pump at the correct wavelength is required to provide energy to the gain medium in the oscillator. The Ti:Sapphire requires a pump in the green band at 532 nm. Several watts of pump power are needed because the upper-state life-time of Ti:Sapphire is very short (3.2 μs) (Moulton 1982) and the saturation power, the incident optical power required to achieve significant saturation of an absorber, is very high.

Figure 2.17 shows the laser system to demonstrate the dual-mode operation. The diode laser array at 807 nm pumps the 5 W $Nd:YVO_4$ laser (Verdi V5, Coherence Inc.). It uses $Nd:YVO_4$ as the

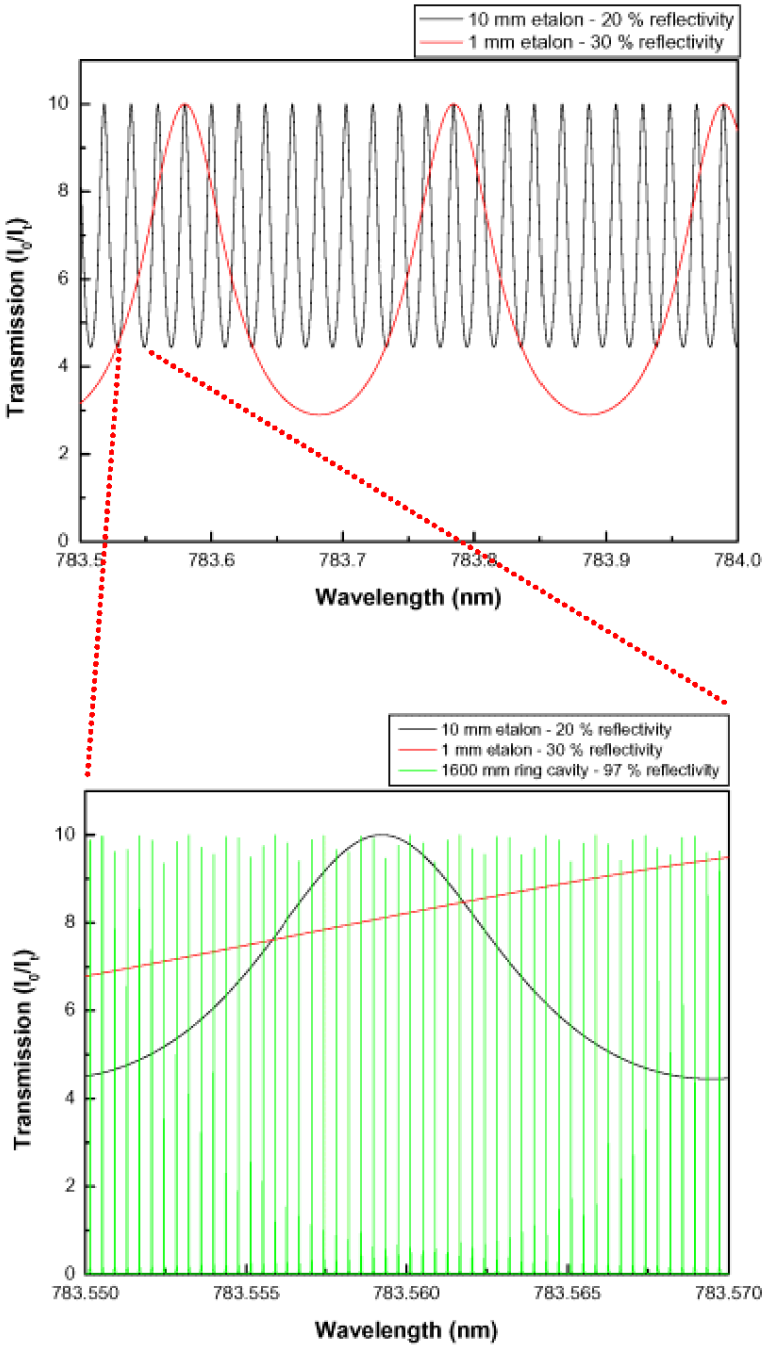

Figure 2.15.: Top : Simulation of the overlapped transmission curves of the etalons with the tilt angle of 1° and the ring cavity modes. Bottom : The transmission curves of the 10 mm and 1 mm etalons and the ring cavity modes. Many longitudinal modes (Green line) exist in the transmission curve, but most of the modes are suppressed by mode competition.

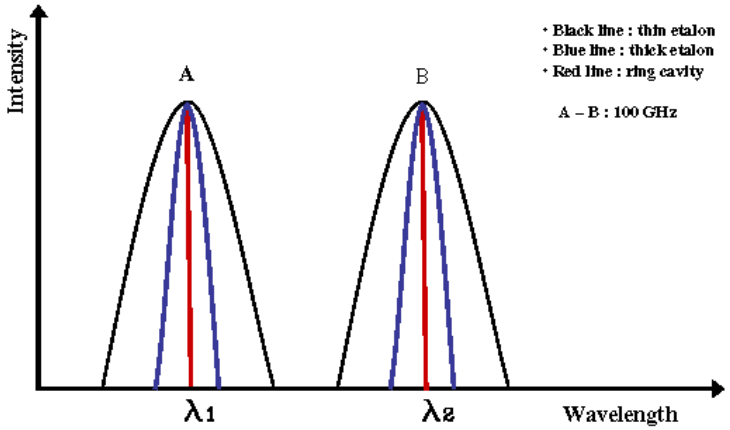

Figure 2.16.: Schematic overview of the filtered two modes by the intracavity etalons. The black curve is the thin etalon transmission curve, the blue curve is the thick etalon transmission curve, and the red line is the filtered longitudinal mode.

gain medium, which lases at a wavelength of 1064 nm. This is frequency-doubled to produce a wavelength of 532 nm by a non-linear crystal of LBO (Lithium Borate - LiB_8O_5). This is the pump for the Ti:Sapphire ring cavity laser (899-01, Coherence Inc.).

Figure 2.18 shows the schematic diagram of the Ti:Sapphire ring cavity laser with internal mode selection components. The effective round trip cavity length was 1.6 m. A periscope (mirror P) and collimation lens L were used to inject the 532 nm Nd : YVO_4 beam into the ring cavity. The cavity (or resonator) itself consisted of the curved M1, M2 mirrors and M3, M4 flat mirrors. The Ti:Sapphire crystal was placed between M1 and M2. The Ti:Sapphire laser pumped by the Nd : YVO_4 laser beam can emit light from 660 nm to 1180 nm. The direction of circulation of the light was determined by an optical diode (Faraday rotator). The frequency was chosen by adjusting a birefringent filter and two intracavity Fabry-Perot etalons.

According to the birefringent filter specification from the Coherent company, the birefringent filter consisted of three waveplates with thicknesses of 0.5 mm, four times 0.5 mm, and 16 times 0.5 mm. The FSR of the birefringent filter was 83 THz and its bandwidth (or FWHM) was 1.7 THz.

To select two modes, the two solid etalons with different thicknesses were installed inside the ring cavity. The etalons were fabricated by B.Halle GmbH in Berlin, Germany. The etalon material was fused silica with a refractive index of 1.444 at 1.5 μm wavelength. The flatness deviation is less than $\lambda/10$. The specifications of the etalons are given in table 2.4.

Figure 2.17.: Picture of the laser system.

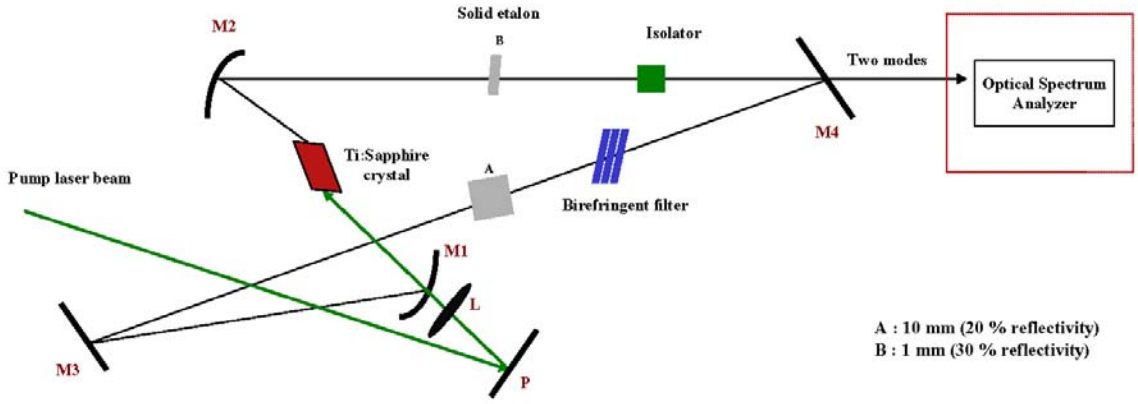

Figure 2.18.: Schematic of the dual-mode laser with internal mode selection components.

	Thickness [mm]	Reflectivity [%]	FWHM [GHz]	FSR [GHz]	Finesse
Etalon A	10	20	5.7	10	1.76
Etalon B	1	30	40	100	2.5

Table 2.4.: Specification of the etalons installed in the ring cavity for selecting the two modes. The material used fused silica with 1.444 refractive index at 1.5 μm wavelength.

2.5. Results

To characterize the Ti:Sapphire ring cavity laser, several experiments were done to determine the beam diameter of the Ti:Sapphire laser, the spectral width of the longitudinal mode in the ring cavity and the stability of the longitudinal mode in the ring cavity. The dual-mode operation using mode-selection components as the birefringent filter and the Fabry-Perot etalons was demonstrated. In this section the experimental results are described.

2.5.1. Transmission Curves of the Etalons

Figures 2.19 and 2.20 show the etalon transmission curves measured using a tunable laser diode (New Focus, Velocity 6300). The resolution bandwidth of the scanning laser was 0.005 nm. As shown in the figures, the FSR and FWHM values were close to the calculated results given in table 2.4.

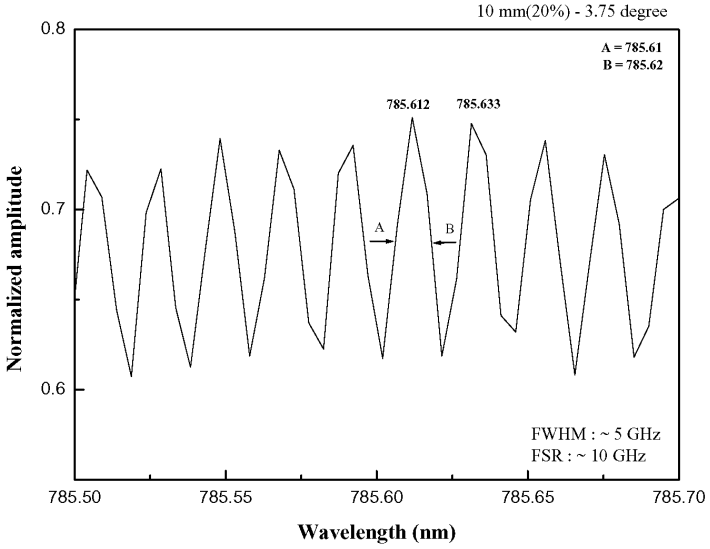

Figure 2.19.: Measured transmission curve of the 10 mm etalon. The tunable diode laser was used for scanning with resolution bandwidth of 0.005 nm.

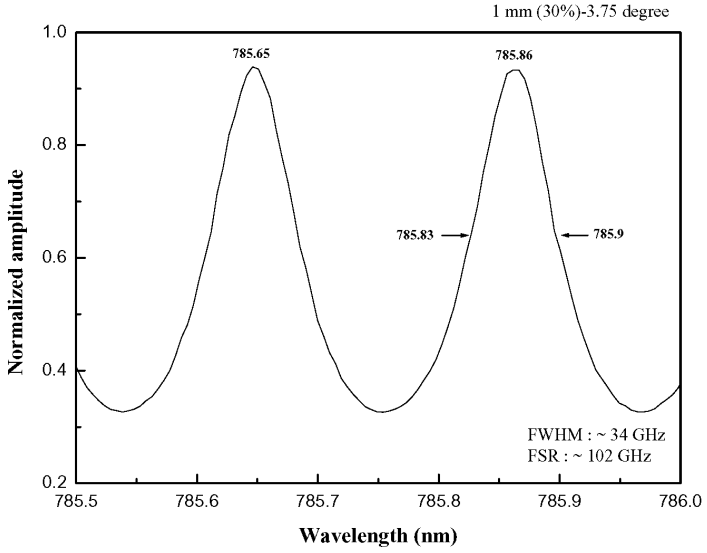

Figure 2.20.: Measured transmission curve of the 1 mm etalon. The tunable diode laser was used for scanning with resolution bandwidth of 0.005 nm.

2.5.2. Beam Diameter of the Ti:Sapphire Laser

To measure the beam diameter of the Ti:Sapphire laser, a Coherent Beam Master system was used. There are two primary Knife-edges used for the main profile diameter determination. The determined profiles, called W and V, are perpendicular to each Knife-edge as shown in figure 2.21.

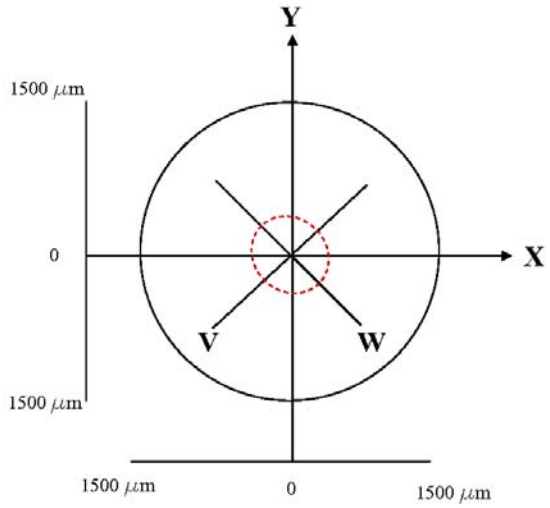

Figure 2.21.: Schematic of Beam Master axis (Knife-edge).

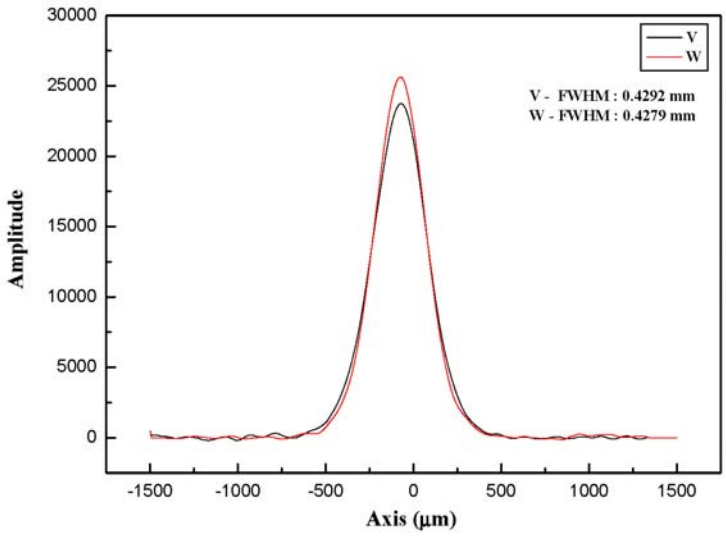

Figure 2.22.: Measured Gaussian profile of Ti:Sapphire laser beam. The FWHM of the beam is 0.43 mm.

Figure 2.22 shows the measured beam profiles, which appear Gaussian with a waist $1/e$ of approximately 0.43 mm. The waist was measured at 300 mm from the output coupler.

2.5.3. Spectral Width of the Ti:Sapphire Laser

Radio- or submillimeter astronomy requires high resolution spectroscopy, for which the FWHM of the LO source must be as narrow as possible. Currently, the best resolution bandwidth of spectroscopic observations that has been achieved is about 30 kHz at submillimeter wavelength. This corresponds to a velocity resolution of 9 $\mathrm{km\,s^{-1}}\,\nu^{-1}$, where ν is the observing frequency in GHz, or

30 km s^{-1} at 300 GHz, but 0.3 km s^{-1} at 30 GHz. Lines in cold, dark interstellar clouds can have linewidths as narrow as 0.1 km s^{-1}. Therefore, 30 kHz frequency resolution is adequate for practically all astronomical submillimeter applications, but would not be for longer-wavelength radio observations.

To use the Ti:Sapphire laser as a LO source for the radio telescope, a spectral width less than 30 kHz is required. Figure 2.23 shows the spectral width of the Ti:Sapphire ring cavity laser beam, which is the 184 MHz mixing product of two adjacent ring cavity modes. The spectral width was about 12 kHz. This spectral width is quite narrow enough to use of the Ti:Sappire laser as the LO source for high resolution radio spectroscopy.

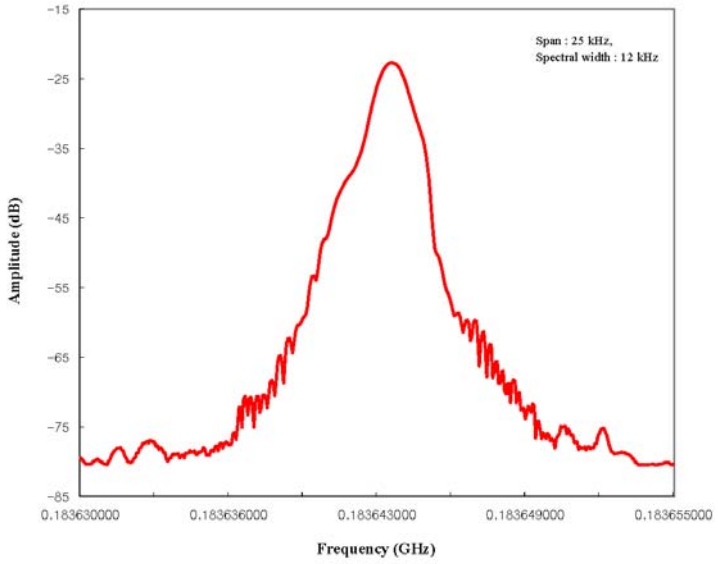

Figure 2.23.: Spectral width of the Ti:Sapphire laser measured by mixing ring cavity modes to produce a difference signal at 184 MHz which was measured with an RF spectrum analyzer. The frequency span is 25 kHz and the spectral width is 12 kHz.

2.5.4. Frequency Stability of the Ti:Sapphire Laser

To observe radio molecular lines from the interstellar medium or from circumstellar envelopes, a frequency stabilized LO signal is needed because a drift in the LO frequency makes a determination of the source′s kinematical properties (by Doppler shifts) impossible and causes problems when identifying the unidentified molecular transitions. Thus the LO frequency must be stabilized to better than the resolution bandwidth of the spectroscopic observation.

The frequency stability of the Ti:Sapphire laser was measured in the laboratory at room temperature (20 °C ±1 °C). The output power of the laser was approximately 500 mW. Figure 2.24 shows the frequency drift of the Ti:Sapphire ring cavity mode as a function of the temperature change over three hours. The spectrum was produced by mixing of the n mode and $n+1$ mode in the cavity with a commercial photodetector and displaying the mixing product on an RF spectrum analyzer. The

frequency drift was about 332 kHz / 1.3 ^{o}C. So the beat frequency is equal to the FSR of the modes. For example, in the case of 184 MHz beat frequency, the frequency drift is 332 kHz but in the case of 1 THz, the frequency drift is 332 kHz $\times$5000. Therefore, for the short-term stability and for low beat frequencies, this drift is not a serious problem because the observation time for one scan is very short (less than 3 minutes). However, to achieve long-term stability and for observations using high beat frequencies a frequency stabilization system is required. The drift is due to thermal changes of the intracavity material (air) and mirrors.

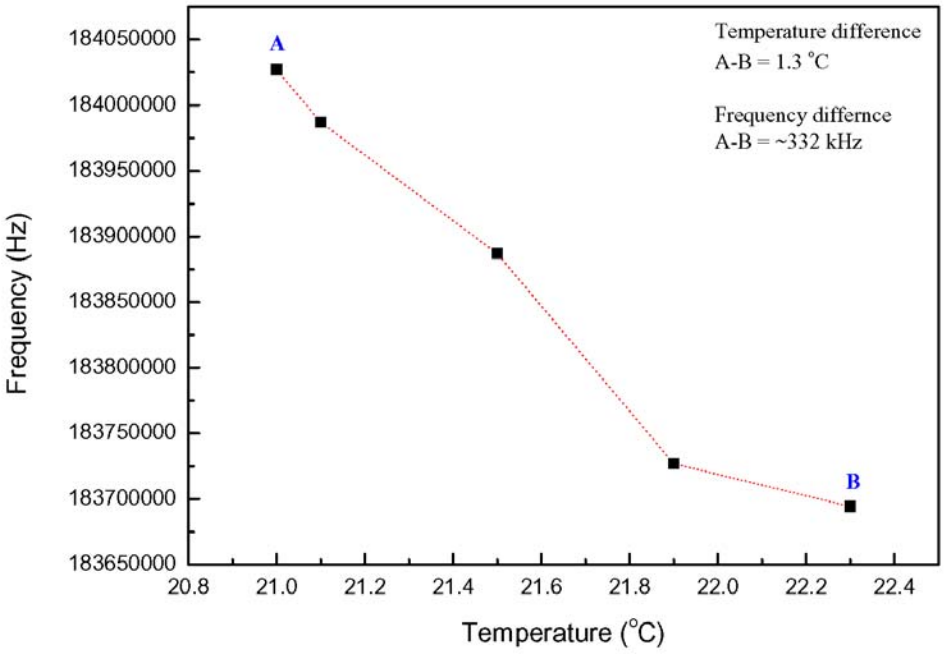

Figure 2.24.: Frequency stability of the Ti:Sapphire laser mode as a function of temperature changing, showing frequency drift sampled at five instances.

2.5.5. Dual-Mode Operation

As shown in figure 2.25, the dual-mode was clearly observed. The difference frequency was around 100 GHz. The output power of the dual-mode was around 200 mW. To confirm that there was only one mode in each mode profile, the mixing product was observed using the photodetector and the RF spectrum analyzer. If more than one mode were present, a mixing product with a 184 MHz frequency components would exist. However our measurements showed that only one mode existed in each filtered spectrum.

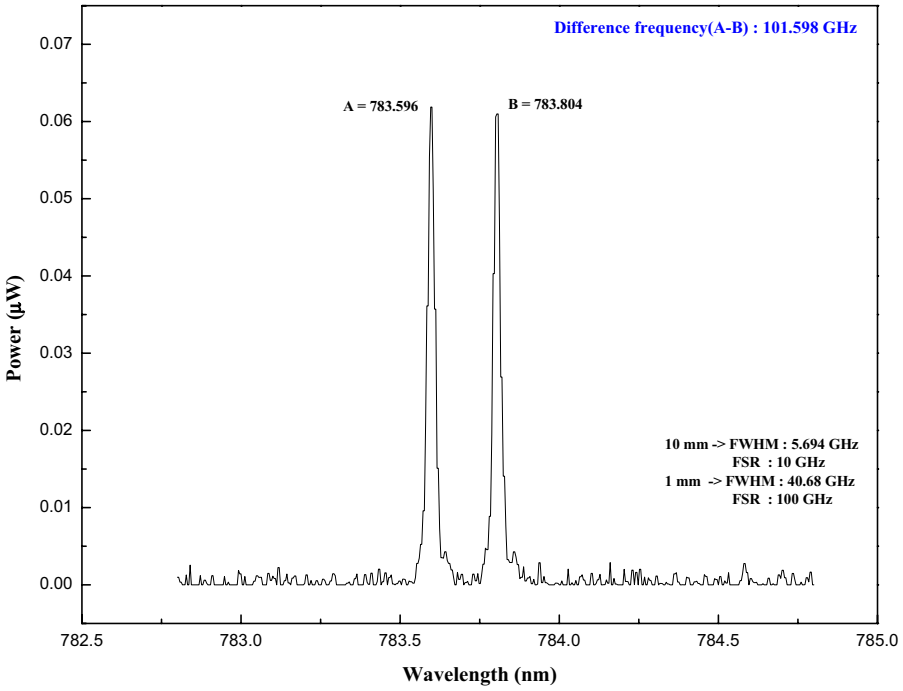

Figure 2.25.: The dual-mode spectrum from the Ti:Sapphire laser measured using an optical spectrum analyzer with an wavelength resolution of 0.1 nm. To select two modes the two etalons were installed in the ring cavity. The thicknesses of the etalons were 10 mm and 1 mm.

2.6. Summary

The Ti:Sapphire ring cavity laser and two types of mode selection components (birefringent filter and Fabry-Perot etalon) were characterized and the dual-mode operation experiment was demonstrated.

The Ti:Sapphire laser has a broadband gain profile that allows the widest tuning range of any laser. The photon life-time of the excited state is very short, around 3.2 μs. The difference frequency (FSR) of cavity modes was about 184 MHz.

The photomixer for the photonic LO system generates the difference frequency between two input laser beams. These two input laser beams should be narrow enough for high spectral resolution spectroscopy. The laser frequency should be stabilized with a tolerance equal to the resolution bandwidth. The spectral width of the Ti:Sapphire laser beam was measured to be 12 kHz adequarte for submillimeter spectroscopy and the frequency stability, which is the FSR variation of ring cavity, was measured to be 332 kHz when the room temperature changed by $\pm$ 1.3 °C around 20 °C. The frequency drift (FSR change) is probably caused by the thermal expansion of cavity material (as documented in table 2.2 and figure 2.24).

Since the Ti:Sapphire ring cavity laser has a very wideband gain profile and plenty of longitudinal modes, one needs to select two modes. A birefringent filter with 1.7 THz filtering bandwidth and two intracavity etalons with different thicknesses were used. The thicknesses of the etalons were 10 mm and 1 mm, giving FSR of 10 GHz and 100 GHz and FWHM of 5.7 GHz and 40 GHz. The birefringent

filter filtered a few hundred GHz bandwidth from the Ti:Sapphire wide-gain profile. The thin etalon filtered two colors meaning the thin etalon determined the expected difference frequency (i.e. the expected LO frequency). The thick etalon selected only one mode in the thin etalon transmission curve. The etalon and birefringent filter were selected to have a very wide FWHM but the difference frequency between the ring cavity modes was 184 MHz, so there could have been several modes within the transmission curve. However, the experimental result has confirmed that actually only the two modes separated by 100 GHz were present in the cavity.

Finally, we have achieved dual-mode operation with a difference frequency of about 100 GHz and with 200 mW power. However, the power in each mode changed continuously due to mode competition, air fluctuations, thermal fluctuation, and mechanical vibration. Therefore, we need a power stabilization system to reduce this power fluctuation. I introduce the power stabilization system in Chapter 5.

3. The 34 GHz Mixing Product

3.1. Introduction

The generation of millimeter- and submillimeter-wave radiation using a dual-mode laser has been demonstrated by Zimmermann et al. (1995), Biebersdorf et al. (2003), Johansson et al. (2005), Hyodo et al. (1996), Tani et al. (2005), Stone et al. (2005), and others. These authors presented the mixing product (or beat frequency) by their experiments. Although they used various different types of lasers and different lasing bands, the basic scheme common to all those demonstrations is the dual-mode operation in one laser resonator. The advantage of this scheme, assuming that the laser cavity is stabilized against thermal fluctuations and air fluctuations, is that the mode spacing does not change very much compared to the absolute frequency drift due to common-mode rejection. It means that drift in the beat frequency generated by photomixing is a small fraction of the frequency drift.

In the previous section, the dual-mode operation, separated by 100 GHz, was presented using the Ti:Sapphire ring cavity laser with two intracivity Fabry-Perot etalons. But the spectral width of the mixing product could not be observed directly because the available maximum bandwidth of the commercial photodetector is around 50 GHz. Therefore, to observe the spectral width of the mixing product of two modes produced by the Ti:Sapphire laser, I analyzed the mixing product at 34 GHz.

3.2. Experimental Set-up

The schematic diagram for the 34 GHz beat frequency observation is shown in figure 3.1. The fundamental scheme for the experimental setup is the same as the setup for the dual-mode observation described in Chapter 2. The Ti:Sapphire laser with internal mode selection components had a ring configuration as shown in figure 3.1. The effective round trip cavity length is 1.6 m. A periscope (mirror P) and collimation lens L were used to inject the 532 nm $Nd:YVO_4$ beam into the ring cavity. The cavity (or resonator) itself consisted of the curved M1, M2 mirrors and M3, M4 flat mirrors. The Ti:Sapphire crystal was placed between M1 and M2. The Ti:Sapphire was pumped by the $Nd:YVO_4$ laser. The direction of circulation of the light was determined by an optical diode (Faraday rotator) and so reduced the interference effect between clockwise trip photons and counter clockwise photons. The frequency was chosen by adjusting a birefringent filter and two etalons.

The birefringent filter and two internal etalons (B.Halle Nachfl GmbH, Germany) served as mode-selection components. The FSR of the birefringent filter was 83 THz and the bandwidth (FWHM) was 1.7 THz. The etalon material was fused silica with a refractive index of ~ 1.444. The theoretical specifications of the 12 mm etalon with 20 % reflectivity when the etalon is tilted by 1° to the incident ray are given in table 3.1. The expected dual-mode is shown on the overlapped transmission curves of two etalons in figure 3.2. The arrows on the graph indicate the expected modes that pass through both filters.

The filtered two modes were directed into the commercial photodetector made by New Focus

	Thickness [mm]	Reflectivity [%]	FWHM [GHz]	FSR [GHz]	Finesse
Etalon A	12	20	4.7	8.3	1.76
Etalon B	3	20	19	33	1.76

Table 3.1.: Specification of the etalons installed in the ring cavity for selecting the two modes. The material used fused silica with 1.444 refractive index at 1.5 μm wavelength.

(Model number 1004) which has -45 dBm output power when the input power is 0.8 mW at 780 nm wavelength. The filtered dual-mode were mixed by the photoconductive mixing effect. The 34 GHz beat frequency radiation generated by the photodetector was coupled into the Agilent E4448A PSA series spectrum analyzer.

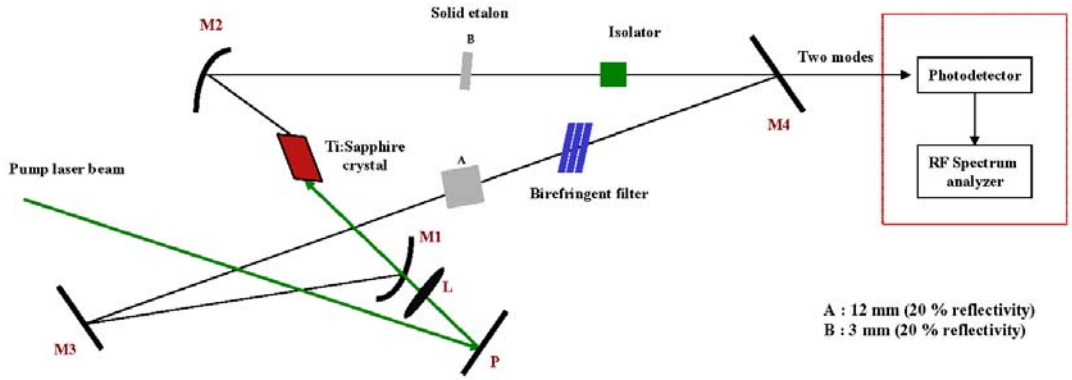

Figure 3.1.: Experimental setup for the 34 GHz mixing product observation. To select two modes, 3 mm and 12 mm etalons were installed as internal etalons then the filtered two modes were mixed by a commercial photodetector.

3.3. Experimental Results

The experiments were done at a room temperature of 20 °C $\pm$ 0.5 °C. The Ti:sapphire ring cavity was not completely thermally and acoustically isolated. The pump laser power from the Coherent Verdi V5 was 5 W. The power of the Ti:Sapphire laser without etalons was around 500 mW and power with etalons was around 120 mW due to the loss from the etalons. The output power from the laser cavity is related to round trip losses, round trip unsaturated gain, output transmission and saturation parameter. Hence the output power can be given by (Alfrey 1989)

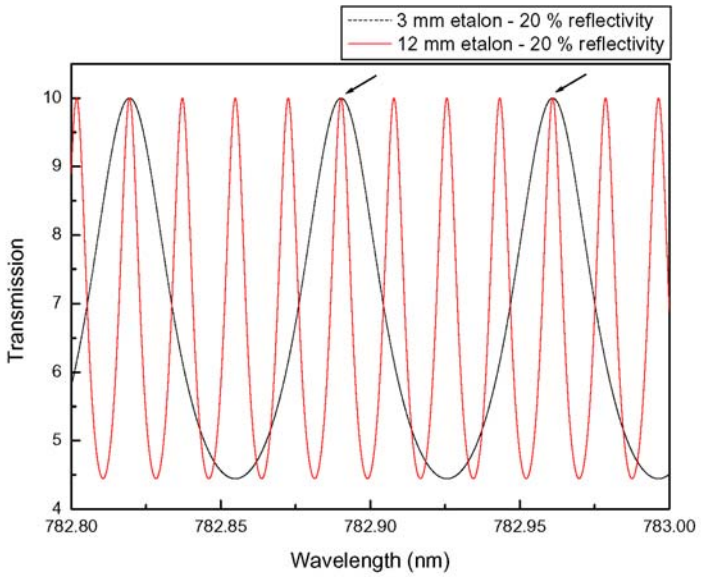

Figure 3.2.: Theoretical transmission curves of etalons assuming that the etalons are tilted by 1° to the incident ray. The expected difference frequency is around 34 GHz and the arrows indicate the expected filtering modes by overlapped transmission peaks of each etalon.

$$I_{\text{out}} = \frac{\text{output transmission}}{2 \times \text{saturation parameter}} \cdot [\frac{\text{round trip unsaturated gain}}{\text{round trip loss}} - 1]. \tag{3.1}$$

The main factor reducing the output power in this setup was the round-trip losses from the intra-cavity etalons. For example, if the etalon reflectivity is 10 %, then 10 % of the incident power reflects by angle of θ into the free space from the front surface of the etalon. The other major source of loss was the alignment problem of the mirrors. Since amplification in the Ti:sapphire ring cavity laser is regenerative, the photons in the cavity should return to the same point with a tolerance equal to the beam diameter of $\sim$ 0.43 mm (measured in Chapter 2.5.2). If the mirrors are not aligned correctly then the cavity has quite high losses. In the case of this setup, two etalons were installed to select two modes. Two reflectivities of 20 % from the etalons and two more alignment elements added to the losses in the cavity.

3.3.1. Dual-Mode Observation

A tunable diode laser was used to measure the real transmission curves of the etalons. The scanning resolution was 0.005 nm. The results are shown in figures 3.3 and 3.4. The presented datas are not convoluted because the resolution of the scanning laser is quite wide whilst the etalons have a quite narrow FWHM. The measured FSR and FWHM are close to the calculated results (presented in table 3.1).

Figure 3.5 shows the dual-mode spectrum observed using an Anritsu MS9710C optical spectrum analyzer with a resolution bandwidth of 0.1 nm.

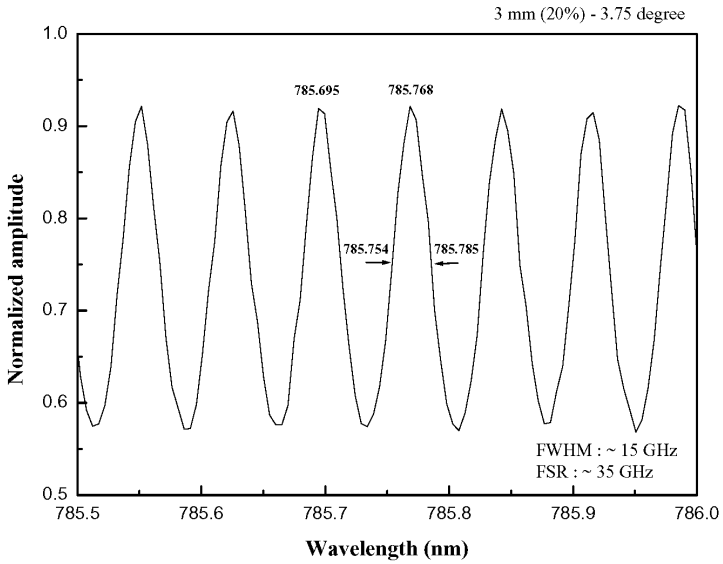

Figure 3.3.: The measured transmission curve of the 3 mm etalon scanned by tunable diode laser.

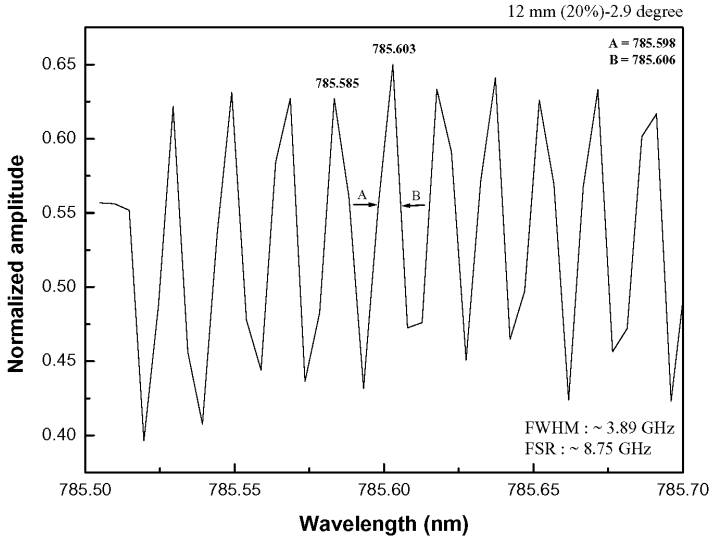

Figure 3.4.: The measured transmission curve of the 12 mm etalon scanned by tunable diode laser.

3.3.2. 34 GHz Spectrum

Figure 3.6 shows the spectrum of the 34 GHz radiation generated by mixing the dual-mode laser signal using the commercial photodetector. The spectral width of the 34 GHz spectrum is $\sim$ 6 kHz at 100 kHz span with a resolution bandwidth (Agilent RF spectrum analyzer) of 910 Hz. The noise level of the RF spectrum analyzer itself is shown in figure 3.7. The noise levels of the spectra in figures 3.6 and 3.7 are identical. Therefore the signal at 34 GHz in figure 3.6 spectrum is indeed the

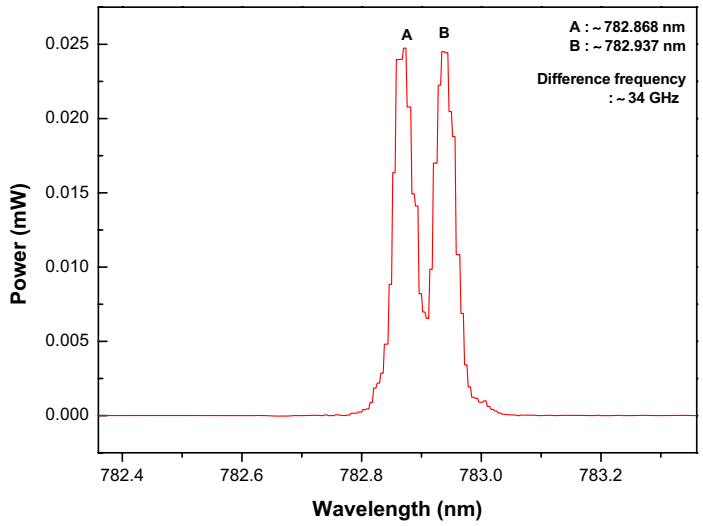

Figure 3.5.: Dual-mode spectrum observed using an optical spectrum analyzer. The difference frequency is 34 GHz.

mixing product from the photodetector.

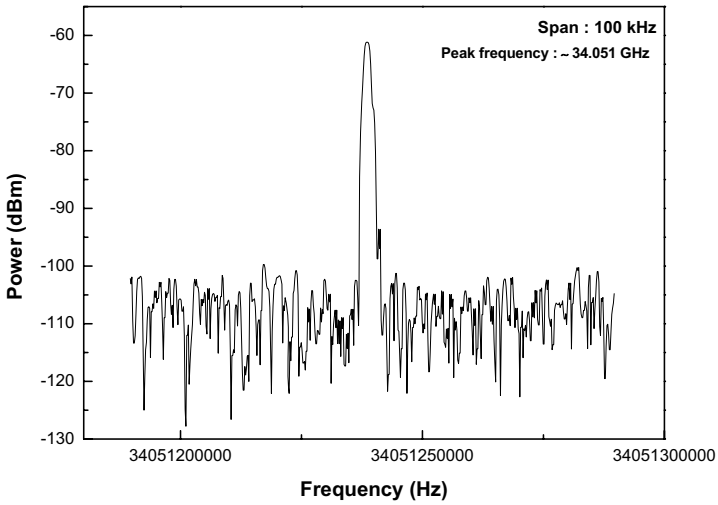

Figure 3.6.: 34 GHz mixing product spectrum. The spectral width is $\sim$ 6 kHz at 100 kHz span with the resolution bandwidth of 910 Hz.

In order to prove that we really have only one mixing product of two modes a spectral region of 500 MHz with 3 MHz resolution bandwidth is shown in figure 3.8. It only contains one spectral peak and no other intermodulation products. This means that each overlapped transmission peak passed only one longitudinal mode. Had more modes passed the etalons then the spectrum would contain

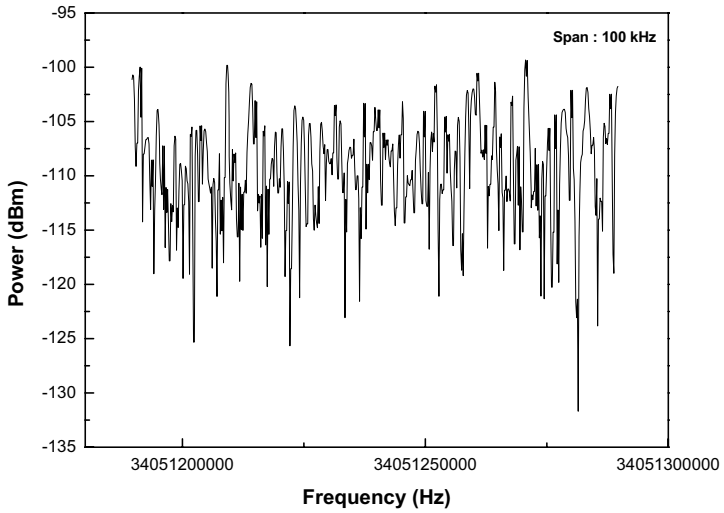

Figure 3.7.: Noise spectrum from the spectrum analyzer at 100 kHz span with the resolution bandwidth of 910 Hz.

additional lines shifted by $\sim$ 184 MHz from the center frequency. In order to confirm the significance of the signal, the noise level at 500 MHz span was measured (figure 3.9). Compared to this noise level the beat signal is well 15 dB above the noise.

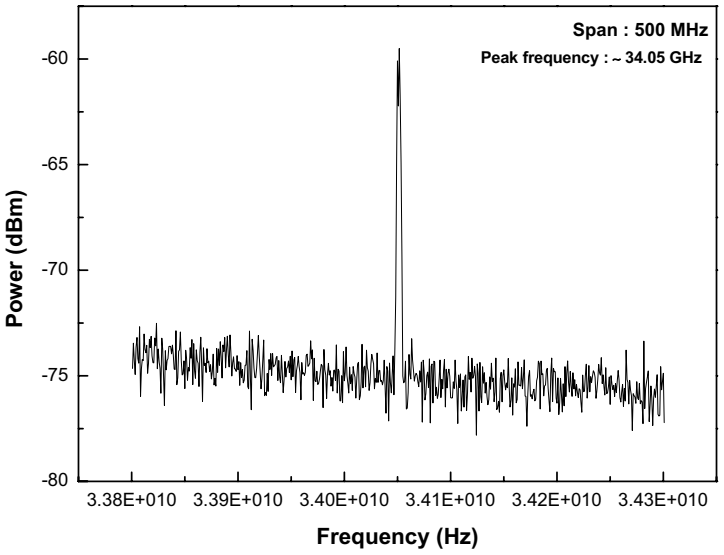

Figure 3.8.: 34 GHz mixing product spectrum at 500 MHz span with the resolution bandwidth of 3 MHz.

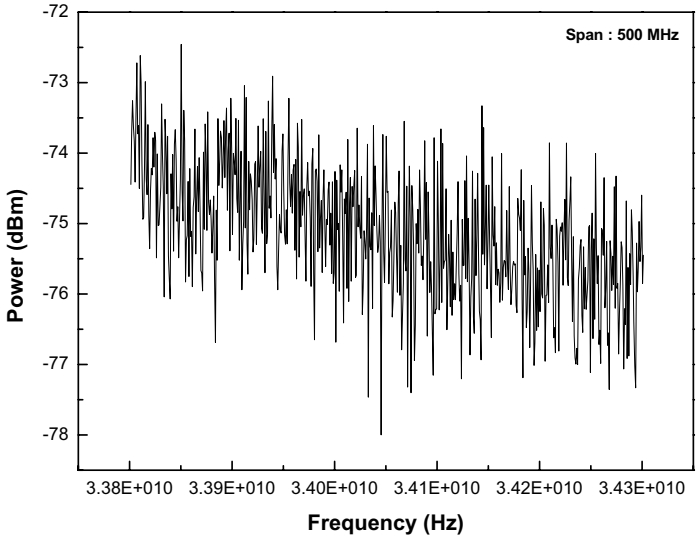

Figure 3.9.: Noise spectrum from the spectrum analyzer at 500 MHz span with the resolution bandwidth of 3 MHz.

3.3.3. Frequency Stability

To measure the frequency stability of the 34 GHz mixing product, the frequency variations over time during a three-hour period were taken, the frequency spectrum was recorded six times over the three hours as shown in figure 3.10. The maximum variation was about 50 kHz from spectrum A to spectrum C. The mixing product drifted to a higher frequency during the first ~ 90 minutes and then drifted to a lower frequency.

The main reason for the frequency drift is most likely thermal expansion of the etalon. Thus I calculated the shift of the transmission peak and changes in the FSR of the etalon by the following equation (refer to equation 2.11)

$$I = I_0 \frac{(1-R_1)(1-R_2)}{(1-\sqrt{R_1R_2})^2 + 4\sqrt{R_1R_2}\sin^2(\phi/2)} \tag{3.2}$$

where I_0 is the intensity of the incident ray into the etalon, R_1 and R_2 are the reflectivities of the etalon surfaces and the optical phase, ϕ, is given by

$$\phi = 4\frac{\pi n(T) d\cos(\theta)}{\lambda} \tag{3.3}$$

and the refractive index change with temperature is given by

$$n(T) = n(T_0)[1 + \beta(T - T_0)]. \tag{3.4}$$

where $n(T_0)$ is the refractive index at the standard temperature and β is the temperature coefficient of the refractive index in units of ppm/°C. The FSR shift with temperature can be obtained easily as

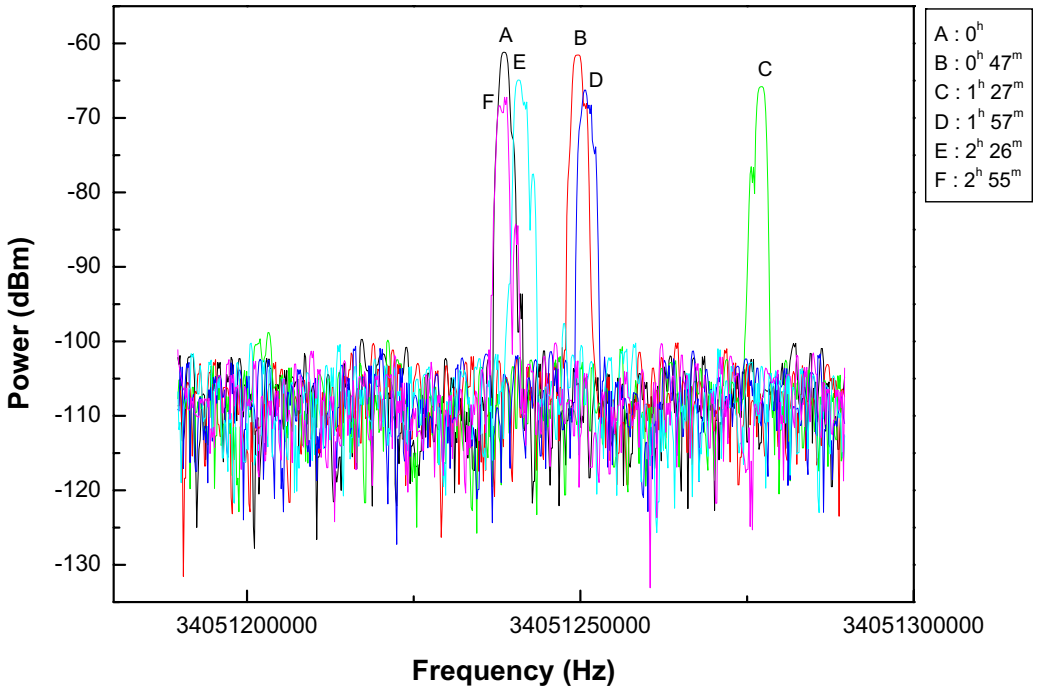

Figure 3.10.: Frequency drifting function as time. The maximum frequency drifting is 50 kHz during three hours at a room temperature of 20 °C with variation of ± 0.5 °C. The times are elapsed time since the beginning of the monitoring period.

$$FSR(T) = FSR(T_0)[1 - (\alpha + \beta)(T - T_0)]. \tag{3.5}$$

In case of the fused silica, the thermal expansion coefficient, α, is 0.55 in units of ppm/°C and the thermal refractive index coefficient β is 6.57 in units of ppm/°C. I assumed the standard temperature, T_0, is 20 °C. Using equation 3.5, I obtained a change of 246.54 kHz for a 3 mm etalon and 61.63 kHz for a 12 mm etalon when the temperature changed by 1 °C. However, the FSR was decreased when the temperature was increased. But both etalons have the same thermal expansion coefficient and so the transmission peaks (3 mm and 12 mm) are always overlapping.

From these results, we can expect that the frequency stability is very sensitive to temperature variation. This experiment has been done in the laboratory in which the room temperature was roughly 20 °C ± 0.5 °C. However if the temperature had variations as high as ± 1 °C then this dual-mode laser system will require a temperature stabilization system for the etalon.

3.4. Summary

The 34 GHz beat frequency between two modes from the Ti:Sapphire laser was observed using a commercial photodetector. To filter two modes in the multi-mode ring resonator, I used two internal etalons made from fused silica with a refractive index of 1.444 at 1550 nm. The thicknesses of the

etalons were 12 mm and 3 mm. The 3 mm etalon determined the beat frequency and the 12 mm etalon suppressed modes by mode competition. The optical components were installed on an Invar bar, which had a low thermal expansion coefficient. Invar alloy has been widely used in the industrial field where low thermal expansion is required (Wang et al. 2004) taking advantage of its low thermal expansion coefficient at room temperature (about $0.07 \times 10^{-6}/^{\circ}$C) (Roy et al. 1989).

From the observed spectrum, the spectral width of a 34 GHz beat frequency was $\sim$ 6 kHz at 100 kHz span and only one mode transmitted through the each overlapped transmission peak of combination of 3 mm and 12 mm etalon transmission curves. The 34 GHz beat frequency drift was $\sim$ 50 kHz maximum during the three hours. The reason for the frequency drift was most likely thermal expansion of the etalons. By the calculated results for the refractive index change as a function of temperature, assuming that the thermal effect of air in the ring cavity is zero, one expects the FSR shift by 246.54 kHz per 1 °C. Room temperature typically varied within $\pm$ 0.5 °C.

The drift of the beat frequency was within quite a small range and so the short-term frequency stability was good. But if the room temperature changes by more than 0.5 °C then a frequency stabilization system is required or the etalons could be made from low thermal expansion material instead of fused silica. Berthold et al. (1977) and Houwman et al. (2006) presented the frequency drift using etalons of low thermal expansion material. In the case of Berthold et al. (1977), they measured cavity length change with temperature of two types of fused silica, ULE, Zerodur, Invar and Super Invar materials. Houwman et al. (2006) fabricated a diamond solid etalon and measured the shift of the transmitter frequency as a function of temperature. Both groups found the transmission peak frequency (less than 10 MHz / 40 °C, see more detail figure 1 in Houwman et al. (2006)) and length of cavity (less than 1×10^{-9} mm / day) did not change much with temperature. Therefore to improve the frequency stability against temperature variation, I suggest using a low thermal expansion etalon such as diamond for the solid etalon or a vacuum air-spaced etalon mounted in a holder made from low thermal expansion material such as Invar or Zerodur for the mode selection components.

4. Generation of 100 GHz Radiation using the Dual-Mode Ti:Sapphire Laser and a LT-GaAs Photomixer

4.1. Introduction

Up to now millimeter- and submillimeter-wave heterodyne mixers based on SIS junctions have used LO sources that consist of Gunn diodes or YIG oscillators followed by multiplier chains consisting of doublers or triplers. Recently, the photonic LO based on the photomixing technique was demonstrated. The first experiment was done at 50 GHz (Brown et al. 1993a) but it was shown that performance up to 5 THz can be achieved (McIntosh et al. 1995). The advantage of the photonic LO technique is the inherent wide tunability that is limited only by the geometric structure and carrier recombination life-time of the semiconductor of the photomixer used, the limitation is mainly the antenna that radiates the LO signal. The disadvantage is the relatively low conversion efficiency (Tani et al. 2005).

Figure 4.1 shows a schematic illustration of the photomixer device. The photomixer chip is mounted on the flat side of a Si hemispherical lens made from high resistivity silicon. In this section I demonstrate that a 100 GHz LO signal can be generated by illuminating the photomixer with a tuned dual-mode Ti:sapphire laser.

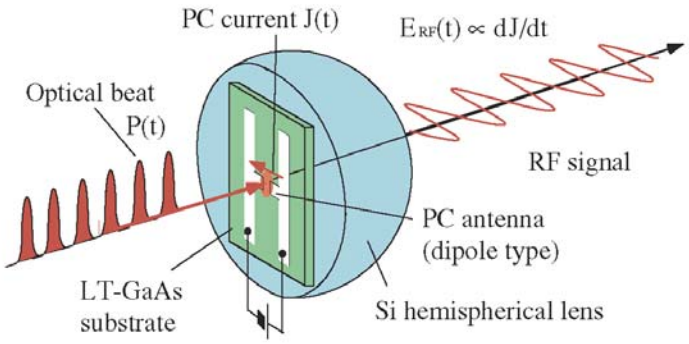

Figure 4.1.: Schematic illustration of the operation of a photomixer photoconductive antenna for CW RF wave generation. Modified from Tani et al. (2005).

4.2. Experimental Set-up

A schematic view of the experiment is shown in figure 4.2. Two solid Fabry-Perot etalons were installed inside the ring cavity: one has a thickness of 1mm and a reflectivity, R of 30 % on both sides, the other has a thickness of 10 mm and R = 20 %. The flatness deviation is less than $\lambda/10$. The etalons were fabricated by B. Halle GmbH in Berlin, Germany. The etalon material was fused silica with a refractive index of 1.444 at 1.5 μm wavelength. The specifications of the etalons are given in table 2.4. The beat frequency was determined by the free spectral range of the thin etalon. As the installation of the etalons inevitably contributes to the cavity losses, care was taken to select proper reflectivities to optimize throughout at optimum finesse. Final frequency tuning of the etalons was done by a fine tilting mechanism (fine-pitch micrometer and piezo actuators (PZT)). At the output of the Ti:sapphire laser the signal was coupled into a 1.5 m long fiber (single-mode). To check the laser spectrum an Anritsu MS9710C optical spectrum analyzer was used.

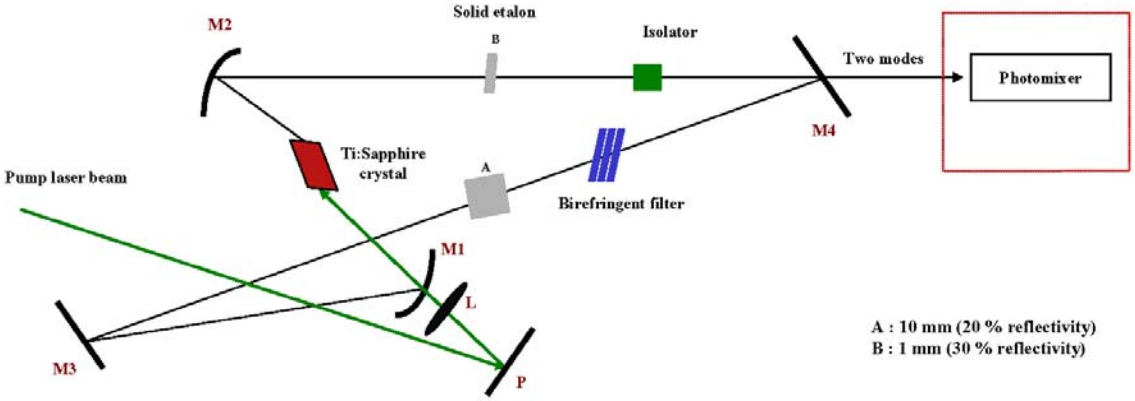

Figure 4.2.: Schematic overview of the experimental setup. To operate the dual-mode laser, two solid etalons were installed as intracavity etalon. The two modes passed by the filters were coupled into the photomixer.

The dual-mode laser output was coupled into the fiber and was guided to the photomixer as shown in figure 4.3. The spectral quality of the beat frequency generation is largely dependent on the purity and beam properties at the end of the fiber. Note that the end of the fiber was very precisely positioned with respect to the photomixer chip by using a nanocube from Physik Instrumente. A calibrated Golay cell with an overdimensioned Winston corn horn (not specially optimized to a certain frequency) and a cut-off filter for visible and NIR light was used to measure the power of the emitted beat frequency signal. A chopper was placed in front of the fiber coupler as shown in figure 4.3. A lock-in amplifier handled the signal from the Golay cell thus avoiding any influence from thermal background radiation. The optical response of the Golay cell was 19.3 kV W^{-1} and the detector optical noise equivalent power (N.E.P.) was 1.9×10^{-10} W Hz$^{-1/2}$ according to calibration documents.

Figures 4.4 and 4.5 show a typical photomixer device developed at the Max-Planck Institute for Radioastronomy (MPIfR) and the Golay cell with horn antenna. The photodetector chip was de-

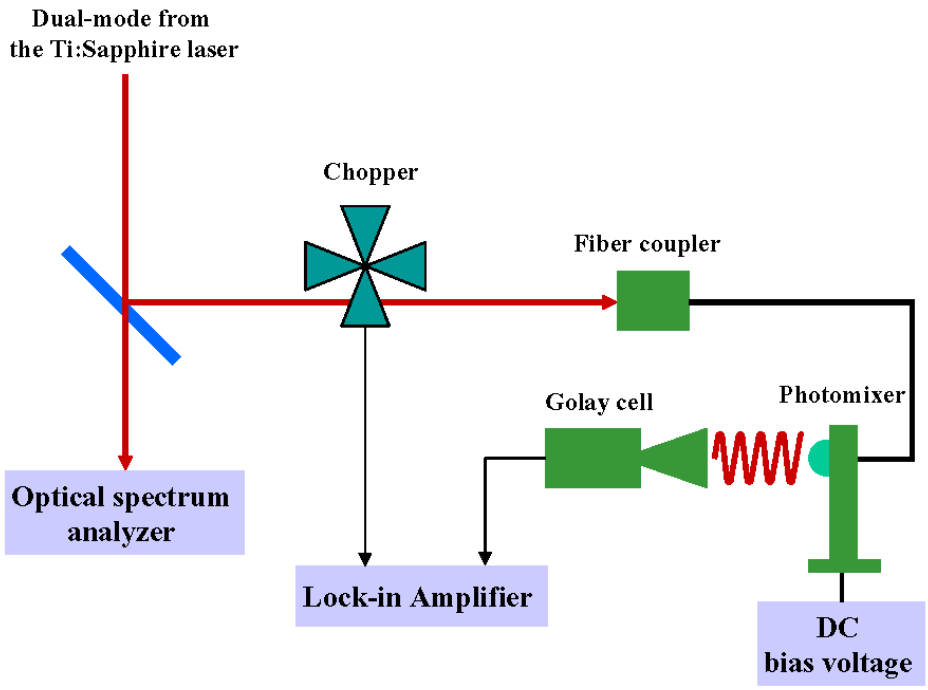

Figure 4.3.: Schematic overview of the radiation power measurement setup.

signed at the MPIfR and processed on a GaAs-wafer at the Research Center Jülich (Mikulics (2004), Adam et al. (2004), Mayorga et al. (2004)).

In general, the emitted beat frequency power generated in a photomixer is quadratically increasing with the applied bias voltage as described by Brown et al. (1993b).

$$P(\omega) = \frac{\frac{1}{2}(J_0)^2 R_L}{[1+(2\pi f\tau)^2]\cdot[1+(2\pi f R_L C)^2]} \tag{4.1}$$

where J_0 ($= G_0 V$) is the DC photocurrent, G_0 is the time-averaged photoconductance of the photomixer, V is the bias voltage, R_L is the antenna input resistance, C is the capacitance of the finger structure, τ is the photocarrier life-time and f is the difference frequency (or beat frequency). This expression is valid for $G_0 R_L \ll 1$ and assuming that both input optical beams have identical power. The beat frequency output power is proportional to the radiation resistance of the antenna, the square of the DC conductance (G_0^2) and to the square of the bias voltage, V^2.

The 100 GHz radiation generated from the photomixer radiates through the dipole antenna and Si hemispherical lens. To monitor the radiation power, the Golay cell with horn antenna was installed as shown in figure 4.5.

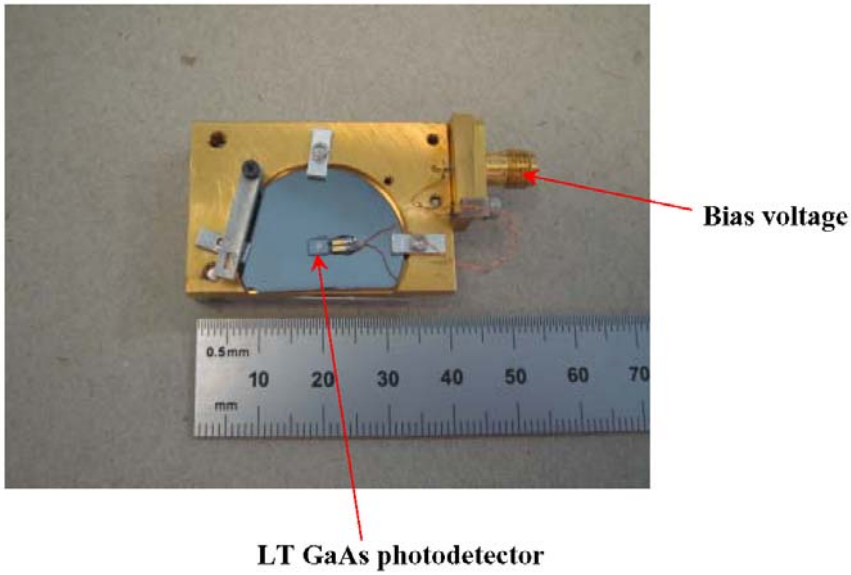

Figure 4.4.: Front view of the photomixer block.

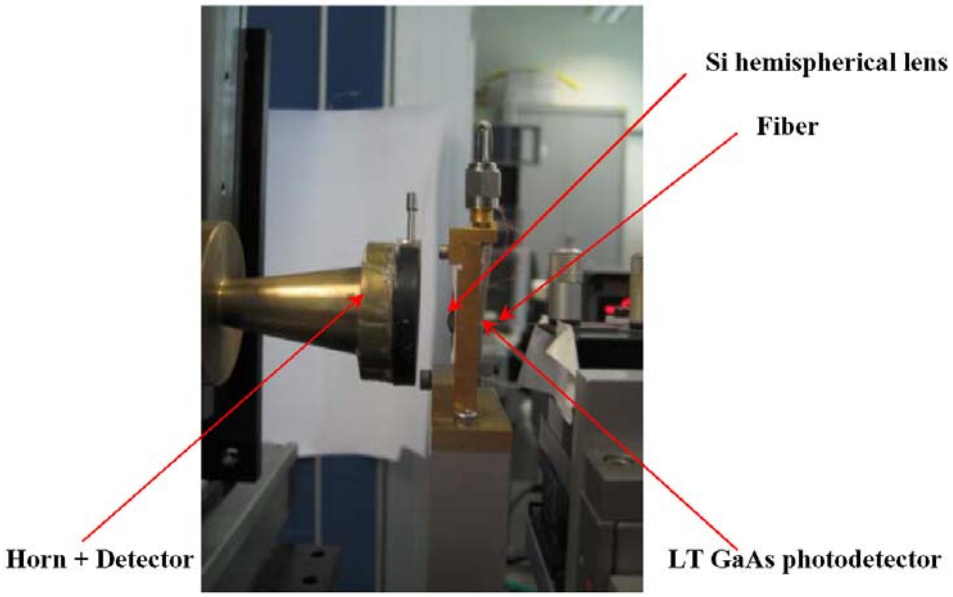

Figure 4.5.: System for the detecting power of the mixing product from the photomixer. The input laser signal is coupled into the LT GaAs photodetector through the single-mode fiber and the generated beat frequency radiates from the Si hemispherical lens to the Golay Cell.

4.3. Results

The output power of the Ti:Sapphire laser with intracavity etalons was around 200 mW at maximum. The input laser power at the photomixer was only about 35 mW due to the losses in coupling to the fiber. Figure 2.25 shows the dual-mode spectra obtained with two intracavity Fabry-Perot etalons. Two etalons of different thickness were used to achieve dual-mode operation. The ratio of intensity between the two modes depended on the alignment of the etalon.

The emitted CW 100 GHz radiation power was measured by the Golay cell. Figure 4.6 presents the measured output power as a function of the bias voltage applied to the photomixer. As shown in the figure 4.6, the measured output power generated in the photomixer increased with the applied bias voltage. The errors, 20 %, were caused by the power variation between the two modes. The intensity ratio between two modes could be optimized by alignment of the resonator mirrors and intracavity etalons but still suffered from mode competition between the photons and suffered from the variation in temperature of the resonator, air fluctuation and mechanical vibration. Taking the errors into account, a linear increase of beat frequency power with bias voltage is visible in the fit. This linear behavior is confirmed in figure 4.7, which was obtained with two tunable diode lasers. However, the input laser power at the photomixer and photomixer itself were different in both setups. Therefore the slopes of figure 4.6 and 4.7 are different.

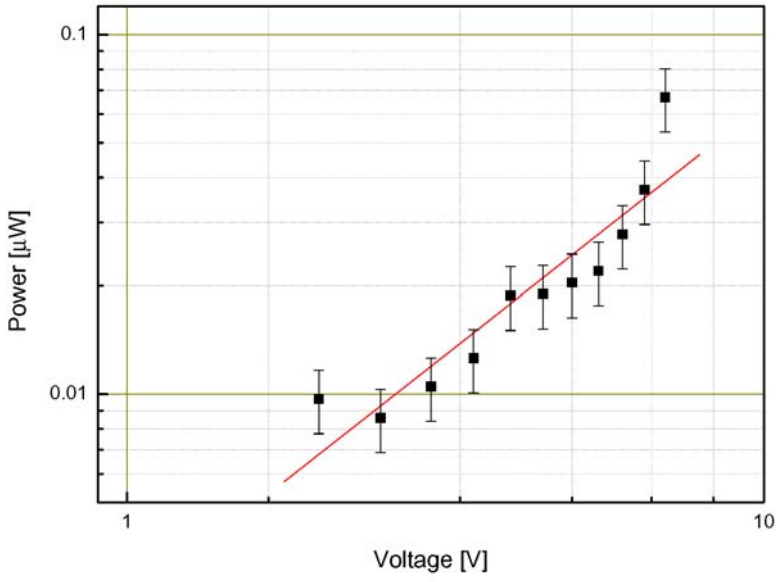

Figure 4.6.: 100 GHz output generated by the photomixer as a function of the photomixer bias voltage at a room temperature of 21 °C. The input dual-mode laser power was 35 mW.

The maximum radiation power was 0.07 μW at the applied bias voltage of 7 V when the input laser power was around 35 mW. In this experiment, the main motivation was to demonstrate that a beat frequency signal was generated with a frequency of 100 GHz with a dual-mode laser. Damaging of the photomixer by excess laser power or too high bias voltage was avoided at all times. Therefore, the conversion efficiency was lower than can be expected for a higher laser power and bias voltage.

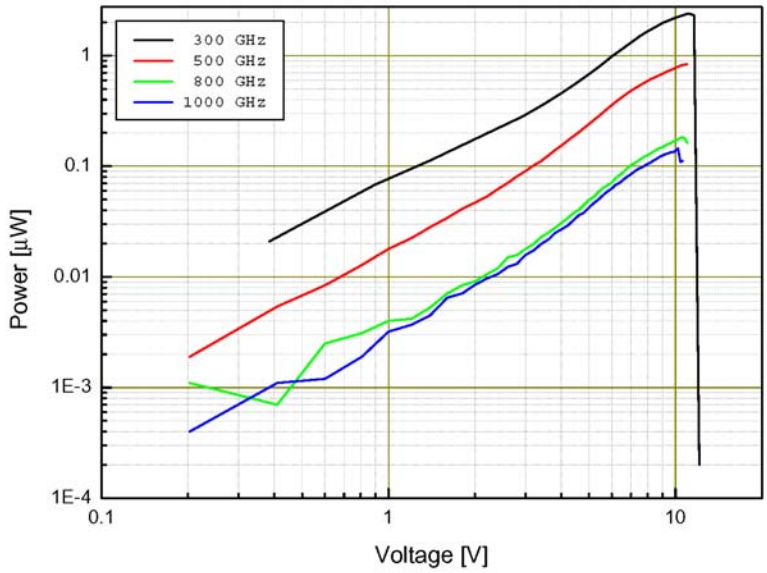

Figure 4.7.: The photomixer output powers as a function of the bias voltage. Two tunable diode lasers were used (Camara, priv. com.).

The conversion efficiency is defined as $\varepsilon = \frac{P_\omega}{P_0}$, where P_ω is the radiation power from the photomixer, and P_0 is the total incident laser power of $P_1 + P_2$. Conversion efficiency depends on the applied bias voltage (see equation 10 in Brown et al. (1993b)) assuming that the other mixer parameters are constant. To increase the conversion efficiency, the bias voltage should be optimized to the maximum value and the input laser power should be high enough.

4.4. Summary

It was demonstrated that a dual-mode Ti:Sapphire ring cavity laser can be used to generate a CW 100 GHz beat frequency in LT-GaAs photomixer. The power of the 100 GHz radiation as a function of the applied bias voltage was measured by a Golay cell with horn antenna. The experiment has been done in a room temperature of 21 ^{o}C and the Ti:Sapphire ring cavity was in open contact with the laboratory atmosphere.

A maximum power of 0.07 μW was obtained at a bias voltage of 7 V with an input laser power of around 35 mW. From the results, the beat frequency power as a function of applied bias voltage increased linearly with uncertainties of 20 %. The main reason for the errors was the continuous peak intensity variation (approximately 10 dB fluctuations) between the modes caused by mode competition of the photons in the laser cavity and changes in the resonator condition due to air fluctuations, temperature variations and mechanical vibrations. To reduce these intensity fluctuations, a power stabilization system should be applied as proposed in the next chapter.

5. Power Stabilization of the Dual-Mode Laser using Volume Holographic Gratings

5.1. Introduction

The dual-mode power from the Ti:Sapphire ring cavity laser with intracavity etalons was unstable. The power of each mode varied continuously. Generally, for the modes generated by the ring cavity, the main factors that contributed to the power instability were:

1) competition between modes in the ring cavity,

2) cavity length and refractive index drift due to thermal fluctuations, and

3) mechanical vibrations, air fluctuations and dust particles influences.

As stated in section 4, power fluctuations contributed to instability of the radiation power from the photomixer. To improve the power stability we discuss two approaches;

1) A passive stabilization system stabilizes the resonator against thermal and mechanical influences using a housing.

2) An active stabilization system stabilizes the power using a closed feedback loop such as a phase-locking loop (PLL).

To demonstrate the active power stabilization system, the dual-mode output coming from the laser has to be separated into two single modes by an optical tunable filter. Available single-passband tunable filters are volume holographic gratings (Havermeyer et al. 2004), fiber Bragg gratings (Iocco et al. 1999), thin film filters (Lequine et al. 2002), Fabry-Perot filters (Stone & Stulz 1987), arrayed waveguide grating (Watanabe et al. 1997), accusto-optic tunable filters (Jackel 1996) and microelectro-mechanically-actuated tunable filters (Vail 1995).

In this experiment a volume holographic gratings (VHGs) was used to separate the two single wavelengths for individual power measurement because the VHGs is one of the easiest filters to separate the modes in the multi-mode operation and it selects only one mode. Most widely used VHGs are phase gratings with low absorption, fabricated in various media such as photo-refractive crystals, polymers, dichromated gelatin and photosensitive glasses (Ondax 2006). The power stabilization using the VHGs for the dual-mode laser was demonstrated and described in the following.

5.2. Theory of Volume Holographic Gratings

The VHGs is a diffractive element that consists of a periodic phase or absorption perturbation throughout the entire volume of the element as shown in figure 5.1. When the incident beam satisfies the Bragg phase matching condition it is diffracted by the periodic perturbation (Ondax 2006) but the other wavelengths pass through the filter (Hsieh et al. 2004). The Bragg wavelength of the holographic grating is determined by

$$\lambda_{\mathrm{b}} = 2n(T_0)\Lambda(T_0)\cos\theta_{\mathrm{n}}, \tag{5.1}$$

where λ_{b} is the Bragg phase matching wavelength, $n(T_0)$ is the refractive index of the material at temperature T_0, $\Lambda(T_0)$ is the holographic grating period at T_0, and θ_{n} is the angle of the beam inside the holographic material. By changing the incident angle, θ_{n}, the Bragg wavelength can be tuned continuously from $2n\Lambda$ down to $2\Lambda\sqrt{(n^2-1)}$ (Havermeyer et al. 2004).

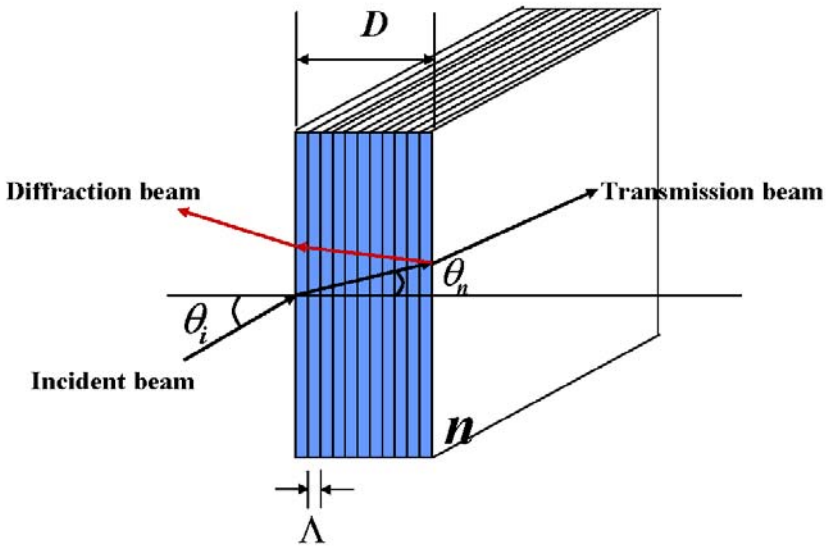

Figure 5.1.: The reflection VHGs, the frequency-reflected beam is reflected to the same side of the grating as the incident beam.

When the temperature changes to $T_0 + \Delta T$ then the Bragg wavelength is shifted by the relation:

$$\lambda_{\mathrm{b}}(T_0 + \Delta T) = 2n(T_0 + \Delta T)\Lambda(T_0 + \Delta T)\cos(\theta_{\mathrm{n}} + \Delta\theta) \tag{5.2}$$

where $\Delta\theta$ is the angle selectivity of a reflective grating and is given by $\Delta\theta = \lambda/(2n\sin\theta_{\mathrm{n}}D)$, where D is the effective length of the grating. The angle selectivity improves as the tuning incident angle θ_{n} increases. When $\Delta\theta$ is comparable with or smaller than the Gaussian angular deviation, part of the Gaussian beam will not be Bragg matched (Havermeyer et al. 2004). The affected wavelength range, $\Delta\lambda$, is inversely proportional to the thickness D of the grating and is given by as (Blais-Ouellette et al. 2006)

$$\frac{\Delta\lambda}{\lambda_{\mathrm{b}}} = \frac{\Lambda\cot(\theta_{\mathrm{n}})}{D}. \tag{5.3}$$

5.3. Experimental Set-up

The schematic overview of the dual-mode power stabilization is shown in figure 5.2. The Ti:Sapphire laser with the intracavity Fabry-Perot etalons had a ring configuration as shown in the figure. The effective round trip cavity length was 1.6 m. The direction of circulation of the light was determined by an optical diode (Faraday rotator) and so reduced the interference effect between clockwise trip photons and counter clockwise photons. Two modes were filtered by adjusting a birefringent filter with FWHM of 1.7 THz and two intracavity Fabry-Perot etalons with specifications shown in table 2.4. Final frequency tuning of the etalons was done by a fine tilting mechanism (fine pitch micrometer and PZT). Again the dual-mode spectrum was analyzed with an Anritsu MS9710C optical spectrum analyzer.

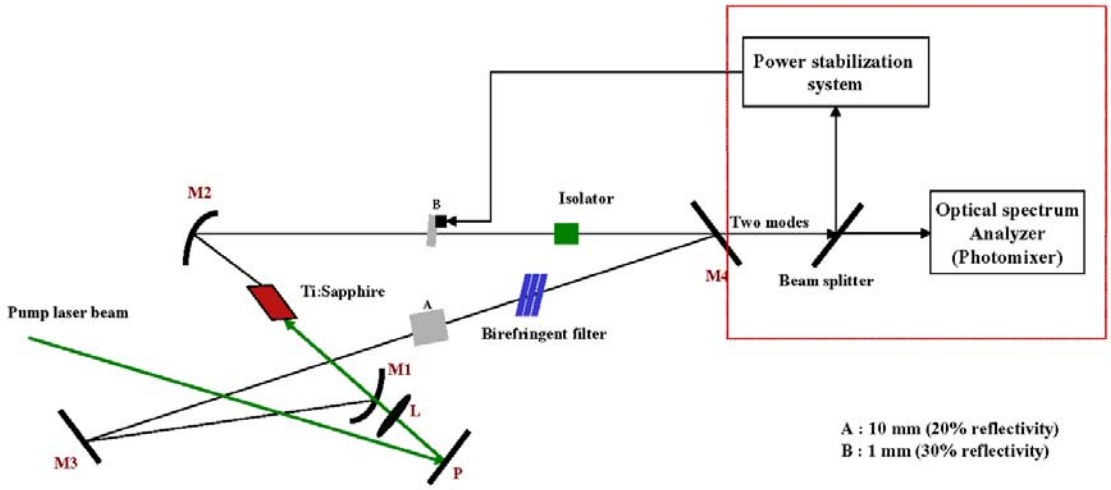

Figure 5.2.: Schematic overview of the Ti:Sapphire ring cavity with intracavity mode selection components and power stabilization system.

The filtered two modes were directed into the power stabilization system. Figure 5.3 shows a schematic overview of the power stabilization configuration using the VHGs (Ondax Inc.). The laser beam from the Ti:Sapphire laser was split by the beam splitter, 10 % of which was passed to the optical spectrum analyzer and reflected, the other 90 % to the power stabilization system. The λ_1, λ_2 first passed through the 20 Hz chopper into the first VHGs with a reflectivity of 45 % and with a resolution bandwidth of 0.2 nm. There, 45 % of the power at λ_1 was diffracted from the VHGs to the photo diode (D1). λ_2 and the rest of λ_1 were transmitted through the first VHGs to the second VHGs, which had a reflectivity of 45 % and a resolution bandwidth of 0.2 nm. There, 45 % of the power at λ_2 was diffracted and went to the photo diode (D2). The detected powers A and B fed to the lock-in amplifier (LIA) which performed a phase detection of A-B using the chopper reference signal. At the output of the LIA, the DC signal was proportional to A-B and was used (including polarity) as an error signal. This was fed into the proportion-integration (PI) controller with an integration time of 1 ms. The PI controller output controlled the tilt of the thin etalon via the PZT.

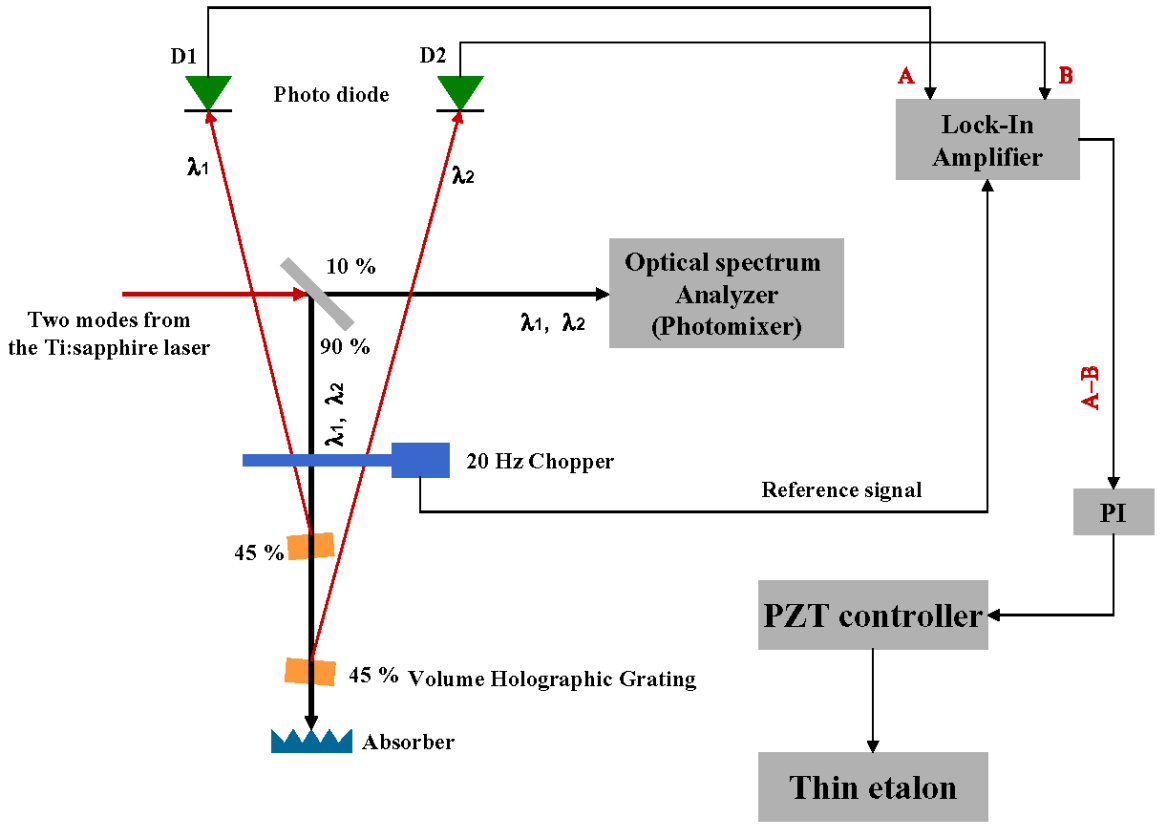

Figure 5.3.: Schematic configuration of the power stabilization system using the VHGs.

The main difficulty in this setup was to optimize the angle of each VHGs. One must carefully distinguish between the weak reflection from the front surface of VHGs and the diffracted beam.

5.4. Experimental Results

5.4.1. Spectral Bandwidth of the VHGs

A tunable diode laser was used to characterize the spectral behavior of the VHGs with a resolution of 0.005 nm. The result is shown in figure 5.4. The spectral bandwidth was approximately 0.2 nm (approximately 100 GHz). Figure 5.5 shows identical measurements at different angles of incidence (2°, 3.5°, 8° and 12°). As shown, the filter peak shifted to shorter wavelength with tilt angle increasing. Also, the spectral bandwidth became narrower with tilt angle increasing. These two results are described by the formulae 5.1 and 5.3.

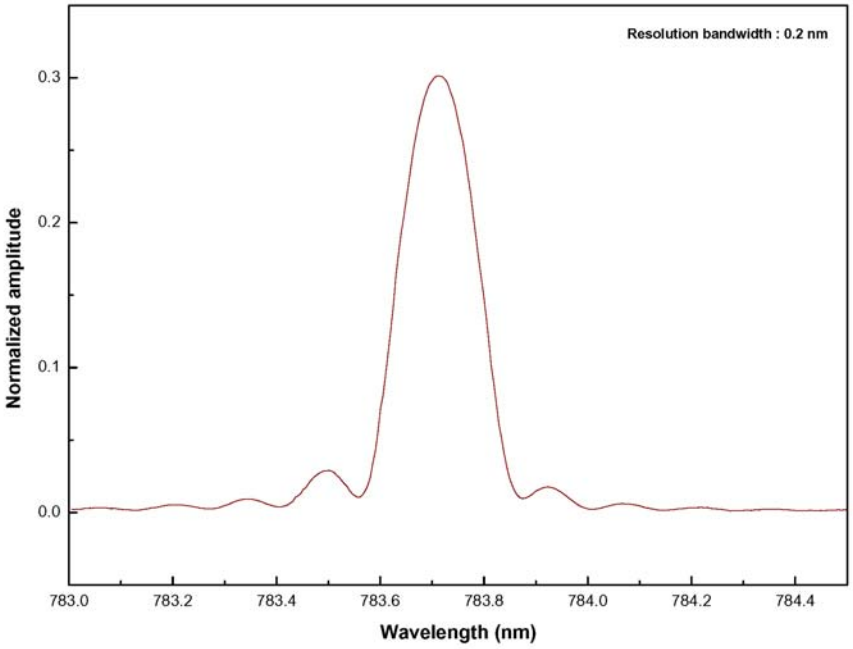

Figure 5.4.: Transmission curve of the VHGs. The scanning laser resolution bandwidth was 0.005 nm.

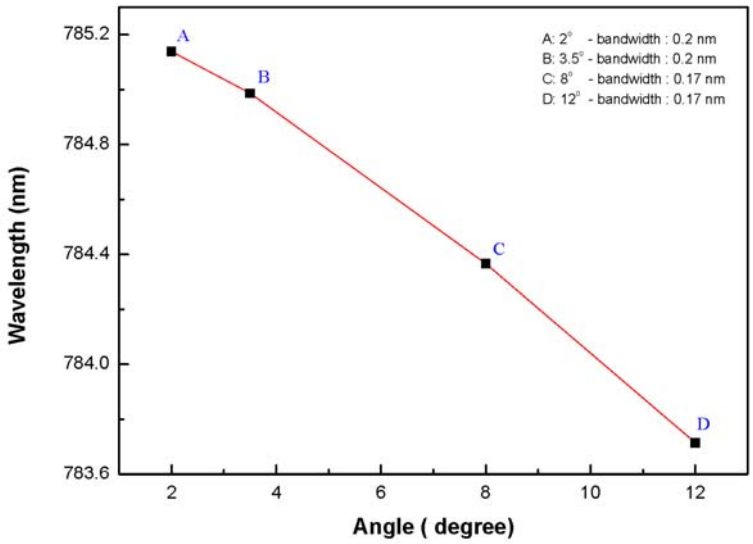

Figure 5.5.: The filtered wavelengths as a function of the tilt angle of the VHGs. The angles were 2°, 3.5°, 8° and 12°.

5.4.2. Dual-Mode Laser Operation

To select two modes in the multi-mode ring cavity laser, two intracavity etalons were installed as described in section 5.2. The difference frequency between the modes was 100 GHz, determined by the FSR of the thin etalon. The spectrum observed by the optical spectrum analyzer is presented in figure 2.25.

5.4.3. Power Stabilization using the VHGs

A typical error signal of the output PI controller is shown in figure 5.6. It was recorded by a National Instrument Data Acquisition system (NI DAQ) controlled by a LabView program. The integration time was 1 ms. The error signal depended on A-B and was fed back to the PZT controller to make a fine adjustment to the tilt of the thin etalon. The adjustment maintained the transmission peak of the thin etalon aligned in frequency within the transmission peak of the thick etalon (see figure 2.15). Figure 5.7 show the peak power difference between two modes recorded for 600 s long periods by the optical spectrum analyzer controlled by LabView. The integration time was 1 s. In the case of operation without the power stabilization system, the fluctuating power difference was $\sim$ 10 dB with occasional excursions to 30 dB. As presented in the figure, the power difference with the power stabilization was less than 3 dB except for a few moments. It is clearly shown that the power stability was improved when the power stabilization system was on. By comparing figures 5.6 and 5.7, one notes that the times of the peaks are identical. However, the peaks that appear indicate single-mode operation for very short periods of time. An explanation of this behavior is hard to give here.

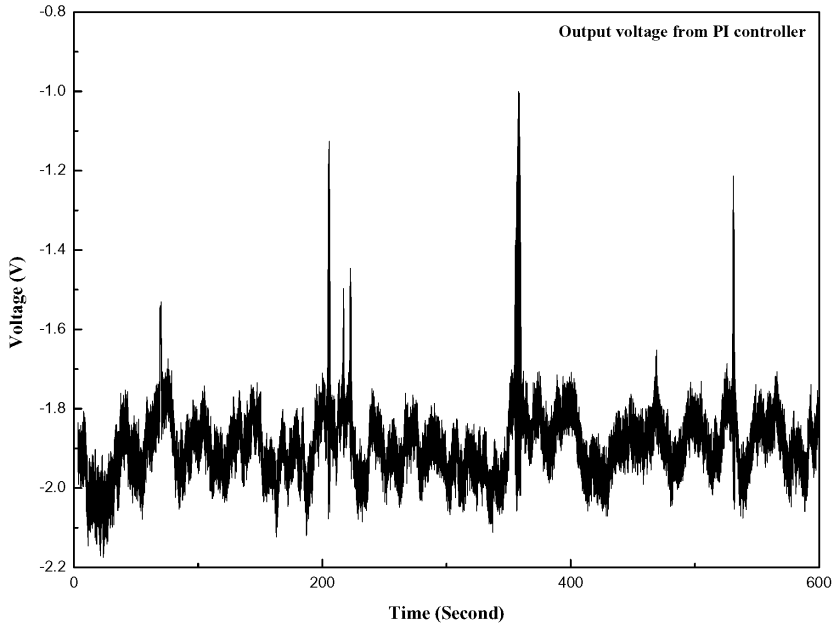

Figure 5.6.: The output voltage from the PI as a function of time. The output voltage was recorded by LabView program developed by NI (National Instrument Inc.) with the integration time of 1 ms.

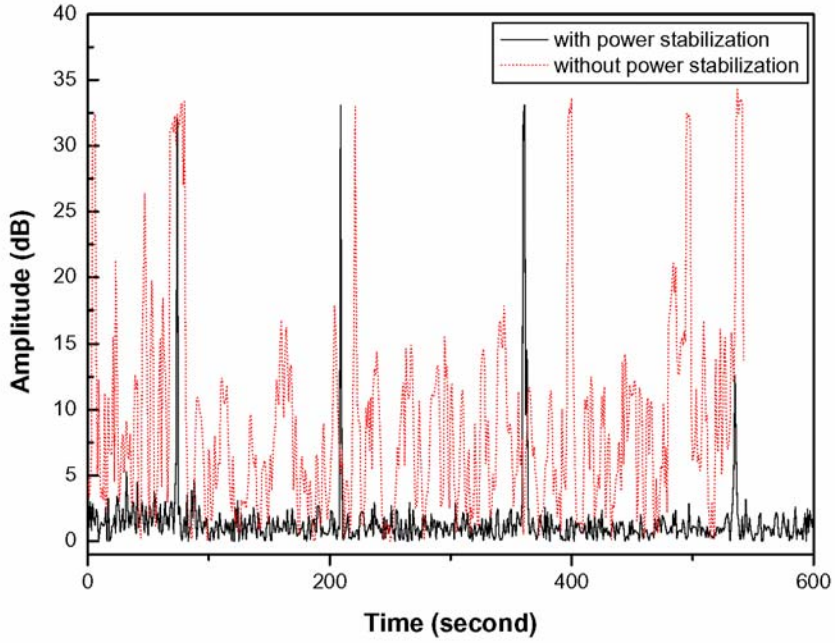

Figure 5.7.: The power difference between two modes with and without the power stabilization system recorded by LabView program with the integration time of 1 s.

5.5. Summary

Two longitudinal modes were filtered by the intracavity etalons in the ring cavity. Air fluctuations, thermal fluctuations and mode competition between the photons contributed to power instability, causing continuous power fluctuations. A power stabilization experiment using the two VHGs with 45 % reflectivity improved stability dramatically. Without stabilization system, the power difference between two modes fluctuated by $\sim$ 10 dB with occasional 30 dB excursions. With the power stabilization system, fluctuations were less than 3 dB except for a few moments. To confirm that the feedback loop was working, the output voltage from the PI controller and the power difference between the two modes were recorded by LabView. As shown in figure 5.6 and 5.7, the error signal follows the power difference.

The power difference fluctuations were greatly reduced by the power stabilization system except for few moments. The events are so fast that the servo system could not react in time. Future improvements could be achieved by using a better stabilization system such as a thermally stabilized box, which would also help to reduce acoustic effects.

6. The Molecular Composition of an Oxygen-Rich Asymptotic Giant Branch Star

6.1. Introduction

6.1.1. The Final Stages of Stellar Evolution

In a main-sequence (MS) star, the stellar interior consists of the nuclear burning core and, going radially outward, the convection zone and the radiation zone. The energy is generated in the core and then transferred toward the surface either by radiation or convection depending on which is more efficient at the prevailing physical conditions.

When all hydrogen (H) is transformed into helium (He) in the core, the nuclear energy release stops and the core starts to resume gravitational contraction and its interior becomes hotter. Then the outer layers expand and become cooler, resulting in the star glowing redder. The star is now called a red giant. At one point, He fusion begins and, simultaneously, H-burning also occurs in a shell around the He core. In the Hertzsprung-Russell diagram (HRD) (see figure 6.1) the star evolves to a pulsationally unstable red giant star onto the Asymptotic Giant Branch (AGB). At this stage, mass loss from the evolved central star produces an expanding envelope. Further on, carbon (C) is fused in the core and then oxygen (O) (Yamamura et al. (1996), Fukasaku et al. (1994)).

6.1.2. Structure of AGB stars

The structure of an AGB star is that of a C and O core surrounded by He-burning and, further out, H-burning shells, and, around these, an enormous convective envelope. Following core He exhaustion, the ignition of the He-burning shell is accompanied by a large increase in the energy burning rate, at least for the more massive stars. This energy output causes the star to expand and the H-burning shell is extinguished. Regions progressively further inward become unstable to convection and, thus, the depth of the convective envelope increases, mixing the products of H-burning to the surface in what is called the *second dredge-up* (for masses above about 4 $M_{\odot}$). The He-shell forms and advances outward to meet the H-shell. When the second dredge-up occurs, it hastens the coming together of these two shells (Lattanzio & Frost (1997), Lattanzio (2002), see Habing & Olofsson (2003) for a comprehensive source on AGB stars).

After this, the output of the He-shell becomes unstable, resulting in a thermal pulse or shell flash. It is caused by the high temperature dependence of the He-burning reactions. Shell flashes are divided into four phases. During the *on* phase the He-shell provides the energy and drives a convective zone from the He-shell almost all the way to the H-shell. During the *power-down* phase the convection dies away and the star expands in response to the energy input from the He-burning. This expansion causes the outer regions to cool and the H-shell is essentially extinguished. During the second dredge-up, the bottom of the convective envelope moves inward and can penetrate the region which

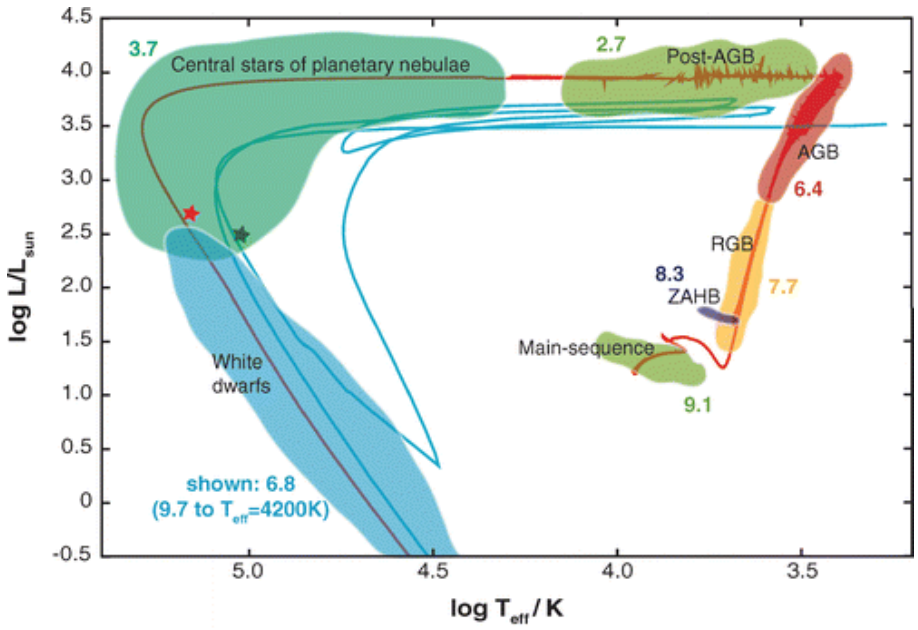

Figure 6.1.: In this Hertzprung-Russell diagram the red line traces the complete evolution of a star of mass 2 $M_{\odot}$ (Herwig 2005).

was previously part of the inter-shell convective zone. This is called the *dredge-up* phase, and it mixes the freshly produced C to the surface. Finally, the dredge-up stops, the star contracts again, the H-shell is reignited and the star enters the *off* or *inter-pulse* phase. During this the star is powered primarily by the H-shell with secondary energy provided by the He-shell. Instabilities in the outer envelope can cause AGB stars to pulsate on periods of several hundred days (Lattanzio 2002).

The structure of an AGB star is sketched in figure 6.2. An AGB star is made up of five regions: 1) the region just outside the stellar core where nuclear burning occurs, 2) the pulsating envelope of the star which includes H- and He-shells and, on the outside, the bulk of the stellar atmosphere, 3) the inner circumstellar envelope, 4) the main circumstellar envelope, and 5) the far outer envelope, which terminates in the interstellar medium (Glassgold 1996).

6.1.3. Characteristics of AGB stars

According to their evolutionary status, AGB stars are characterized by low surface temperatures, $T_* \leq 3000$ K, high luminosities up to several 10^4 $L_{\odot}$, by a peculiar chemical composition and their very large geometrical size (Habing 1996). The atmospheres of these giant stars provide favorable thermodynamic conditions for the formation of complex molecules, due to the low temperatures and, simultaneously, high densities. Once molecules reach a distance from the star at which the temperature is lower than the dust condensation temperature, rapidly dust is formed. Radiation pressure on the dust drives it away from the star. Molecules surviving dust formation are accelerated, too, due to dust-grain collisions (Goldreich & Scoville 1976).

In general, these highly evolved stars are surrounded by envelopes with expansion velocities of 5 $\mathrm{km\,s^{-1}}$ to 40 $\mathrm{km\,s^{-1}}$. They have high mass loss rates of 10^{-8} to $10^{-4}\,\mathrm{M_{\odot}\,yr^{-1}}$. The material lost

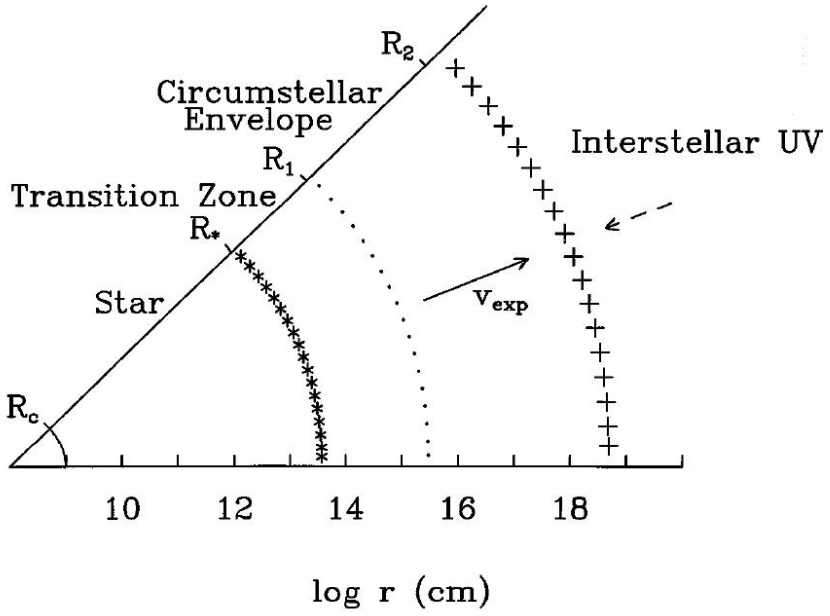

Figure 6.2.: Sketch of an AGB star. A slice of the star with the space divided into the star proper, circumstellar matter (an inner transition zone and the main circumstellar envelope), and the interstellar medium (Glassgold 1996).

during this period, enriched with nuclear material, complex molecules, and solid dust particles, is recycled to the interstellar medium. According to some sources, up to 90 % of the total dust mass returned to the interstellar medium is produced by star evolving along the AGB (Gehrz 1989).

6.1.4. Chemical Composition of AGB Star Envelopes

The chemistry of circumstellar envelopes of cool evolved stars is of considerable interest in the context of millimeter and infrared observations of a wide variety of molecules. The chemical reactions in circumstellar envelopes producing diverse molecules are a mixture of various types of reactions depending on the physical conditions. Typically chemical equilibrium reactions dominate in the high temperature ($T \sim 2000$ K), high density ($n > 10^{12}$ cm^{-3}) innermost region close to the stellar atmosphere.

The chemistry of the atmosphere and, further out, the circumstellar envelope (CSEs) around AGB stars is dependent on the chemical class (O-rich, C-rich, or in between). The stars are classified either as M stars (C/O < 1), S stars (C/O $\approx$ 1) or C stars (C/O > 1). The optical and infrared spectra of AGB stars show absorption from the stars$'$ atmospheres. M-type stellar spectra are dominated by lines of oxygen-bearing molecules, e.g., the metal oxides SiO and TiO, and H_2O. In C star atmospheres carbon-bearing molecules like, a.o., CH, C_2, C_2H_2 and HCN (see figure 6.3) are found. CO is easily observable in M-, S-, and C-stars (Tsuji (1964), Tsuji (1973)).

Further away from the star, once dust forms and density and temperature drop, the chemistry is determined by neutral-neutral (radical) reactions (in an intermediate region) and ion-molecular

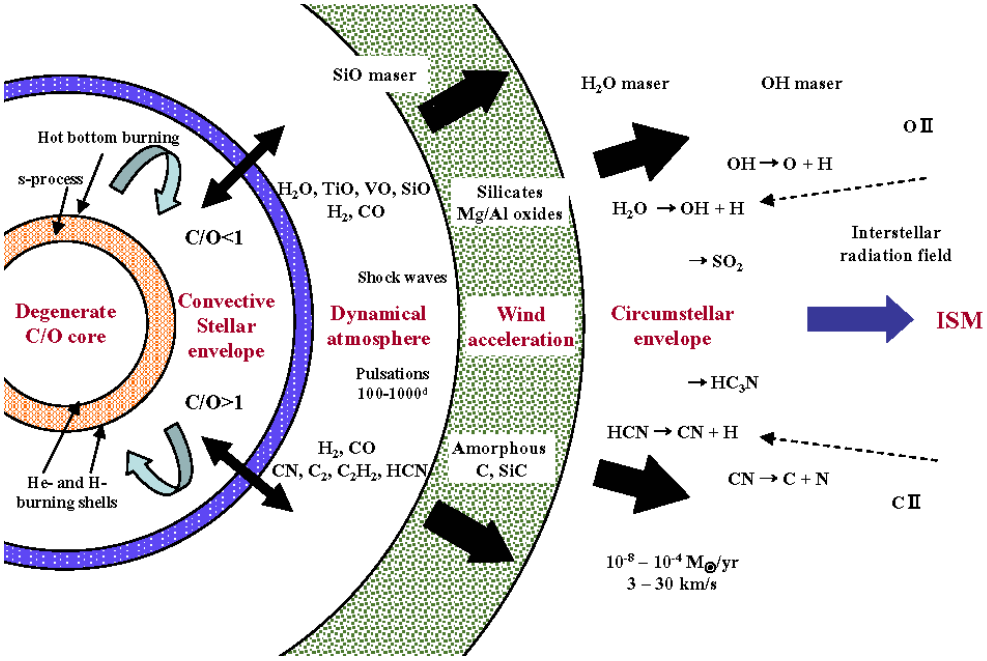

Figure 6.3.: Overview of an AGB star (Habing & Olofsson 2003).

reactions. In the latter regions, first, parent molecules begin to break down and recombine into other species. Further out, the daughter molecules reach their peak abundances. In the outermost regions, photons from the interstellar radiation field influence the chemistry and finally dissociate all the molecules (Willacy & Millar 1997). These regions are best observed by millimeter- and submillimeter-wavelength spectroscopy.

6.1.5. IK Tau

The Mira variable IK Tau, also known as NML Tau, is located at α_{2000}=$3^h53^m28^s.8$, δ_{2000}=$11°24'23''$. It was found to be an extremely cool star having large infrared (J-K) excess (Alcolea et al. 1999) consistent with a 2000 K black body. IK Tau shows regular optical variations with an amplitude of 4.5 mag.

IK Tau is an O-rich star of spectral type ranging from M8.1 to M11.2 (Wing & Lockwood 1973). Its distance was derived by Olofsson et al. (1998) to be 250 pc assuming a stellar temperature of 2000 K for their radiation transfer model of the IR excess. The pulsation period is $\sim$ 470 days (Hale et al. 1997). The systemic velocity of the star is 33.7 $\mathrm{km\,s^{-1}}$. Mass-loss rates estimated from the CO(J=1-0) line range from 2.4×10^{-6} $\mathrm{M_\odot\,yr^{-1}}$ (Olofsson et al. 1998) to 5.1×10^{-6} $\mathrm{M_\odot\,yr^{-1}}$ (Knapp & Morris 1985).

In the cicumstellar envelope of IK Tau maser emissions of OH (Bowers et al. 1989), H_2O (Lane et al. 1987), and SiO (Boboltz & Diamond 2005) and thermal emission of SiO, CO, SiS, SO, SO_2 and HCN have previously been found (Lindqvist et al. (1988), Bujarrabal et al. (1994) and Omont et al. (1993)). Obviously, IK Tau is a prime candidate for circumstellar chemistry studies.

6.2. Observation and Data Reduction

The observations were performed with the APEX (Atacama Pathfinder Experiment) 12 m telescope in Chile. At the 5100 m high APEX site on Llano de Chajnantor the amount of precipitable water vapour (PWV) is typically 0.5 mm but can in exceptional cases fall below 0.1 mm. The image in figure 6.4 shows the atmospheric transmission between 200 GHz and 900 GHz for different PWV values (see APEX homepage, http://www.apex-telescope.org).

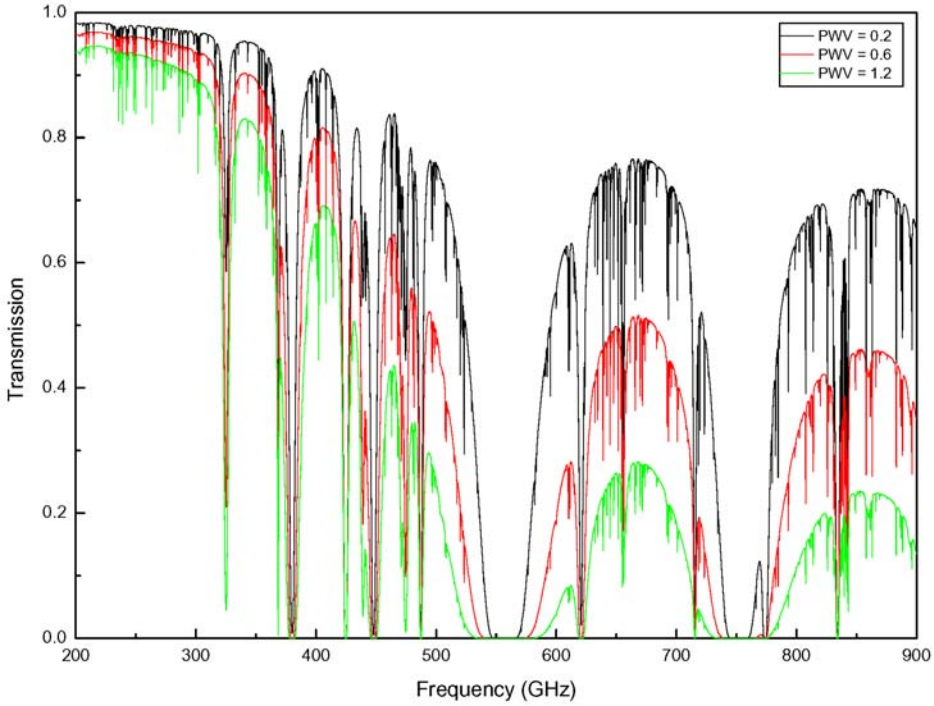

Figure 6.4.: Zenith atmospheric transmission on Llano de Chajnantor at 5100 m altitude for the frequency range from 200 GHz to 900 GHz for three different PWV values.

The data were obtained during observing periods in November 2005, April 2006 and August 2006. The receivers used were the facility APEX-2A and the MPIfR FLASH receivers (Heyminck et al. 2006). Typical system noise temperatures were about 200 K – 1000 K at 290 GHz and 350 GHz, 1000 K at 460 GHz and 5000 K at 810 GHz, respectively. The spectrometer for the observations were Fast Fourier Transform Spectrometers (FFTS) with 1 GHz bandwidth and the channel width for the 279 GHz and 381 GHz observations was approximately 122.07 kHz (8192 channels), and for the 460 GHz and 810 GHz observations 488.28 kHz (2048 channels). For the observations, a position-switching mode was used with the reference position typically 180″ off-source. The antenna was focused on the available planets. IK Tau itself was strong enough to serve as a pointing source, thus small cross scans in CO were done to monitor the pointing during the observations. The telescope beam sizes (HPBW) at frequencies of the observed molecular lines are shown in table 6.1. The antenna beam efficiencies are given in table 6.2 (Güsten et al. 2006).

The spectra were reduced using the CLASS package (Forveille et al. 1989). To calculate the

Species	Transition	ν (MHz)	HPBW (")
^{12}CO	3 - 2	345796.00	18
	4 - 3	461040.78	14
	7 - 6	806651.81	8
^{13}CO	3_2 - 2_2	330587.94	19
SiS	16 - 15	290380.31	21
	17 - 16	308515.63	20
	19 - 18	344778.78	18
	20 - 19	362906.34	18
SiO	7 - 6	303926.81	20
	8 - 7	347330.59	18
SO	7_7 - 6_6	301286.13	20
	8_8 - 7_7	344310.63	18
SO_2	$3_{3\,1}$ - $2_{2\,0}$	313279.72	20
	$17_{1\,17}$ - $16_{0\,16}$	313660.84	20
	$4_{3\,1}$ - $3_{2\,2}$	332505.25	19
	$13_{2\,12}$ - $12_{1\,11}$	345338.53	18
	$5_{3\,3}$ - $4_{2\,2}$	351257.22	18
	$14_{4\,10}$ - $14_{3\,11}$	351873.88	18
CS	6 - 5	293912.25	21
	7 - 6	342883.00	18
HCN	4 - 3	354505.47	18
^{29}SiO	7 - 6	300120.47	20
	8 - 7	342980.84	18
^{30}SiO	7 - 6	296575.75	21
	8 - 7	338930.03	18
CN	N=3 - 2, J=5/2 - 3/2	340031.56	18
	N=3 - 2, J=7/2 - 5/2	340247.78	18
H_2O	$10_{2\,9}$ - $9_{3\,6}$	321225.63	19
	$5_{1\,5}$ - $4_{2\,2}$	325152.91	19
^{28}SiO	V=1, 7 - 6	301814.30	20
	V=1, 8 - 7	344916.35	18
	V=3, 7 - 6	297595.41	20
^{29}SiO	V=1, 7 - 6	298047.33	20
^{30}SiO	V=1, 8 - 7	336602.44	19

Table 6.1.: Observed lines of each molecule and beam sizes (HPBW).

Receiver	Beam efficiency
APEX-2A 290 GHz	0.80
APEX-2A 350 GHz	0.73
FLASH 460 GHz	0.60
FLASH 810 GHz	0.43

Table 6.2.: Beam efficiencies of the each receivers used.

main-brightness temperature of the source ($T_{\rm MB}$) the following relation was used:

$$T_{\rm MB} = \frac{T_{\rm A}^*}{\eta_{\rm eff}} \tag{6.1}$$

Here $T_{\rm A}^*$ is the antenna temperature measured and $\eta_{\rm eff}$ is the antenna main-beam efficiency of APEX (see table 6.2). The molecular species were identified using the XCLASS program (Schilke, priv. com.).

6.3. The Observed Molecular Species toward IK Tau

Thirty four transitions from 12 molecular species including maser lines were detected with the APEX telescope toward IK Tau. The identified molecular lines are listed in table 6.1. Figures 6.5 to 6.9 display the spectra of the detected lines. The chemical formation processes of the detected molecules are described in Appendix B.

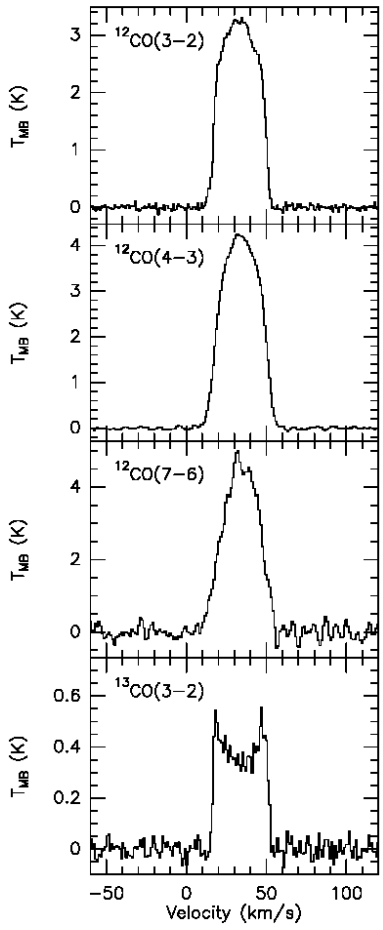

Figure 6.5.: Spectra of lines from the ^{12}CO and ^{13}CO molecules.

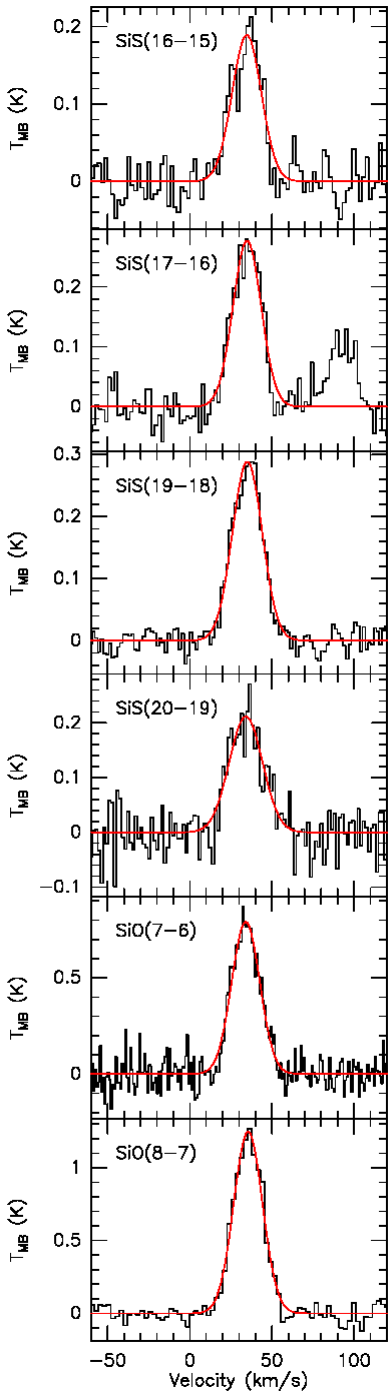

Figure 6.6.: Spectra of lines from the SiS and SiO molecules with Gaussian fits.

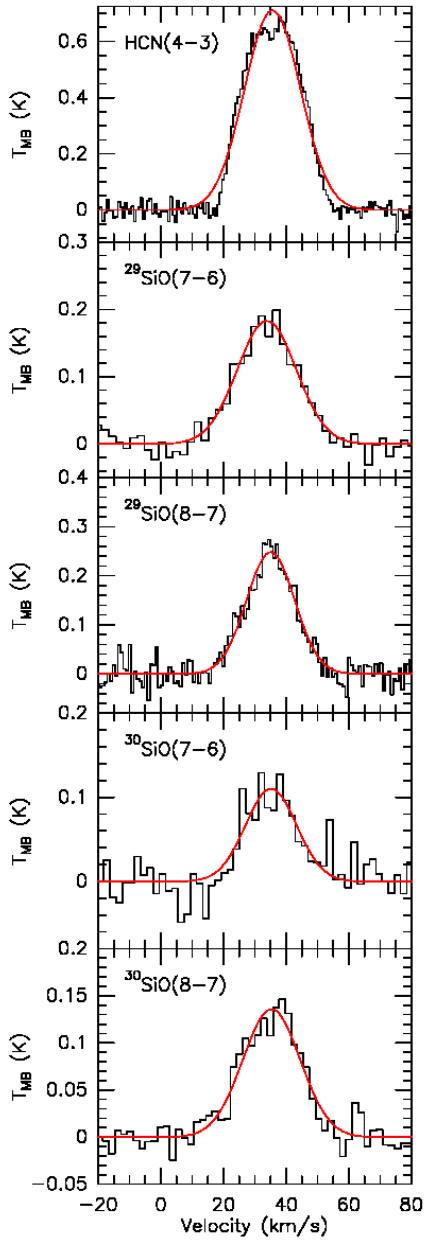

Figure 6.7.: Spectra of lines from the HCN, ^{29}SiO and ^{30}SiO molecules with Gaussian fits.

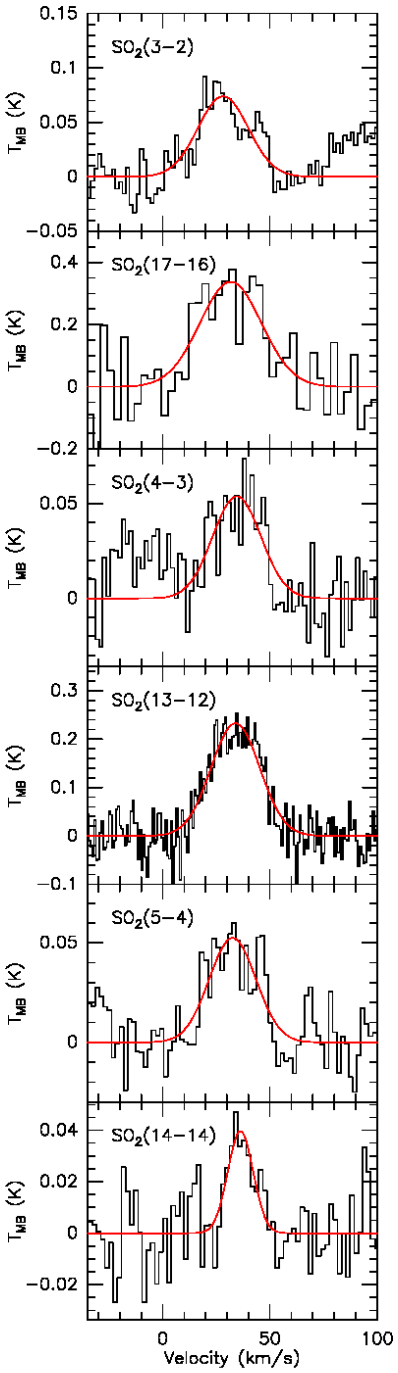

Figure 6.8.: Spectra of lines from the SO_2 molecule with Gaussian fits.

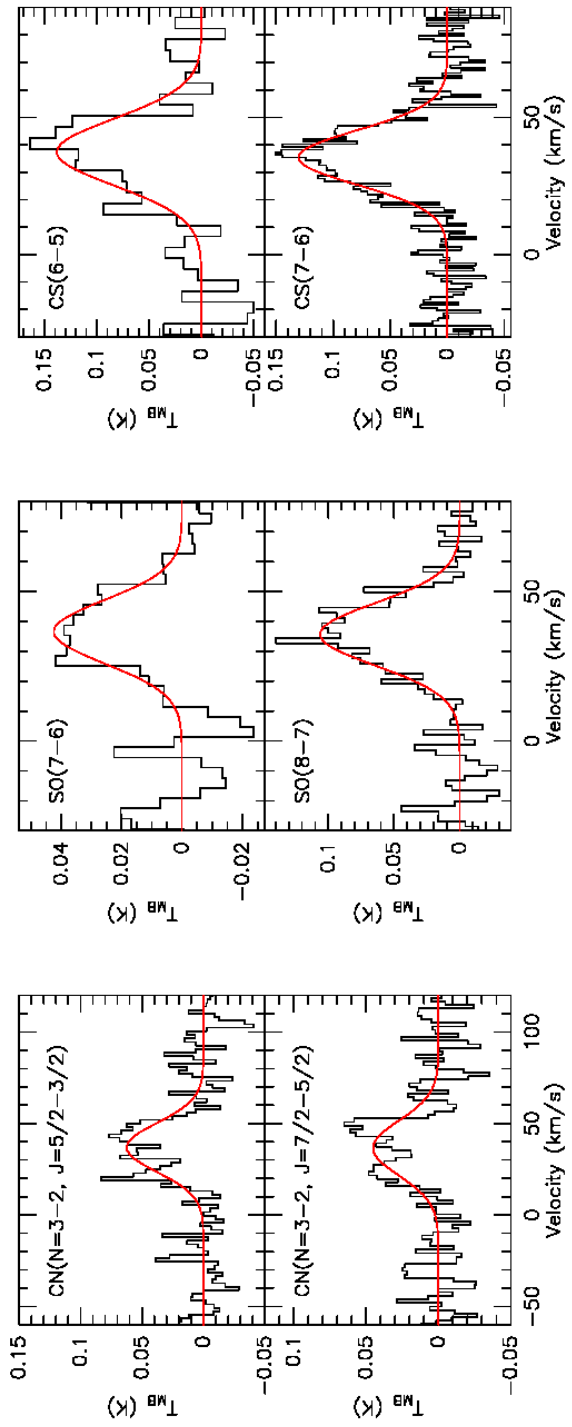

Figure 6.9.: Spectra of lines from the CN, SO and CS molecules with Gaussian fits.

6.3.1. Line Parameters of the Detected Thermal Emission Lines

To get the intrinsic brightness temperatures, the spectra were corrected by the beam-filling factors assuming a CO source size of 20″ (Bujarrabal & Alcolea 1991), a HCN source size of 3.85″ (Marvel 2005) and source sizes for the other molecules of 2.2″ (Lucas et al. 1992). The beam-filling factor is given by

$$f = \frac{\theta_S^2}{\theta_S^2 + \theta_b^2} \tag{6.2}$$

where θ_S is the source size and θ_b is the half-power beam width (HPBW). Both source and beam are assumed to be circular Gaussians. Then the intrinsic brightness temperature is computed by

$$T_b = \frac{1}{f} T_{MB} \tag{6.3}$$

where T_{MB} is the measured main beam brightness temperature.

Line parameters were derived from Gaussian and expanding shell fits with CLASS. The observed line parameters and the line parameters after correcting for the filling factor are given in table 6.3 and 6.4, including the expansion velocity V_{exp}, the main beam brightness temperature T_{MB}, the integrated area, and the parameters of the Gaussian and expanding shell fits.

6.3.2. Results

The parameters of the fits are: (i) the FWHM linewidth for Gaussian fits, (ii) an expansion velocity for expanding shell fits. The Gaussian linewidths of most of lines are distributed from 20 $\mathrm{km\,s^{-1}}$ to 35 $\mathrm{km\,s^{-1}}$ and the expansion velocities are distributed from 16 $\mathrm{km\,s^{-1}}$ to 21 $\mathrm{km\,s^{-1}}$.

When the signal-to-noise ratio is high enough to warrant a consideration of the shape of the line profiles they appear to be characteristic for circumstellar envelopes (see more detail in Zuckerman (1987)): ^{12}CO lines have the parabolic shape of optically thick lines and ^{13}CO has the double-horn shape of spatially resolved optically thin lines. SiO with its isotope lines and SiS lines have the parabolic shape of optically thick lines. Some of the SO_2 lines show the square shape characteristic of unresolved optically thin lines and some of them have the parabolic shape of optically thick lines. CN lines have the unresolved double-horn shape of optically thin lines. CS and SO lines have the square shape of unresolved optically thin lines for low excitation transitions and the parabolic shape of optically thick line for high excitation transitions. HCN shows a global parabolic shape with a weak double-peak profile on the top.

Species	Transition	Eu (K)	μ^2S (Debye^2)	Peak (K) uncorr. / corr.	Δv (km s^{-1})	Area (K km s^{-1}) uncorr. / corr.	V_{exp} (km s^{-1})
^{12}CO	3 - 2	33.2	0.04	3.31 / 5.99	26.2 (0.1)	95.7 / 173	17.7
	4 - 3	55.3	0.05	4.25 / 6.33	26.6 (0.1)	125 / 186	21.6
	7 - 6	155	0.08	5.04 / 5.85	25.2 (0.2)	129 / 149	20.9
^{13}CO	3_2 - 2_2	31.7	0.04	0.58 / 1.10	31.9 (0.5)	15.2 / 23.0	17.4
SiS	16 - 15	118	47.9	0.21 / 19.3	20.2 (1.2)	3.91 / 360	12.9
	17 - 16	133	50.9	0.28 / 23.4	20.2 (1.0)	5.77 / 483	16.4
	19 - 18	166	56.9	0.29 / 19.7	21.1 (0.3)	6.33 / 430	17.3
	20 - 19	183	59.9	0.27 / 18.3	24.7 (1.7)	5.2 / 353	19.4
SiO	7 - 6	58.4	67.4	0.87 / 72.8	20.1 (0.6)	16.4 / 1373	17.0
	8 - 7	75.0	77.0	1.27 / 86.3	20.6 (0.4)	26.7 / 1813	16.5
SO	7_7 - 6_6	71.0	16.5	0.06 / 5.0	24.7 (3.0)	1.09 / 91.2	17.7
	8_8 - 7_7	87.5	18.9	0.27 / 18.3	24.6 (1.6)	4.72 / 321	21.0
SO_2	$3_{3\,1}$ - $2_{2\,0}$	27.6	6.64	0.09 / 7.5	27.7 (2.5)	2.16 / 181	17.8
	$17_{1\,17}$ - $16_{0\,16}$	136	36.5	0.38 / 31.8	34.0 (4.0)	11.3 / 945	17.9
	$4_{3\,1}$ - $3_{2\,2}$	31.3	6.92	0.07 / 5.3	26.5 (4.2)	1.41 / 107	19.4
	$13_{2\,12}$ - $12_{1\,11}$	93.0	13.4	0.25 / 17.0	26.7 (1.2)	6.34 / 43	16.5
	$5_{3\,3}$ - $4_{2\,2}$	35.9	7.32	0.06 / 4.08	25.7 (2.4)	1.36 / 92.4	16.1
	$14_{4\,10}$ - $14_{3\,11}$	136	19.6	0.05 / 3.40	13.9 (2.8)	0.55 / 37.4	12.1

Table 6.3.: Line parameters with uncertainties. To be continued in the next table.

Species	Transition	Eu (K)	μ^2S (Debye^2)	Peak (K) uncorr. / corr.	Δv (km s^{-1})	Area (K km s^{-1}) uncorr. / corr.	v_{exp} (km s^{-1})
CS	6 - 5	49.4	23.1	0.16 / 14.7	28.6 (4.3)	4.12 / 380	19.1
	7 - 6	65.8	27.0	0.15 / 10.2	23.4 (1.1)	3.07 / 209	16.6
^{29}SiO	7 - 6	57.6	67.2	0.22 / 18.4	22.1 (0.9)	5.08 / 425	18.7
	8 - 7	74.1	76.8	0.27 / 18.3	18.5 (0.9)	4.72 / 321	15.1
^{30}SiO	7 - 6	56.9	67.2	0.13 / 12.0	19.2 (3.5)	2.06 / 190	14.1
	8 - 7	73.2	76.8	0.15 / 10.2	21.5 (1.0)	2.88 / 196	16.4
HCN	4 - 3	42.5	108	0.69 / 15.8	21.0 (3.6)	15.3 / 249	17.0
CN	N=3 - 2, J=5/2 - 3/2	32.6	6.72	0.08 / 5.44	31.5 (2.7)	1.98 / 135	18.5
	N=3 - 2, J=7/2 - 5/2	32.7	9.01	0.07 / 4.76	35.3 (3.6)	1.60 / 109	18.7

Table 6.4.: Line parameters with uncertainties.

6.4. Molecular Abundances

Individual molecular density distributions may differ substantially from the total gas density distributions due to chemical processes in the CSE. The *fractional abundance* of species A is given as

$$f_{\rm A}(r) = \frac{n_{\rm A}(r)}{n_{\rm H_2}(r)}. \tag{6.4}$$

Where $n_{\rm H_2}(r)$ is the number density of H_2 and $n_{\rm A}(r)$ is the number density of the species A.

In this section, estimates of molecular abundances and rotational temperatures are described. The rotational temperatures were obtained by the rotational diagram analysis.

6.4.1. Rotational Diagram Analysis

In order to derive the rotational temperature $T_{\rm rot}$ and the total column density $N_{\rm T}$ of the molecules, the rotational diagram analysis method (see Blake et al. 1987) was used under the assumption that (i) all lines are optically thin, (ii) local thermodynamic equilibrium (LTE) prevails and (iii) the excitation temperature between the upper and lower levels is such that $T_{\rm ex} \gg T_{\rm bg}$, where $T_{\rm bg}$ is the background temperature (in our case that of the cosmic microwave background, i.e., 2.7 K). Then the integration of the standard radiation transfer equation yields (Blake et al. 1987).

$$\frac{N_{\rm u}}{g_{\rm u}} = \frac{3kc\int T_{\rm b}dv}{8\pi^3\mu^2 S\nu^2} \tag{6.5}$$

where ν is the transition frequency, μ is the permanent dipole moment in Debye, S is the line strength, $\int T_{\rm b}dv$ is the velocity-integrated intrinsic brightness temperature and $N_{\rm u}$, $g_{\rm u}$ are the column density and degeneracy of the upper transition state, respectively. Further, $N_{\rm u}/g_{\rm u}$ may be replaced by below equation on the assumption that the population distribution is thermalized at a single rotational temperature $T_{\rm rot}$ (=$T_{\rm ex}$):

$$\frac{N_{\rm u}}{g_{\rm u}} = \frac{N_{\rm T}}{Q(T_{\rm rot})} e^{-E_{\rm u}/kT_{\rm rot}} \tag{6.6}$$

Here $N_{\rm T}$ is the total molecular column density summed over all levels, $E_{\rm u}$ is the energy of the upper transition state and $Q(T_{\rm rot})$ is the rotational partition function at temperature $T_{\rm rot}$. Then the following relation can be obtained from the equations taking the natural logarithm:

$$\ln\left(\frac{3kc\int T_{\rm b}dv}{8\pi^3\mu^2 S\nu^2}\right) = \ln\frac{N_{\rm T}}{Q(T_{\rm rot})} - \frac{E_{\rm u}}{kT_{\rm rot}} \tag{6.7}$$

Appendix C presents the rotational diagrams of the molecules observed by APEX and additionally some lines at lower frequencies (see table 6.6) from the literature. Table 6.5 presents the obtained rotation temperatures and total column densities of individual molecules.

The CO intensities in the rotational diagram cannot be fit with a single line. The reason might be that in rotational diagrams high optical depths of the lines will have the effect to reduce the calculated column densities. In the case of high optical depths the computed abundances will be only lower limits to the actual ones. Some of the variations of the abundance estimates seen in table 6.6 for a molecule might be caused by the variations in optical depths of the different transitions. This

is addressed in Appendix D.1: Take for example the trend of CO opacities with rotational quantum number J: The highest opacities are expected for the mid-J transitions. SiS on the other hand is fit well over a wide range of energies. For SiO, again the mid-J transitions seem to be suppressed, leading in this case also to an underestimate of the temperature. For a temperature twice as high, the mid-J transitions would suffer from the highest optical depths (see Appendix D.6) which would explain the distribution of the lines in the rotational diagram.

Species	Trot (K)	N (cm^{-2})
^{12}CO	47.0 (3.7)	$1.32x10^{17}$ ($2x10^{16}$)
^{13}CO	21.4 (4.9)	$1.27x10^{16}$ ($4x10^{15}$)
SiS	85.8 (11.1)	$4.46x10^{15}$ ($1x10^{15}$)
SiO	17.1 (1.0)	$8.24x10^{15}$ ($1x10^{15}$)
SO	27.2 (2.7)	$6.35x10^{15}$ ($2x10^{15}$)
SO_2	67.5 (6.8)	$2.02x10^{16}$ ($4x10^{15}$)
^{30}SiO	68.8 (82.3)	$2.48x10^{14}$ ($4x10^{14}$)
^{29}SiO	30.0 (15.5)	$7.12x10^{14}$ ($9x10^{14}$)
CS	33.9 (4.7)	$8.89x10^{14}$ ($2x10^{14}$)
HCN	8.3 (0.5)	$2.27x10^{15}$ ($5x10^{14}$)

Table 6.5.: Rotational temperature and column density with uncertainties (no systematic errors included).

6.4.2. Molecular Abundance Calculation

In order to calculate molecular abundances, it was assumed that all of the observed molecular transitions are optically thin and the envelope is spherically symmetric. I followed the same method for the calculation of molecular abundances as used in Olofsson et al. (1991). For an optically thin rotational line ($J \rightarrow J-1$) of a linear rotor the abundance with respect to H_2 is given by

$$f_{\rm CO} = 3.8 \times 10^{-16} T_{\rm a} \frac{v_{\rm exp}^2 BD}{\dot{M}} \frac{T_{\rm ex}}{\mu_0^2 B_0^2 J^2} exp(\frac{h(B_0 \times 10^9) J(J+1)}{kT_{\rm ex}}) \frac{1}{\int_{x_i}^{x_e} exp(-4\ln 2x^2) dx} \qquad (6.8)$$

where $T_{\rm a}$ (= $T_{\rm MB}$) is the antenna brightness temperature, $T_{\rm ex}$ is the excitation temperature (= $T_{\rm rot}$), μ_0 is the dipole moment in Debye, B_0 is the rotational constant in GHz, $v_{\rm exp}$ is the gas expansion velocity of the CSE in $\mathrm{km\,s^{-1}}$, B is the beam size in arcseconds, D is the distance to the source in pc, $\dot{M}$ is the mass-loss rate in $\mathrm{M_\odot\,yr^{-1}}$, and x_i (= $0.5R_0/B$ in arcseconds), x_e (= $2R_0/B$ in arcseconds) are the inner and outer radius of the CSE. The photospheric radius is given by Habing & Olofsson (2003)

$$R_{\rm ph,CO} = 10^{16}(0.8[\frac{v_{\rm exp}}{15}] + 6[\frac{\dot{M}}{10^{-6}}]^{0.7}[\frac{15}{v_{\rm exp}}]^{0.6}[\frac{f_{\rm CO}}{10^{-3}}]^{0.6}) \qquad \mathrm{cm} \qquad (6.9)$$

A mass loss rate of $\dot{M} = 4.7 \times 10^{-6}$ $M_{\odot}\,yr^{-1}$ (Teyssier et al. 2006) and a radius of $R_0 = 10^{17}$ cm for the molecular emitting region were adopted to calculate the abundance of ^{12}CO and ^{13}CO. For the other molecules, values for the outer radii were adopted of 2×10^{15} cm for SiO (Bujarrabal et al. 1994) and 1×10^{16} cm for the other molecules because some of the molecules exist further out than SiO. The expansion velocity is 18 $km\,s^{-1}$ determined by the expansion shell fitting of the $^{12}CO(3-2)$ line. The excitation temperatures, T_{ex}, were determined by the rotational diagram method.

The abundances of the other molecules (except SO_2) with respect to CO abundance (3×10^{-4}, Knapp & Morris (1985)) were estimated by the equation given by Lindqvist et al. (1988):

$$f_x(x) = 8.7 \frac{T_a(x) f(CO)^{0.85}}{T_a(CO)} \frac{B}{D} \frac{T_{ex}(x)}{\mu_0^2 B_0^2 J^2} exp\left(\frac{h(B_0 \times 10^9) J(J+1)}{k T_{ex}(x)}\right) \frac{1}{\int_{x_i}^{x_e} exp(-4 \ln 2 x^2) dx} \tag{6.10}$$

The SO_2 abundances with respect to H_2 were estimated by the equation given by Morris et al. (1987):

$$f_{SO_2} = \frac{T_a(SO_2)}{2 \times 10^{13}} \frac{v_{exp}^2 BDQ(T_{ex})}{\dot{M} \mu_0^2 S \nu} \frac{1}{exp[-1.44 E_u / T_{ex}]} \frac{1}{\int_{x_i}^{x_e} exp(-4 \ln 2 x^2) dx} \tag{6.11}$$

where $Q(T_{ex})$ is the molecular partition function ($\simeq 1.15 T_{ex}^{3/2}$, see more detail in Omont et al. (1993)), E_u is the energy of the upper state of the transition, S is the line strength, and ν is the frequency of the transition.

The obtained abundances of the molecular transitions are given in table 6.6.

6.4.3. Results

We estimated the rotational temperatures and the column densities of the detected molecules using the rotational diagram analysis assuming that the lines are optically thin and the circumstellar envelope is in LTE ($T_{ex} = T_{rot}$).

The fractional abundance of CO, whose lines all have very high optical depth, relative to H_2 was determined using a Monte Carlo non-LTE method as described in § 6.7.

By using the derived rotation temperatures the fractional abundances for the other species with respect to CO were obtained.

The most uncertain parameters used to derive the fractional abundances were T_{ex}, D and x_e (the outer radius). T_{ex} was obtained from the rotational diagram analysis, D was from the literature, and the outer radius of x_e has been adopted differently for individual molecules. The absolute abundances depend on the uncertain mass-loss rate, but the relative abundances between molecules should be accurate, except for optically thick lines (Morris et al. 1987). Many of the observed molecules show optically thick profiles and individual transitions have different opacities. Therefore, the abundances were estimated for each transition for some molecules (see section 6.4.2). The line opacity may be expected to be larger for higher J rotational transitions so that lower J rotational transitions are expected to be better probes of the abundance. In general, an optical depth $\gtrsim 1$ will lead to an underestimate of the molecular abundance.

Table 6.7(a) lists the averaged abundances of molecules from this research and the literature, and Table 6.7(b) lists the abundance from chemical models calculated by Duari et al. (1999). Compared

Speccies		Abundance	Photosphere radius	Reference
^{12}CO	(1-0)	$5.6x10^{-4}$	$1.2x10^{17}$	1)
	(2-1)	$1.3x10^{-4}$	$5.6x10^{16}$	1)
	(3-2)	$1.2x10^{-4}$	$5.3x10^{16}$	
	(4-3)	$1.0x10^{-4}$	$5.1x10^{16}$	
	(7-6)	$1.5x10^{-4}$	$6.1x10^{16}$	
^{13}CO	(1-0)	$2.2x10^{-5}$	$2.6x10^{16}$	1)
	(2-1)	$8.8x10^{-6}$	$1.9x10^{16}$	1)
	(3-2)	$2.3x10^{-5}$	$2.6x10^{16}$	
CS	(2-1)	$1.8x10^{-7}$		2)
	(3-2)	$8.7x10^{-8}$		3)
	(6-5)	$1.3x10^{-7}$		
	(7-6)	$1.1x10^{-7}$		
SO	$(2_2 - 1_1)$	$1.3x10^{-7}$		4)
	$(5_6 - 4_5)$	$7.6x10^{-7}$		3)
	$(7_7 - 6_6)$	$1.5x10^{-7}$		
	$(8_8 - 7_7)$	$8.0x10^{-7}$		
SO_2	$(3_{13} - 2_{02})$	$3.4x10^{-6}$		4)
	$(10_{19} - 10_{010})$	$2.3x10^{-6}$		4)
	$(10_{010} - 9_{19})$	$3.6x10^{-6}$		4)
	$(3_{31} - 2_{20})$	$1.3x10^{-6}$		
	$(17_{117} - 16_{016})$	$1.0x10^{-5}$		
	$(4_{31} - 3_{22})$	$9.1x10^{-7}$		
	$(13_{212} - 12_{111})$	$5.5x10^{-6}$		
	$(5_{33} - 4_{22})$	$7.1x10^{-7}$		
	$(14_{410} - 14_{311})$	$1.9x10^{-6}$		
SiS	(5-4)	$6.3x10^{-7}$		3)
	(16-15)	$5.1x10^{-7}$		
	(17-16)	$7.0x10^{-7}$		
	(19-18)	$6.2x10^{-7}$		
	(20-19)	$7.0x10^{-7}$		
SiO	(2-1)	$6.2x10^{-6}$		3)
	(3-2)	$5.8x10^{-6}$		3)
	(5-4)	$1.5x10^{-6}$		4)
	(7-6)	$3.5x10^{-6}$		
	(8-7)	$8.4x10^{-6}$		
^{29}SiO	(7-6)	$2.1x10^{-6}$		
	(8-7)	$6.1x10^{-6}$		
^{30}SiO	(7-6)	$1.3x10^{-6}$		
	(8-7)	$3.1x10^{-6}$		
HCN	(1-0)	$2.0x10^{-7}$		3)
	(4-3)	$1.2x10^{-6}$		

Table 6.6.: Molecular abundances and photosphere radius with individual transitions. The references for data taken from the literature are 1) : Bujarrabal & Alcolea (1991), 2) : Lindqvist et al. (1988), 3) : Bujarrabal et al. (1994) and 4) : Omont et al. (1993).

to the literature (Bujarrabal et al. (1994), Lindqvist et al. (1988) and Omont et al. (1993)), the abundance of CO of this research is 1.4 $\sim$ 1.7 times less than the published results, the CS abundance is 1.3 times higher than Bujarrabal et al. (1994) result and 2.3 times less than Lindqvist et al. (1988) result, the HCN abundance is 1.4 times less than Bujarrabal et al. (1994) result and 1.2 times higher than Lindqvist et al. (1988) result, the SiO abundance is 3.3 times less than Bujarrabal et al. (1994) result and 1.7 times higher than Omont et al. (1993) result, the SiS abundance is 1.4 times higher than Bujarrabal et al. (1994) result and 1.1 times less than Lindqvist et al. (1988) result, the SO abundance is 5.7 times less than Bujarrabal et al. (1994) result and 4 times less than Omont et al. (1993) result, the SO_2 abundance is 1.2 times less than Omont et al. (1993).

Compared to the calculated abundances, the ^{12}CO abundance is 2.6 times less than the calculated result (Duari et al. 1999) at 2.2 R_*, the CS abundance is 2.2 times less than the literature value at 2.2 R_*, that of HCN is 3 times less than the literature value at 2.2 R_*, that of SiO is approximately 8 times less at all radii, that of SiS is 5.4 times less at 1 R_*, and that of SO is roughly 5.5 times higher at 2 R_*.

In summary, since more transitions have been included in the current study, one expects our results to be an improvement over the previously available observed abundances.

	^{12}CO	^{13}CO	CS	HCN	SiO	SiS	SO	SO_2
This work	$2.1x10^{-4}$	$1.8x10^{-5}$	$1.3x10^{-7}$	$7.0x10^{-7}$	$5.1x10^{-6}$	$6.3x10^{-7}$	$4.6x10^{-7}$	$3.3x10^{-6}$
Bujarrabal (1993)	$3.0x10^{-4}$	$3.2x10^{-5}$	$1.0x10^{-7}$	$9.8x10^{-7}$	$1.7x10^{-5}$	$4.4x10^{-7}$	$2.6x10^{-6}$	-
Lindqvist (1988)	$3.0x10^{-4}$	-	$3.0x10^{-7}$	$6.0x10^{-7}$	-	$7.0x10^{-7}$	-	-
Omont (1993)	-	-	-	-	$3.0x10^{-6}$	-	$1.8x10^{-6}$	$4.1x10^{-6}$

(a)

Duari (1999)	^{12}CO	^{13}CO	CS	HCN	SiO	SiS	SO	SO_2
LTE	$7.0x10^{-4}$	-	$1.3x10^{-10}$	$4.4x10^{-11}$	$4.3x10^{-5}$	$2.9x10^{-7}$	$2.2x10^{-8}$	-
$1R_* / 32$ km s^{-1}	$5.5x10^{-4}$	-	$8.1x10^{-6}$	$1.6x10^{-4}$	$4.1x10^{-5}$	$3.4x10^{-6}$	$4.9x10^{-9}$	-
$1.5R_* / 26.1$ km s^{-1}	$6.4x10^{-4}$	-	$1.1x10^{-5}$	$6.5x10^{-5}$	$4.4x10^{-5}$	$1.6x10^{-7}$	$3.1x10^{-8}$	-
$2R_* / 22.6$ km s^{-1}	$6.1x10^{-4}$	-	$5.2x10^{-7}$	$5.2x10^{-6}$	$4.1x10^{-5}$	$1.4x10^{-9}$	$8.3x10^{-8}$	-
$2.2R_* / 21.6$ km s^{-1}	$5.4x10^{-4}$	-	$2.8x10^{-7}$	$2.1x10^{-6}$	$3.8x10^{-5}$	$3.8x10^{-10}$	$7.8x10^{-8}$	-

(b)

Table 6.7.: Comparison of the molecular abundances: (a) between this observation results and the literature results, (b) calculated abundances versus shock strength and radius by Duari et al. (1999), R_* is $305R_\odot$.

6.5. Spatial Distribution of ^{12}CO

To map the circumstellar envelope, 30 positions distributed on a 5×6 grid parallel to the 2 coordinate axes were observed. The grid spacing was $9''$ (half the FWHM beamsize at 345 GHz). A raster mapping procedure was used along the parallel grid lines with an integration time of 15 s. Pointing observations were made by observing cross scans on IK Tau itself. The spectra of the $^{12}\mathrm{CO}(3-2)$ transition were taken for a region of $45\times54''$ and are plotted in figure 6.10.

The source size as a function of radial velocity was derived as shown in figure 6.11. The envelope of IK Tau appears roughly spherical in $^{12}\mathrm{CO}(3-2)$ with a deconvolved extent at half maximum of approximately $20''$. The radius of the emission region is then 4×10^{16} cm assuming a source distance of 250 pc. The FWHM has been also been computed by fitting a Gaussian source model to the integrated antenna temperature distribution. The FWHM was approximately $20''$. This value is similar to the one found in Bujarrabal & Alcolea (1991).

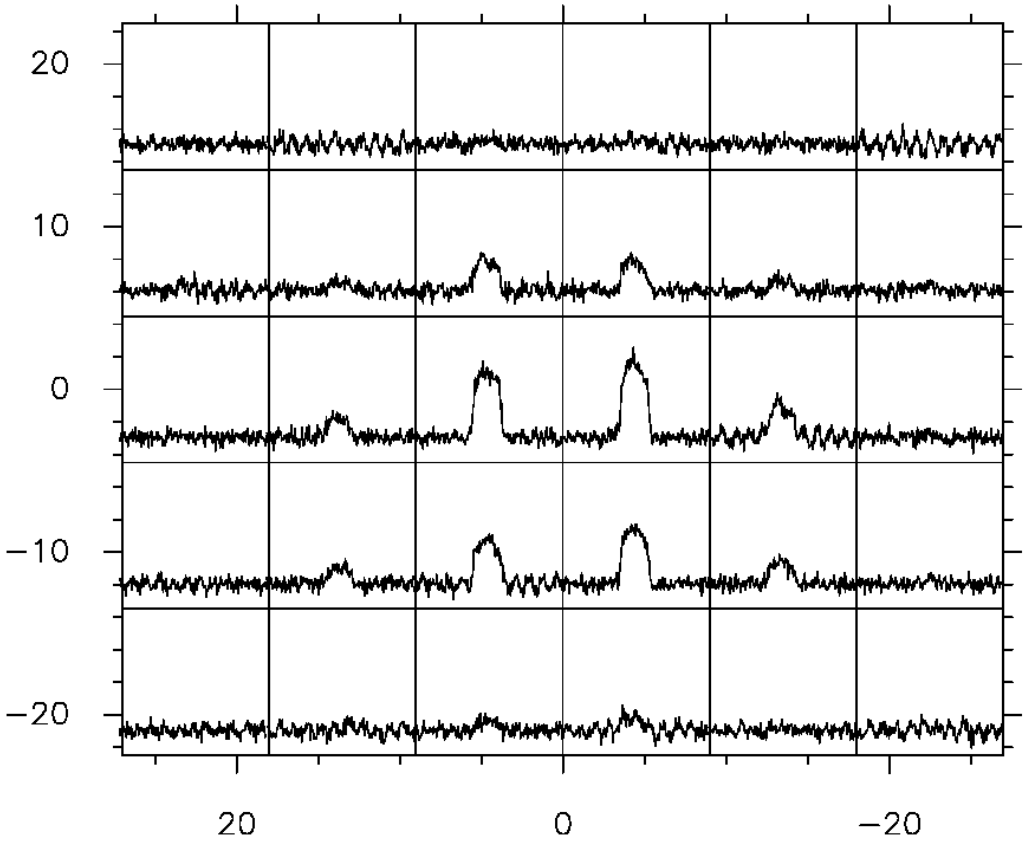

Figure 6.10.: Map of ^{12}CO J=3-2 line emission toward IK Tau. The grid spacing was $9''$. The main-brightness temperatures in the spectra range from 0.5 K to 3.3 K.

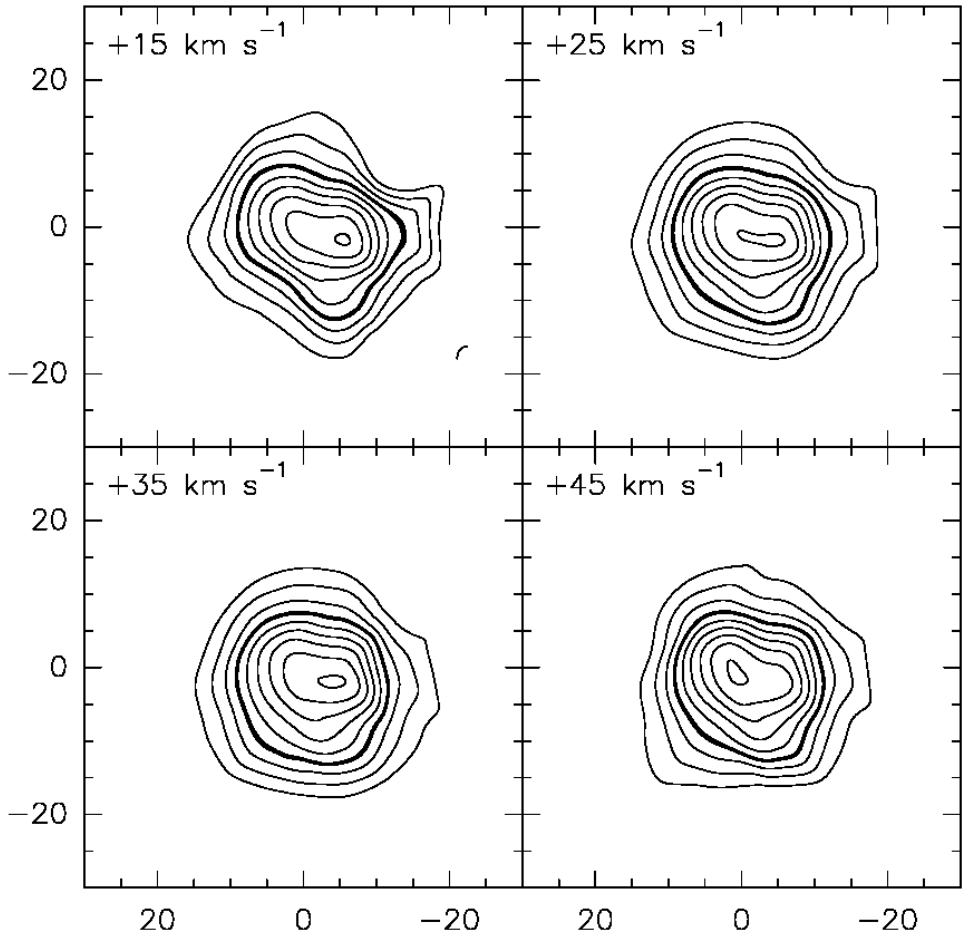

Figure 6.11.: Contour maps of the ^{12}CO J=3-2 line emission for IK Tau integrated over 10 km s^{-1} centered at velocities of 15 km s^{-1}, 25 km s^{-1}, 35 km s^{-1} and 45 km s^{-1}, respectively. One velocity interval is centered near the stellar radial velocity (33.7 km s^{-1}).The contour values are 20 % to 90 % and 99 % of the maximum integrated intensity in each velocity interval, which is 7, 29, 32, and 26 K km s^{-1} for the 15, 25, 35, and 45 km s^{-1} channel, respectively. The 50 % contour is drawn in boldface.

6.6. Maser Emission

The association of OH, H_2O and SiO maser emission with oxygen-rich red giants and supergiants provides a useful probe of the spatial structure and kinematics of their circumstellar envelopes and of the mass loss process in these stars (Lane et al. 1987). The spectral line profiles of masers contain important information on the conditions of the masing region (masing regions exist in IK Tau due to their large mass-loss rates and the physical conditions in the circumstellar shells), such as the thermal line width of the particle distribution and optical depth (Vlemmings & van Langevelde

2005). Menten & Young (1995) suggested that H_2O and SiO masers coexist probably in the hot and dense regions within the central few stellar radii and are located in the same parts of circumstellar envelopes.

6.6.1. H_2O Maser Lines

H_2O is one of the most abundant molecules in the envelopes of cool oxygen rich evolved stars (Menten 1996) but visually not observable from the ground. The exception are strong maser lines emitted from high-lying energy levels that are poorly populated at the temperature of the Earth′s atmosphere. H_2O masers are located in the inner parts of circumstellar shells at distances of $10^{14} \sim 10^{15}$ cm from the central star (7–70 AU $\approx$ 10-20 R_c), where the temperatures are between an 300 K and 1000 K, the number densities of H_2 are $10^7 - 10^9$ cm^{-3} and $N(H_2O)/N(H_2)$ is assumed to be about 10^{-4} (Benson & Little-Marenin 1996).

Figure 6.12 shows the 321 GHz and 325 GHz H_2O maser lines observed toward IK Tau. The 321 GHz spectrum shows a single peak near the stellar velocity $V_* = 33.7$ km s^{-1}. The 325 GHz spectrum shows a broad emission profile shifted to the red with respect to the stellar velocity (see table 6.8).

As shown in the figure (see also table 6.6), the velocity of 321 GHz emission is smaller than that of 325 GHz. This is also observed toward other stars. As a reason for this, Yates et al. (1995) suggested that the emission region and maser pumping mechanism of these two maser lines are different. This is understandable since the lower energy level of the 325 GHz line lies only 470 K above the ground state while that of the 321 GHz line is 1861 K above ground. It means that the 321 GHz maser is excited nearer to the central star.

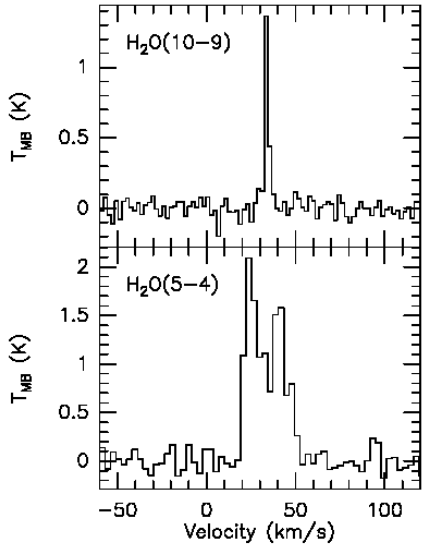

Figure 6.12.: The 321 GHz and 325 GHz H_2O maser emission lines observed toward IK Tau.

6.6.2. SiO Maser Lines

Masers from vibrationally states of the SiO molecule arise from the innermost layers of the circumstellar envelopes between 2 and 4 R_c (Diamond et al. 1994). SiO masers need high temperatures (> 1000 K) and densities ($> 10^9$ cm^{-3}) for their excitation (the $v = 1$ state of SiO is 1770 K above ground, Alcolea (2004)). SiO masers were detected in the three main isotopic substitutions of SiO, ^{28}SiO, ^{29}SiO and ^{30}SiO, in the rotational transitions $J = 7-6$ and $J = 8-7$ of the fundamental v=1 and v=3 vibrationally excited states (see table 6.8, see also figure 6.13). The masers were identified from a list of SiO transition calculated by K. Menten from molecular constants presented by Mollaaghababa et al. (1991).

The figure shows the detected SiO maser lines toward IK Tau. The ^{28}SiO (v=1, 7-6) spectrum shows a broad emission profile shifted to the blue with respect to the stellar velocity, (8-7) spectrum shows a single peak shifted to the red and (v=3, 7-6) shows a single peak near the central velocity. ^{29}SiO (v=1, 7-6) shows a double peaks shifted to the blue. ^{30}SiO (v=1, 8-7) shows an unresolved double peak near the stellar velocity (see table 6.4).

Species	Transition	uncorr. / corr.	uncorr. / corr.	Velocity (km s^{-1})
H_2O	10_{29} - 9_{36}	1.36 / 103	4.31 / 326	33.4
	5_{15} - 4_{22}	2.09 / 158	37.9 / 2864	35.0
^{28}SiO	V=1, 7 - 6	0.44 / 36.8	3.64 / 305	32.5
	V=1, 8 - 7	0.29 / 19.7	1.00 / 67.9	34.6
	V=3, 7 - 6	0.36 / 30.1	1.22 / 102	33.4
^{29}SiO	V=1, 7 - 6	0.41 / 34.3	1.63 / 136	32.9
^{30}SiO	V=1, 8 - 7	1.40 / 106	5.40 / 408	33.8

Table 6.8.: Line parameters of the detected masers.

6.6.3. Results

Maser emission of H_2O at 321 GHz and 325 GHz, and ^{28}SiO, ^{29}SiO and ^{30}SiO in the rotation transitions 7-6, 8-7 of the v=1 and v=3 vibrational excited states was detected. A discussion of their excitation is beyond the scope of this work. Future subarcsecond resolution observations of these lines with the Atacama Large Millimeter Array will allow studies of the innermost envelopes of O-rich AGB stars.

6.7. Molecular Emission Model

CO lines are amongst the best tools to estimate the global properties of circumstellar envelopes, since the abundance of CO is quite constant across the envelope, except for photodissociation effects at the outer edge (Teyssier et al. 2006). Moreover, the spatial distribution of CO was found from our

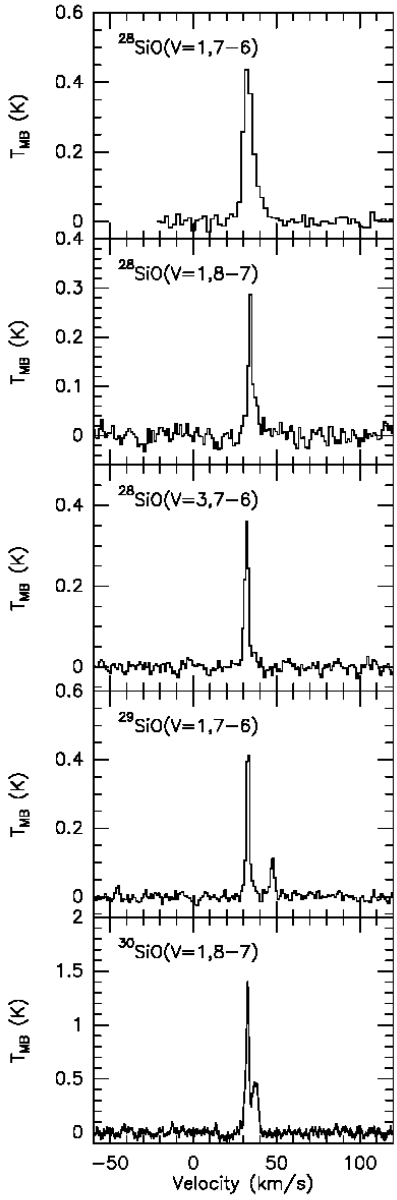

Figure 6.13.: ^{28}SiO, ^{29}SiO and ^{30}SiO maser emission lines in rotational transition $J = 7-6$ and $J = 8-7$ of the fundamental v=1 and v=3 vibrational excited states observed toward IK Tau.

mapping observation to have a spherical shape (see section 6.5). A detailed multiline non-LTE study of CO can therefore be used to determine the physical properties of the envelope. It can also account for opacity effects, which are evident from the line profiles and the non-linearity in the rotational diagram. In this section, we used the one-dimensional version of the Monte Carlo code developed by Hogerheijde & van der Tak (2000), to simulate the CO emissions and SO_2 emissions. The basic idea of the Monte Carlo method is to split the emergent radiative energies into *photon packages*, which perform a random walk through the model volume. This allows the separation of local and external contributions of the radiation field. This makes it possible to calculate the radiative transfer and excitation of molecular lines.

The Monte Carlo method for molecular line transfer has been described by Bernes (1979) for a spherically symmetric cloud with a uniform density. The code is formulated from the viewpoint of cells rather than photons. It shows accurate and fast performance even for high opacities (for more details see Hogerheijde & van der Tak (2000)). For the analysis, the circumstellar envelopes are assumed to be spherically symmetric, to be produced by a constant mass-loss rate, and to expand at a constant velocity.

6.7.1. CO Emission

For the case of a steady state, spherically symmetric outflow, the gas density as a function of radial distance from the center of the AGB star is

$$n(r) = \frac{\dot{M}}{4\pi r^2 v_{\exp} m} \tag{6.12}$$

where m is the mass of the typical gas particle, assumed to be $m \sim 3 \times 10^{-24}$ gram, since the gas is mainly molecular in AGB envelopes (Teyssier et al. 2006). In the Monte Carlo simulation, typically 10^3 model photons are followed throughout the envelope until they escape. The region is divided into spherical shells with an inner radius and an outer radius. The CO abundance and expansion velocity were considered constant within each shell. The initial input parameters were based on the modeling by Teyssier et al. (2006). The kinetic temperature was assumed to vary as

$$T = T_0 [\frac{10^{16}}{r(\mathrm{cm})}]^{\alpha} + T_{\mathrm{bg}}. \tag{6.13}$$

T_0 is the temperature at $\sim 10^{16}$ cm. The best fit model parameters are presented in table 6.9. With the radial profiles for density and temperature given by equations 6.12 and 6.13 the program solved for the molecular excitation as a function of radius. Beside collisional excitation, radiation from the cosmic microwave background and thermal radiation from local dust were taken into account. The result was integrated in radial direction over the line of sight and convolved with the appropriate antenna beam (van der Tak et al. 2003).

6.7.2. SO_2 Emission

In order to model the circumstellar SO_2 line emission the non-LTE radiative transfer code was used as well. SO_2 exists probably in the inner part of envelopes since the excitation temperature estimates range from 50 K to 80 K. SO_2 lines are optically thin given to the opacities obtained (see Appendix D.10). However, in the rotational diagram (see Appendix C.6), the line intensities do not depend

	R_i (10^{14} cm)	R_{co} (10^{14} cm)	Mass-loss rate ($M_\odot yr^{-1}$)	f_{CO} (10^{-4})	V_{exp} (km s^{-1})	T_0 (K)	α	T_{bg} (K)
^{12}CO	1	630	4.7×10^{-6}	3	18	40	0.8	2.7
^{13}CO	1	700	4.7×10^{-6}	0.3	18	50	0.8	2.7

Table 6.9.: Input parameters for the CO emission model.

linearly on the energies of the levels, which is an indication of non-LTE excitation. Therefore, SO_2 was also modeled with the non-LTE code. The adopted input parameters are presented in table 6.10. The main differences to the CO result is a smaller outer radius and an abundance of 5×10^{-6}.

	R_i (10^{14} cm)	R_{SO2} (10^{14} cm)	Mass-loss rate ($M_\odot yr^{-1}$)	f_{SO2} (10^{-4})	V_{exp} (km s^{-1})	T_0 (K)	α	T_{bg} (K)
SO_2	1	70	4.7×10^{-6}	0.05	18	50	0.8	2.7

Table 6.10.: Input parameters for the SO_2 emission model.

6.7.3. Results

1. CO Emission

An extensive radiative transfer analysis of circumstellar CO was performed, using the Teyssier et al. (2006) parameters as starting values. The results of the model fits are shown in figure 6.14. In figure 6.15 the models for ^{12}CO with different inner radii, different T_0, and different outer radii are shown. Fits to offset positions are shown in figure 6.16, and models for ^{13}CO with different T_0 are presented in figure 6.17.

As shown in figure 6.14, the overall line profiles were fit very well for the higher J transitions ($^{12}CO(3-2)$, $^{12}CO(4-3)$, $^{12}CO(7-6)$) observed in the course of this work. However, the model intensities of the lower transitions ($^{12}CO(1-0)$ and $^{12}CO(2-1)$) from the literature are somewhat higher than the observational results but the shapes were fit very well. For this reason, the column density is probably too high for the lower transitions. The mass-loss rate and the CO abundance affect the radiative transfer because the number of CO molecules depends on the total density, which is proportional to the mass-loss rate. If the lines are optically thin then the intensity scales with the CO column density (Crosas & Menten 1997). The $^{13}CO(3-2)$ line also clearly shows a double-horn profile and the best fit results in a somewhat different T_0 and a different outer radius, although the best fit for T_0 from ^{12}CO gives still a reasonable fit to the ^{13}CO line (figure 6.17). As shown in the figure, the intensities of the profiles do not change so much with T_0 but the lines show a flat shape on the top at low temperatures of 30 K and 40 K, and a double-horn shape at higher temperatures.

As shown in figure 6.15, the line shapes and intensities in all transitions were not influenced by the inner radius variations because the ^{12}CO emission contributing dominantly to the spectra arises from regions further out in the envelope. Outer radius variations, did not change significantly the shapes

of higher excitation lines. From this result, we can expect that the $^{12}CO(1-0)$ emission arises from parts of the envelope that are further out than the region from which higher transitions arises an one would expect. To test the prediction of the model on the size of the CO distribution, model spectra were computed with 13 positions distributed on a 7×7 cross grid ($63\times63''$ region). The determined envelope size at half maximum is approximately $20''$. By comparing the spatial distribution of the observational result (see figure 6.11) and the modeling result (see figure 6.16), the radius of half maximum is approximately identical with $20''$, comparable to the observed size.

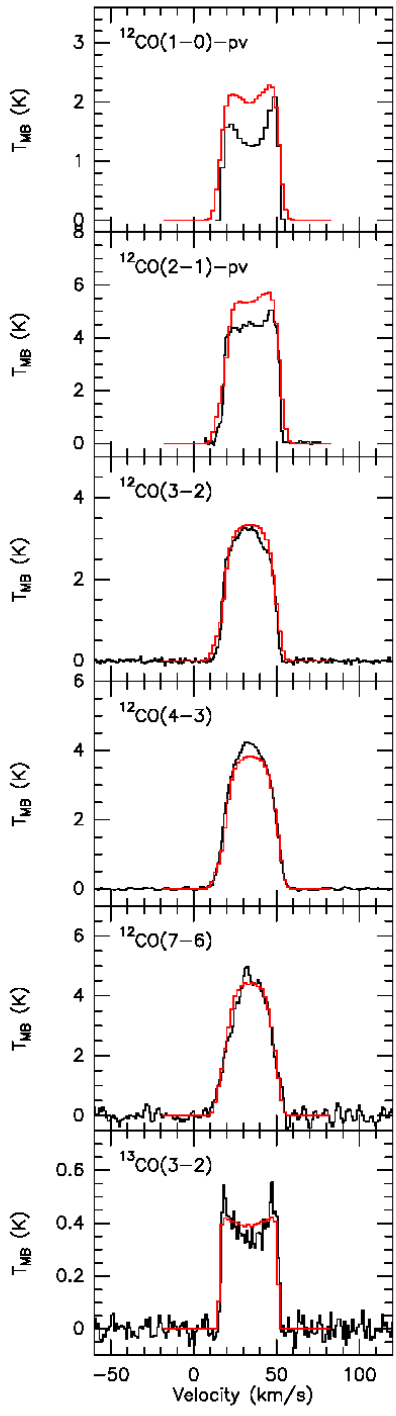

Figure 6.14.: Best model fits of the CO transitions to the available set of data at offset (0″,0″) for IK Tau. For each of the panels, we show the CO transitions and the telescope used to obtain the spectrum displayed. All temperatures are in T_{mb}. $^{12}CO(1-0)$ and $^{12}CO(2-1)$ are from Teyssier et al. (2006). ′pv′ means the IRAM 30 m telescope in Pico Veleta.

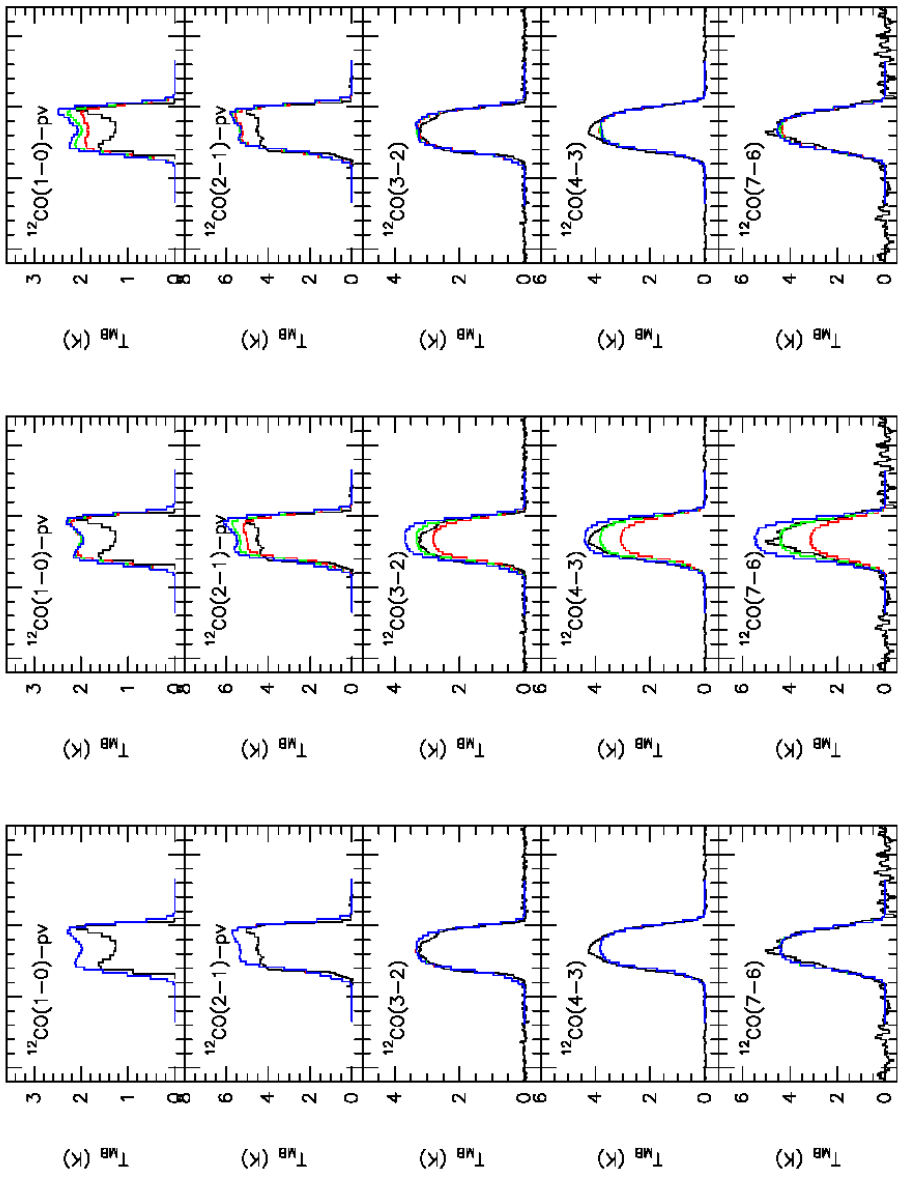

Figure 6.15.: Model fits with different input parameters to the set of data at offset (0″, 0″) for IK Tau. (a) inner radius variation: (red line) 0.1×10^{14} cm, (green line) 1×10^{14} cm, (blue line) 10×10^{14} cm. (b) T_0 variation: (red line) 30, (green line) 40, (blue line) 50. (c) outer radius variation: (red line) 5.3×10^{16} cm, (green line) 6.3×10^{16} cm, (blue line) 7.3×10^{16} cm.

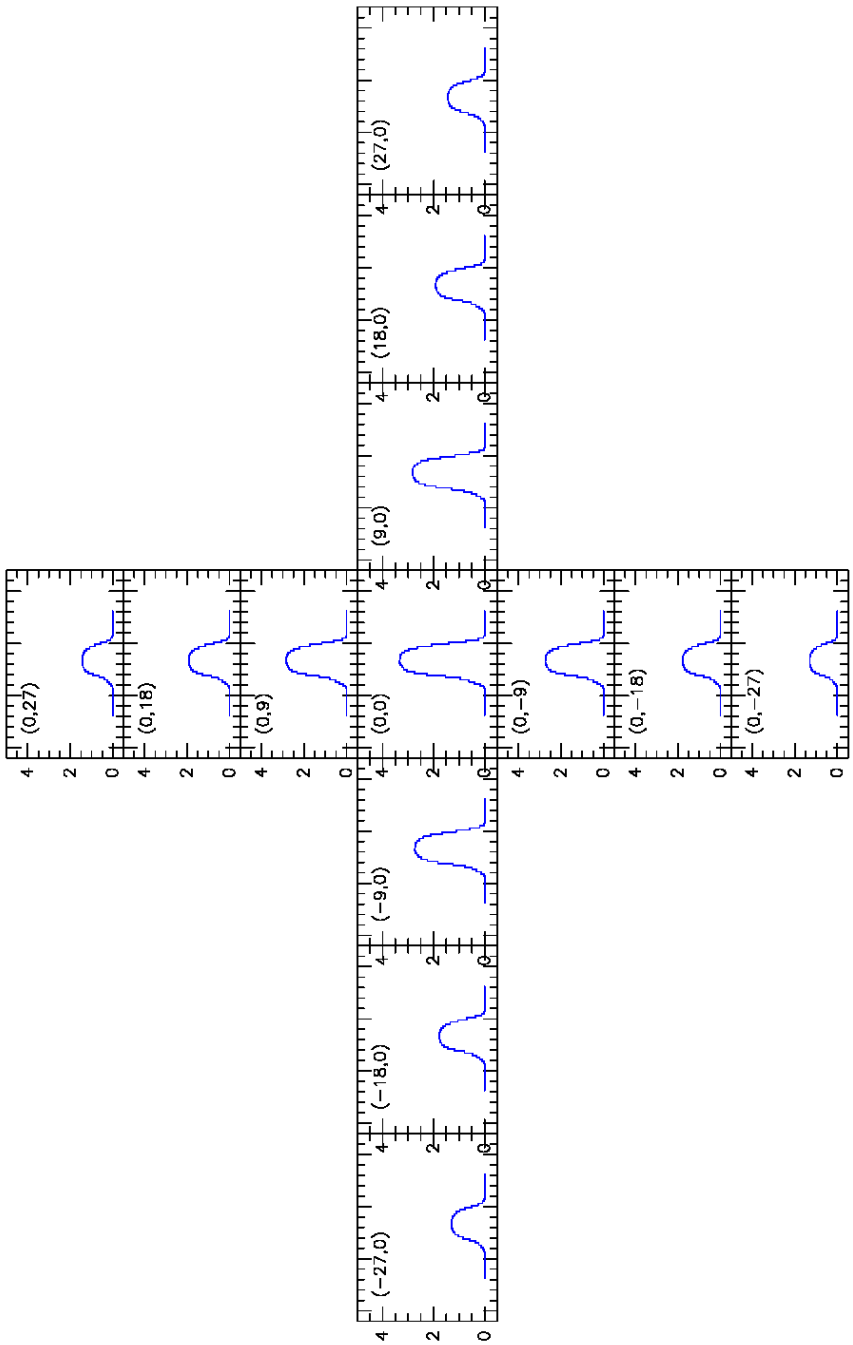

Figure 6.16.: Model fits to offset positions of the ^{12}CO$(3-2)$ transition. The numbers in the upper left corner of each box indicates the offset from the (0,0) position.

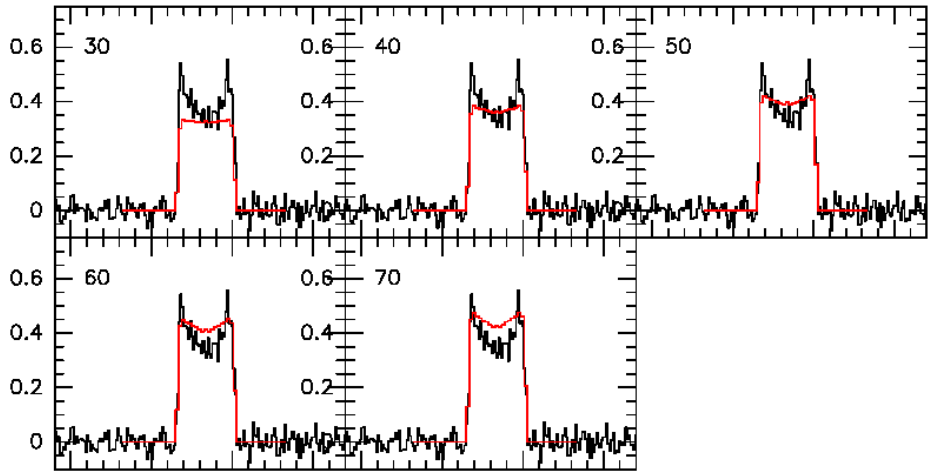

Figure 6.17.: Model fits of the ^{13}CO transition with different T_0. The numbers in the upper left corner of each box indicates T_0 in K.

2. SO_2 Emission

An extensive radiative transfer analysis of circumstellar SO_2 was also performed. The modeled emission lines are presented in figure 6.18. As shown in the figure, the model fits reasonably well the $SO_2(3-2)$, $SO_2(4-3)$, and $SO_2(5-4)$ lines. However, the model did not fit the high excitation $SO_2(17-16)$, $SO_2(13-12)$, and $SO_2(14-14)$ lines. As shown in the Appendix, the predicted T_{MB} values for the SO_2 transitions depend on the kinetic temperature (see Appendix D.12) and also on the column densities (see Appendix D.11). Introducing a much hotter component of SO_2 will still not reproduce the observed intensities of the high excitation lines. In a study of SO_2 in star forming regions van der Tak et al. (2003) had this problem as well. They solved the problem by increasing the SO_2 abundance arbitrarily by a factor 100 in the inner hotter regions probably caused by ice evaporation of solid SO_2. Since in the model for IK Tau the SO_2 abundance is already quite high, introducing a jump of a factor 100 would lead to unreasonable high SO_2 abundances. A possible cause of the discrepancies between model fits and observed line intensities toward IK Tau and the star forming regions could be the treatment of the collisional rates for highly excited SO_2 states: In the models, the rates were taken from Schöier et al. (2005). Green (1995) only computed the rates for lower excitation levels and the rates for the high excitation levels were extrapolated by Schöier et al. (2005). Those extrapolations could be wrong. Finally, one cannot exclude misidentification of the observed line features, although they are very close to the frequencies expected in IK Tau (see Figure 6.18). An important test for the different explanations of the SO_2 results will be to repeat the observations of the high excitation lines and also to extend those observations to other high excitation lines not observed in this study.

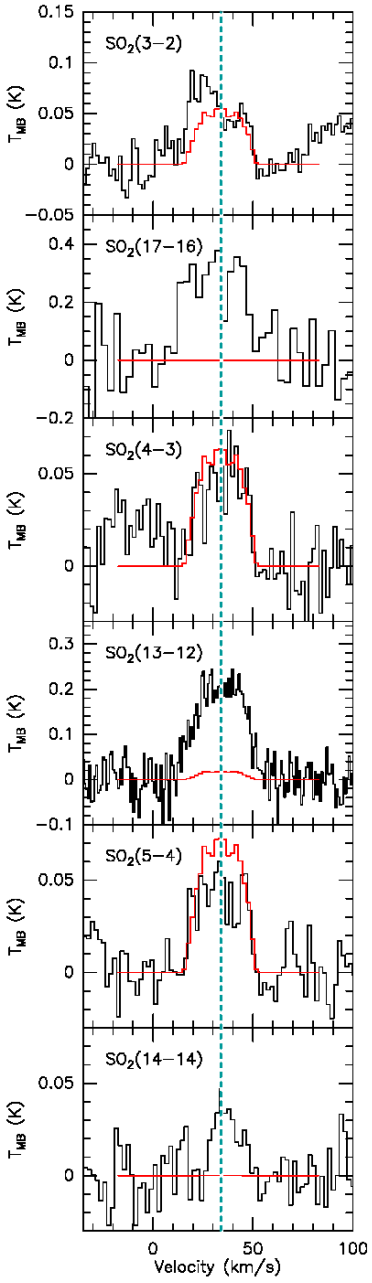

Figure 6.18.: Best model fits of the SO_2 transitions to the available set of data at offset (0″,0″) for IK Tau. SO_2 transitions are displayed. All temperatures are in T_{MB} units. Green dotted line indicates the stellar velocity of 33.7 km s^{-1}.

6.8. Summary

The molecules detected toward IK Tau using the APEX telescope were HCN, ^{12}CO, ^{13}CO, CS, CN, SiS, SiO, ^{29}SiO, ^{30}SiO, SO and SO_2. Also, maser lines were observed from H_2O, ^{28}SiO, ^{29}SiO and ^{30}SiO. By fitting the profiles of the molecular lines, we find that the FWHM linewidths of the thermal emission lines are distributed in the range from 20 $\mathrm{km\,s^{-1}}$ to 35 $\mathrm{km\,s^{-1}}$ and the derived expansion velocities are distributed in the range from 16 $\mathrm{km\,s^{-1}}$ to 21 $\mathrm{km\,s^{-1}}$. Characterized by their line shapes, some molecular lines show the parabolic shape of optically thick lines and others show the double-horn shape or the square shape of unresolved optically thin lines.

To estimate the spatial distribution of the ^{12}CO$(3-2)$ emission, mapping observations were performed. The radius of the spatial distribution at half-peak integrated intensity is $20''$ or 0.024 pc at the distance of IK Tau.

The rotational temperatures and the column densities of the detected molecules were estimated. Using the rotation temperatures, the fractional abundance of CO and SO_2 with respect to H_2 and the other species with respect to CO were obtained. The chemical modeling by Duari et al. (1999) can reproduce the observed abundances within a factor of 5. In particular, SiS is much lower than the observed values at $2.2R_*$ but is close to the observed value at $1R_*$ to $1.5R_*$, implying that SiS is produced deeper in the envelope than the other molecules. SO also shows a much lower value than the observed values at all radii. This means that this molecule is probably formed in the outer envelope of IK Tau. Comparing the averaged abundance of molecular transitions from this work and the literatures (Bujarrabal et al. (1994), Lindqvist et al. (1988) and Omont et al. (1993), see figure 6.19), the abundances of most molecules are close to the previous observed values except for the SiO and SO abundances. Since in our study low and high frequency lines are combined, one can expect that these results are more reliable than the previous ones.

H_2O maser lines at 321 GHz and 325 GHz were detected. The 321 GHz H_2O maser spectrum shows a single peak near the stellar velocity. The 325 GHz H_2O spectrum shows a broad emission profile shifted to the red with respect to the stellar velocity. The velocity spread of 321 GHz line is smaller than that of 325 GHz line because the emission region and maser pumping mechanism of these two maser lines are different. The 325 GHz transition has an excitation temperature of 470 K and the 321 GHz transition has a much higher excitation temperature of 1861 K. Therefore, the 321 GHz maser is excited closer to the central star. Furthermore, SiO masers were detected in the three main isotopic substitutions of SiO within different vibrational states. All lines are centered within a few $\mathrm{km\,s^{-1}}$ of the stellar velocity.

An extensive radiative transfer analysis of circumstellar CO and SO_2 was performed using a model with a power law structure in temperature and density and a constant expansion. Overall, the observed line profiles were fit very well by the model for the observed transitions (^{12}CO$(3-2)$, ^{13}CO$(3-2)$, ^{12}CO$(4-3)$, and ^{12}CO$(7-6)$). The line shapes and intensities in all ^{12}CO transitions were not influenced by variation of the inner radius, which is understandable since the bulk of the ^{12}CO emission is produced in the outer envelope. The intensities depend strongly on the assumed temperature for the higher transitions. Fits with different outer radii did not change the intensities of the higher transitions. Comparing the spatial distribution of the observations and the modeling result, the radius of half maximum was approximately identical with $20''$.

We found that the model fits well the $SO_2(3-2)$, $SO_2(4-3)$, and $SO_2(5-4)$ lines but not the higher excitation $SO_2(17-16)$, $SO_2(13-12)$, and $SO_2(14-14)$ lines. Hence, either the later three lines were misidentified as SO_2 lines or the extrapolation of collisional rates for the high excitation

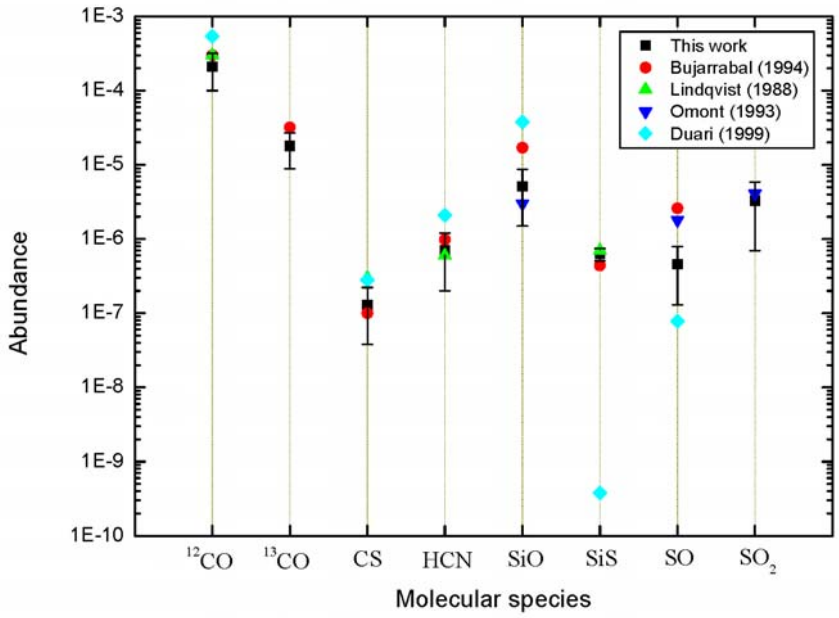

Figure 6.19.: Abundance comparison of this work to the literature (Bujarrabal et al. (1994), Lindqvist et al. (1988), Omont et al. (1993), and Duari et al. (1999)). The errors were estimated from the abundance variation with different transitions (see table 6.6). Abundances from the chemical models by Duari et al. (1999) used were selected at radius of $2.2R_*$ (5×10^{13} cm).

lines is not accuarate enough. Further observations of other highly excited SO_2 lines are needed to resolve this issue. The non-LTE model of SO_2 has an abundance of 5×10^{-6}, consistent with the range of abundances estimated using LTE (see table 6.6).

7. Conclusions

7.1. Dual-Mode Laser for a Photonic Local Oscillator in the Submillimeter Band

I have investigated the use of the Ti:Sapphire laser in order to generate two frequencies in the same laser for a photonic LO. To generate the dual-mode in the multi-mode laser, two intracavity Fabry-Perot solid etalons were installed. The thin etalon selected two colors, thus determining the expected difference frequency (i.e. the expected LO frequency). The thick etalon selected only one mode in the thin etalon transmission curve. Most modes were suppressed by mode competition. Finally, two modes separated by 100 GHz difference were selected. The output power was approximately 200 mW. The spectral width of the Ti:Sapphire laser beam was measured to be 12 kHz, adequate for submillimeter spectroscopy. The frequency stability, which is the FSR variation of the ring cavity, was measured to be 332 kHz when the room temperature changed by $\pm$ 1.3°C around 20 °C. The frequency drift (FSR change) was probably caused by thermal expansion of the cavity material. To observe the spectral width of the mixing product of two modes produced by the Ti:Sapphire laser, a 34 GHz mixing product was studied first, because the available maximum bandwidth of a commercial photodetector is around 50 GHz. From the observed spectrum, the spectral width of the 34 GHz beat frequency was $\sim$ 6 kHz at a resolution of 910 Hz and only one mode was transmitted through each overlapped transmission peak of the two etalon transmission curves combined. The 34 GHz beat frequency drift was $\sim$ 50 kHz maximum during three hours. The reason for the frequency drift was most likely thermal expansion of the etalons. A 100 GHz LO signal could be generated by illuminating a LT-GaAs photomixer with a tuned dual-mode Ti:Sapphire laser. The power of the 100 GHz radiation generated by the photomixer was measured by a Golay cell with horn antenna as a function of the applied bias voltage. A maximum power of 0.07 μW was obtained at a bias voltage of 7 V with an input laser power of around 35 mW. The beat frequency power as a function of applied bias voltage increased linearly with uncertainties of 20 %. The main reason for the errors was the continual peak intensity variation (approximately 10 dB fluctuations) between the modes caused by mode competition of the photons in the laser cavity and changes in the resonator condition due to air fluctuations, temperature variations and mechanical vibrations. To reduce these intensity fluctuations, a power stabilization system using VHGs was demonstrated. Without the stabilization system, the power difference between the two modes fluctuated by $\sim$ 10 dB with occasional 30 dB excursions. With the power stabilization system, fluctuations were greatly reduced to less than 3 dB except for a few events that were too fast for the servo system to react in time.

Future Improvements:

To reduce the frequency drift, the etalons should be made of a low thermal expansion material such as diamond for the solid etalon or a vacuum air-spaced etalon mounted in a holder made from low thermal expansion material such as Invar or Zerodur for the mode selection components. To reduce

the intensity fluctuations, a power stabilization system should be considered with, for example, a thermally stabilized box.

Outlook:

Although the present Ti:Sapphire ring cavity laser is difficult to use at frequencies above 100 GHz, because the adjacent resonator modes are so close together, its broad gain profile and its high gain make it still attractive as a two frequency source for a photonic LO. Unlike with diode lasers an additional optical amplifier is not needed. The spectral width is narrow enough to adopt for use in submillimeter spectroscopy. However, the stability of the frequency and power are sensitive to external factors such as thermal fluctuations, mechanical vibrations, and air fluctuations.

For the fixed LO source at a frequency as low as 100 GHz, the laser power is sufficient to generate the beat frequency using a LT-GaAs photomixer. However, for a tunable LO source from a few hundreds of GHz to a few THz band, the dual-mode laser using the Ti:Sapphire ring cavity laser is not useful. The output powers of the dual-mode at frequencies higher than 200 GHz decreases exponentially because the two modes exist at the edge of the transmission curve of the birefringent filter. Because the photomixer conversion efficiency also decreases with frequency, in the above setup we could not generate enough beat frequency power for SIS mixer operating.

For LO frequencies higher than 100 GHz (even into the THz region) another concept with a shorter cavity may be tried in order to obtain a suitable and larger mode separation. However a smaller cavity may result in wider lines.

To build a photonic LO at such high frequencies, a tunable diode laser with an amplifier might be useful candidate. The disadvantages of the diode laser are the poor frequency stability and the linewidth is roughly 1 MHz with an integration time of 1 s. However, these disadvantages may be improved by the laser stabilization system using an optical frequency comb generator (OFCG).

The photonic LO will be implemented in an upgraded version of FLASH, operating at 1 THz. This making, however, was outside the scope of this PhD work.

7.2. The Molecular Composition of an Oxygen-Rich Asymptotic Giant Branch Star

Thermally excited spectral lines from 27 transitions of 11 molecular species were observed with the APEX telescope toward IK Tau. Maser lines of H_2O at 321 GHz and 325 GHz, and ^{28}SiO, ^{29}SiO and ^{30}SiO were also observed.

The fractional abundances of CO with respect to H_2 and the other species with respect to $^{12}CO(1-0)$ were determined and compared to existing chemical models. The improved abundance estimates of this study will allow refinements of the chemical models in the future.

An extensive radiative transfer analysis of circumstellar CO and SO_2 has been performed. A model using a power law structure for the density and temperature fits our CO observations very well and can reproduce the lower energy lines of SO_2. The bulk of the $^{12}CO(1-0)$ emission is produced further out in the envelope than emission from higher transitions.

This study shows that IK Tau is a good laboratory to study the conditions in circumstellar envelopes around oxygen-rich stars with submillimeter-wavelength molecular lines.

Outlook:

IK Tau's circumstellar envelope contains a plethora of molecules whose moderate to higher excitation transitions can be observed at submillimeter wavelengths. Apart from many C- and O-containing molecules, IK Tau shows a remarkably high abundance of S-bearing molecules, whose chemistry strongly depends on temperature through its connection with the oxygen chemistry.

Molecular line modeling predicts the abundance of each molecule as a function of radial distance from the star. Therefore, to get a clearer picture of the chemistry, mapping observations for molecules other than CO should be performed. Since most of the submillimeter emission from less abundant molecules probably arises from the inner part of the envelope at 2 – 4″ (except CO) meaningful observations require interferometers such as the future Atacama Large Millimeter Array (ALMA).

A. The Transmitted Intensity of the Fabry-Perot Interferometer

The multiple output beams differ in phase due to the different path lengths traversed by each of the beams. The optical phase acquired by the light on one round trip through the etalon is given by,

$$\phi = 4\frac{\pi nd\cos(\theta)}{\lambda} \tag{A.1}$$

where ϕ is the optical path difference of neighboring transmitted rays, θ is the angle of incidence in the etalon, λ is the wavelength and d is the physical cavity thickness and n is the index of refraction. The amplitude of each of the transmitted waves can thus be written (see figure 2.7),

$$A_1 = tt'A_i, \qquad A_2 = tt'r'^2e^{i\phi}A_i, \qquad A_3 = tt'r'^4e^{2i\phi}A_i, ... \tag{A.2}$$

The sum of transmitted wave amplitudes, A_t is

$$A_t = A_i tt'(1 + r'^2e^{i\phi} + r'^4e^{2i\phi} + ...) = \frac{tt'}{1 - rr'e^{i\phi}}A_i \tag{A.3}$$

The fractional output intensity, $T = \frac{I_t}{I_i}$ (I_t is the transmitted intensity and I_i is the incident intensity) from an ideal etalon is given by

$$T = \frac{I_t}{I_i} = \frac{A_tA_t^*}{A_iA_i^*} = \frac{(tt')^2}{(1 - rr')^2 + 4\sqrt{rr'}\sin^2(\phi/2)} \tag{A.4}$$

where the power reflectivity $R = r^2$ in a lossless system with $r = r'$, with lossless interfaces $r^2 + t^2 = 1$.

Therefore the transmitted intensity is

$$I = I_0\frac{(1 - R_1)(1 - R_2)}{(1 - \sqrt{R_1R_2})^2 + 4\sqrt{R_1R_2}\sin^2(\phi/2)} \tag{A.5}$$

where I is the transmitted intensity (same as I_t), I_0 is the incident intensity (same as I_i) when the ray was transmitted through different refraction index etalon on the both surfaces. R_1, R_2 are the reflectances of the mirror surfaces.

B. Chemical Chains of the Detected Molecules

Chemical formation chains of molecules were investigated by Cherchneff (2006) and Duari & Hatchell (2000). The pathways for the detected molecules are the following. Carbon monoxide is formed from the trimolecular reaction and the bimolecular process.

$$C + O + M \rightarrow CO + M \tag{B.1}$$

$$C + OH \rightarrow CO + H. \tag{B.2}$$

CS is formed via the destruction of CO

$$CO + S \rightarrow CS + O \tag{B.3}$$

SiO is linked to presence of the hydroxyl radial OH,

$$Si + OH \rightarrow SiO + H \tag{B.4}$$

The chemical processes responsible for the formation of HCN involve reactions with cyanogens. HCN is formed by the reaction

$$CN + H_2 \rightarrow HCN + H \tag{B.5}$$

CN acts as an intermediary in the formation of HCN and CS and is destroyed quickly by atomic hydrogen. The reaction is sensitive to temperature. CN is forming by the following routes

$$N + CH \rightarrow CN + H \tag{B.6}$$

$$N + CS \rightarrow CN + S \tag{B.7}$$

The parent H_2S is photodissociated to HS and thence to S and S^+. Both react with oxygen-bearing molecules such as OH and O_2. For $r < 10^{17}$ cm, SO is formed by a trimolecular reaction and a bimolecular reaction

$$S + O + M \rightarrow SO + M \tag{B.8}$$

$$S + CO \rightarrow SO + C \tag{B.9}$$

Towards lower gas temperatures the dominant formation process is

$$S + OH \rightarrow SO + H. \tag{B.10}$$

and destroyed by reaction with OH to form SO_2

$$SO + OH \rightarrow SO_2 + H. \tag{B.11}$$

The chemistry of silicon sulfide SiS is linked to hydrogen sulfide HS and Si

$$\mathrm{Si} + \mathrm{HS} \rightarrow \mathrm{SiS} + \mathrm{H} \tag{B.12}$$

$$\mathrm{Si} + \mathrm{S} + \mathrm{M} \rightarrow \mathrm{SiS} + \mathrm{M} \tag{B.13}$$

C. Rotation Diagrams

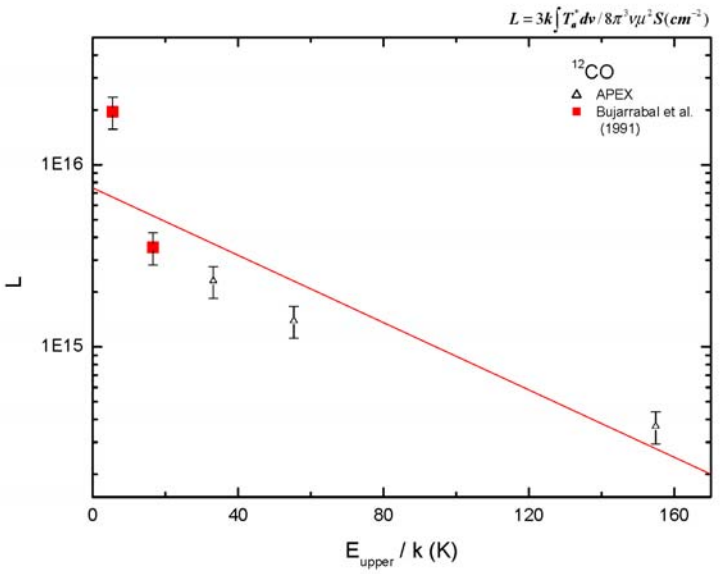

Figure C.1.: The rotation diagram of the ^{12}CO molecule.

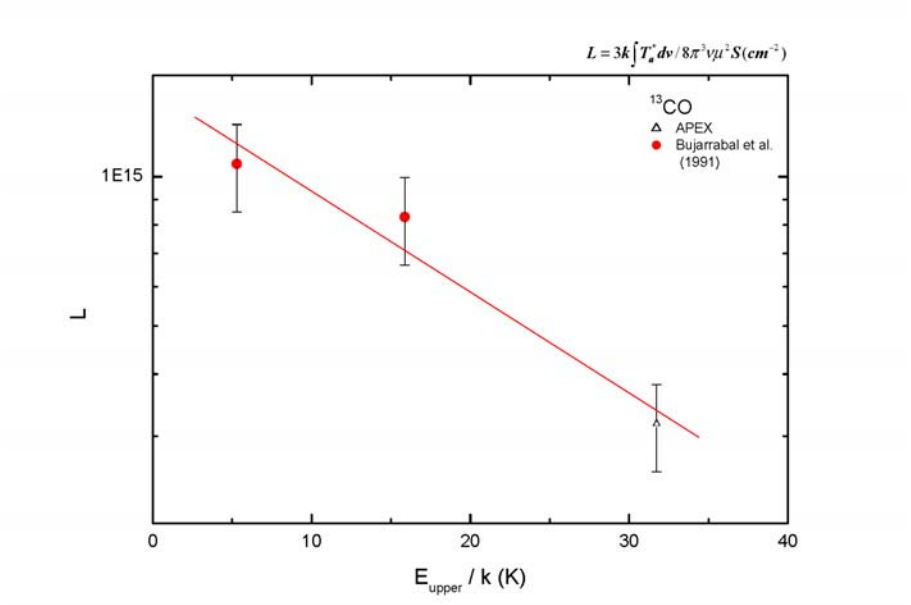

Figure C.2.: The rotation diagram of the ^{13}CO molecule.

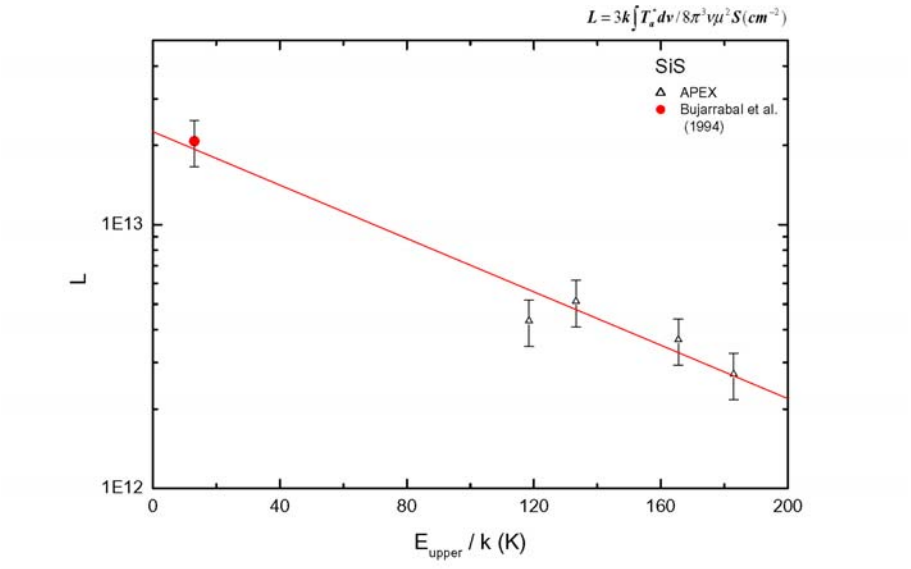

Figure C.3.: The rotation diagram of the SiS molecule.

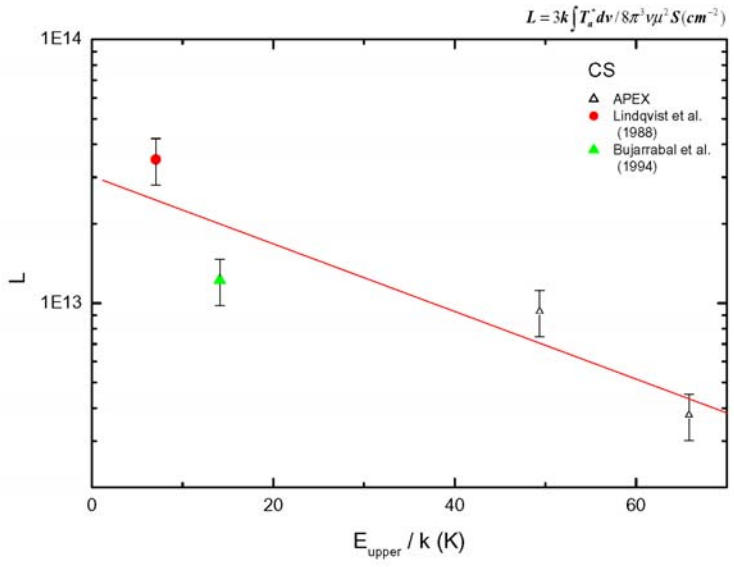

Figure C.4.: The rotation diagram of the CS molecule.

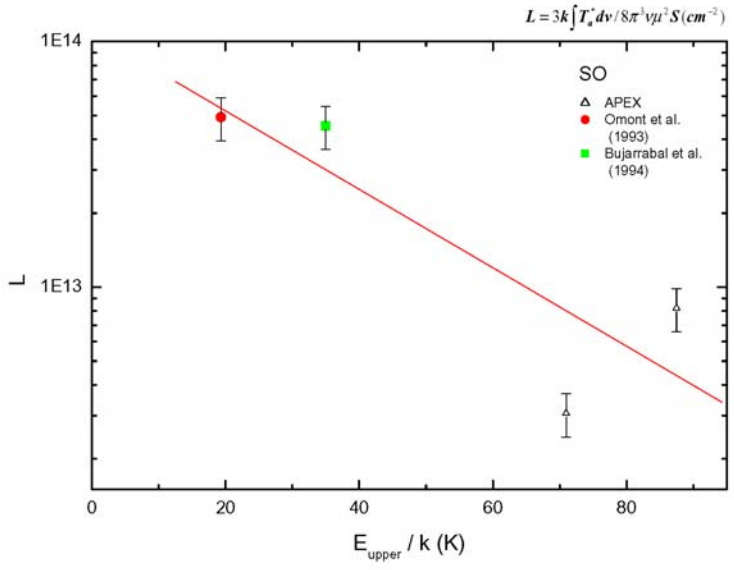

Figure C.5.: The rotation diagram of the SO molecule.

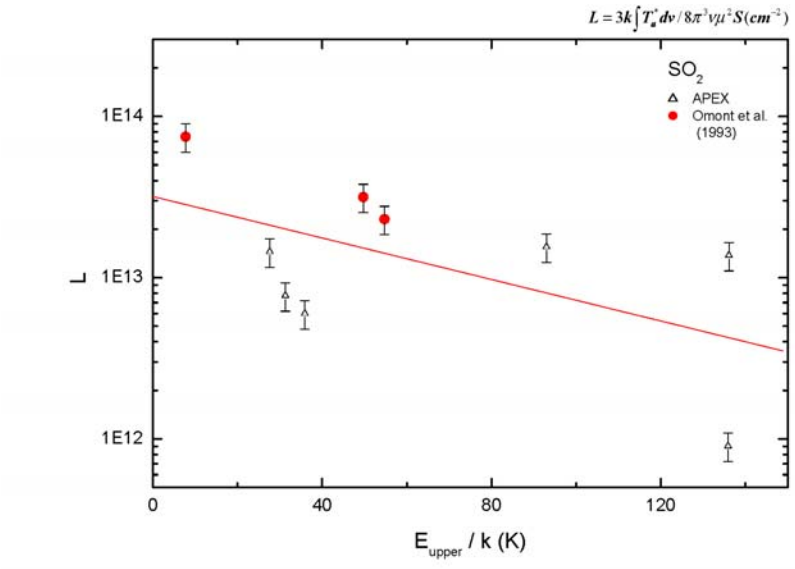

Figure C.6.: The rotation diagram of the SO_2 molecule.

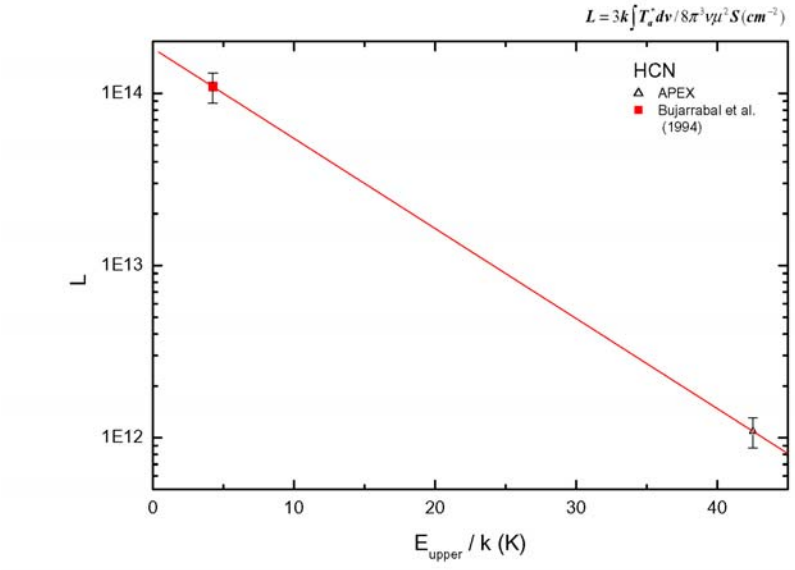

Figure C.7.: The rotation diagram of the HCN molecule.

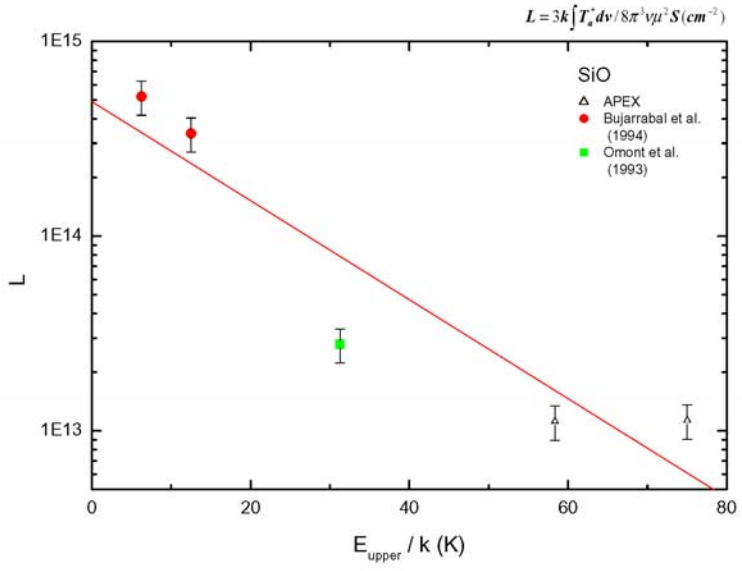

Figure C.8.: The rotation diagram of the SiO molecule.

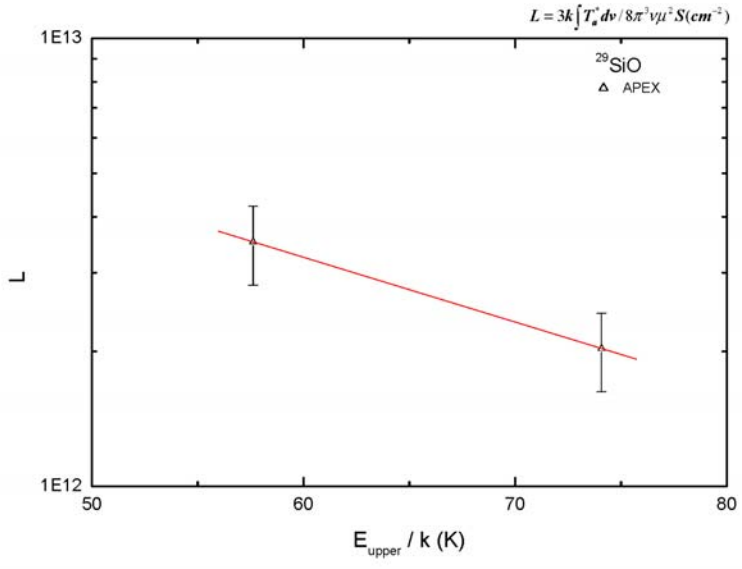

Figure C.9.: The rotation diagram of the ^{29}SiO molecule.

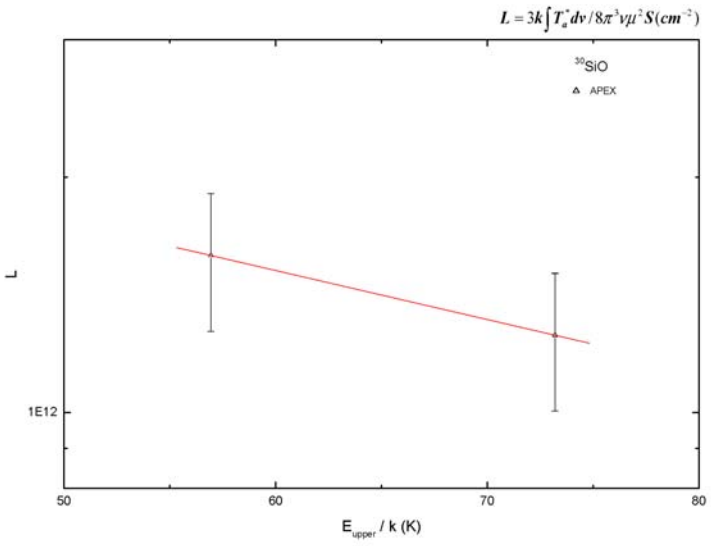

Figure C.10.: The rotation diagram of the ^{30}SiO molecule.

D. Opacities of the Molecular Lines

The intensity of a molecular line strongly depends on its excitation temperature and the molecule′s column density. To know how excitation temperature and column density influence the opacities, I calculated the opacities for each individual molecular line. This procedure is based on the guide of RADEX (van Langevelde & van der Tak 2004) and the opacities were obtained using RADEX, a statistical equilibrium radiative transfer code.

In LTE we assumed that the level populations are governed by the Boltzmann equation and are thus independent of the density. The optical depth in LTE is given by

$$\tau_\nu = \frac{c^2}{8\pi\nu^2} n_1 \frac{g_2}{g_1} A_{21} (1 - e^{-\frac{h\nu}{kT}}) \phi_\nu(v) \Delta s \tag{D.1}$$

where n_1 is the volume density of molecule in the lower state of the transition, g_1 and g_2 are statistical weight of molecule in the lower and upper state of the transition, A_{21} is the Einstein coefficient and $\phi_\nu(v)$ is $1/\Delta\nu$. Δs is N/n (where N is the column density and n is the volume density in the upper or lower state of the transition).

The main beam brightness temperature for unify filling factor is

$$T_{\mathrm{MB}} = T_{\mathrm{ex}} (1 - e^{-\tau}), \tag{D.2}$$

if we neglect the cosmic microwave background.

Figures D.1 to D.12 shows the opacities and the main-beam brightness temperatures of the molecules.

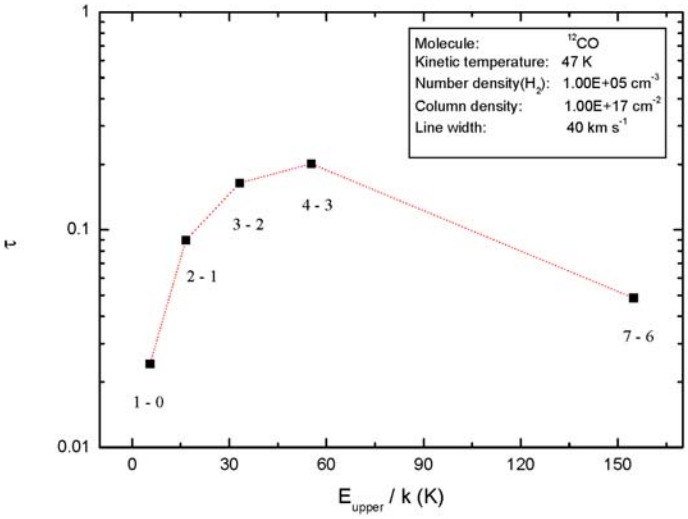

Figure D.1.: The opacities of the ^{12}CO molecule.

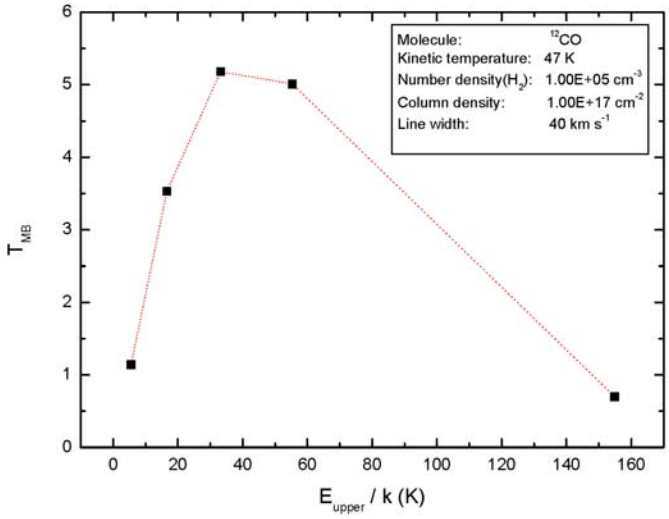

Figure D.2.: Main-beam brightness temperature of the ^{12}CO lines.

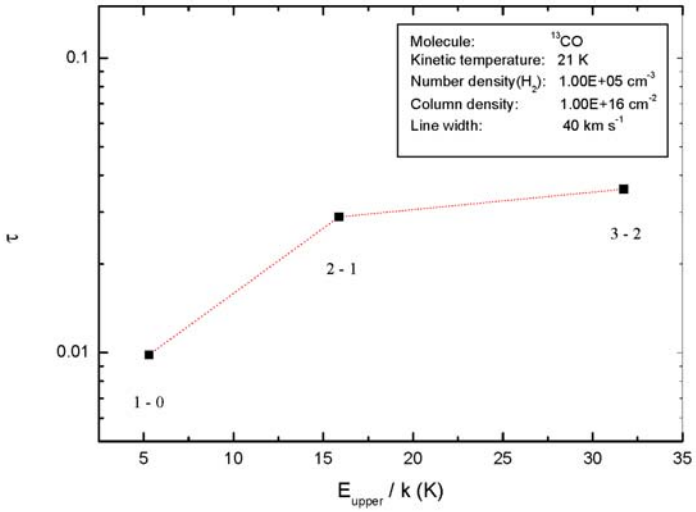

Figure D.3.: The opacities of the ^{13}CO lines.

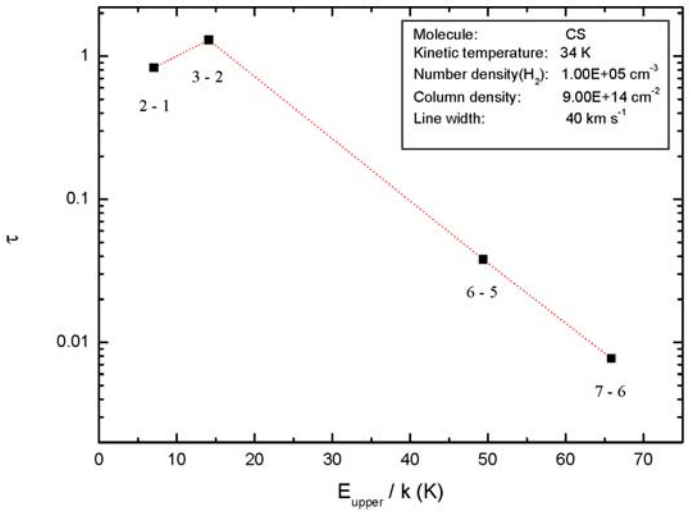

Figure D.4.: The opacities of the CS lines.

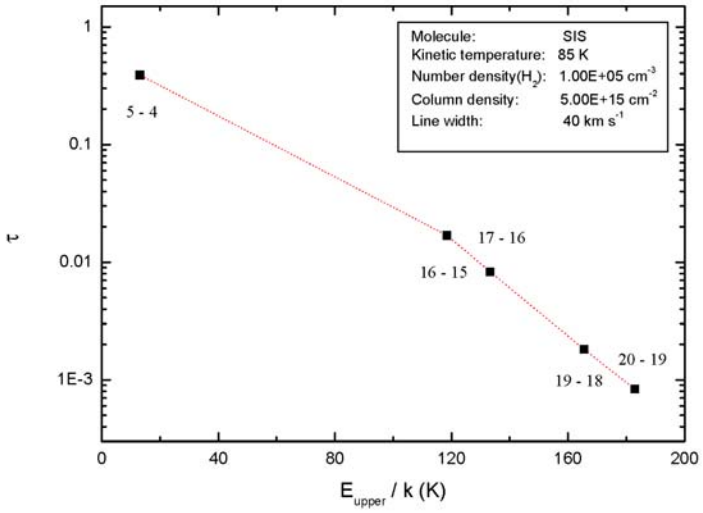

Figure D.5.: The opacities of the SiS lines.

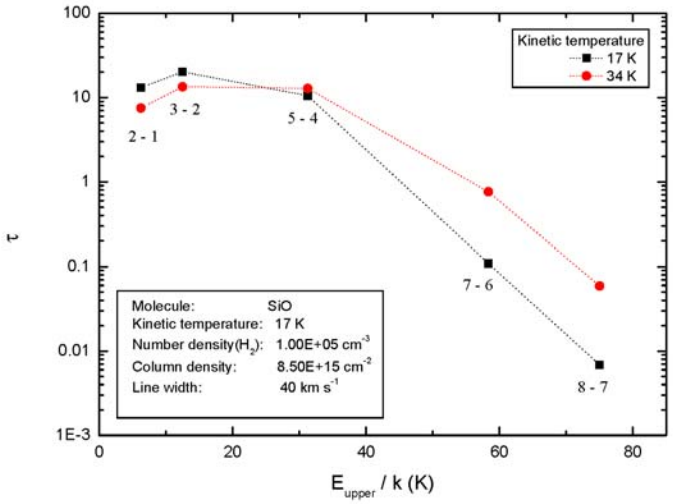

Figure D.6.: The opacities of the SiO lines.

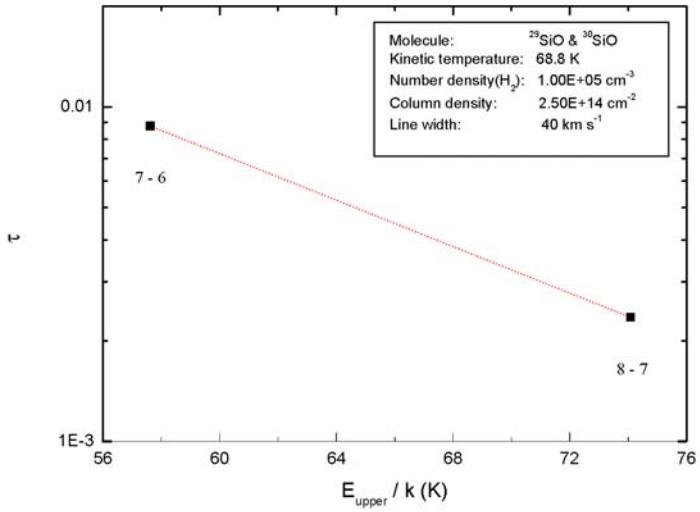

Figure D.7.: The opacities of the ^{29}SiO lines.

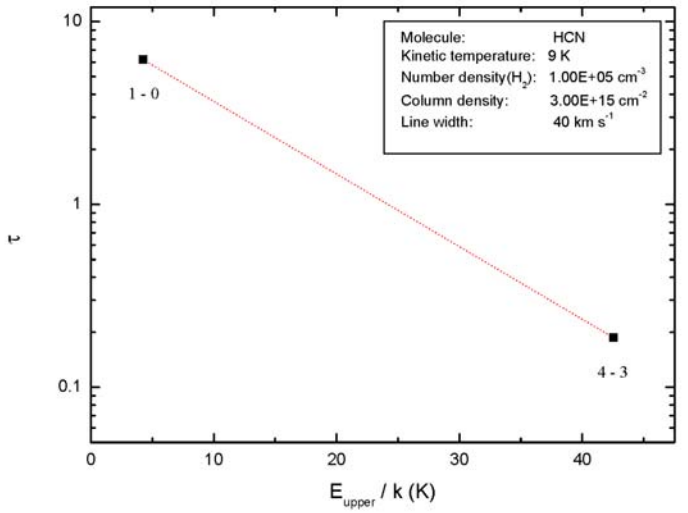

Figure D.8.: The opacities of the HCN lines.

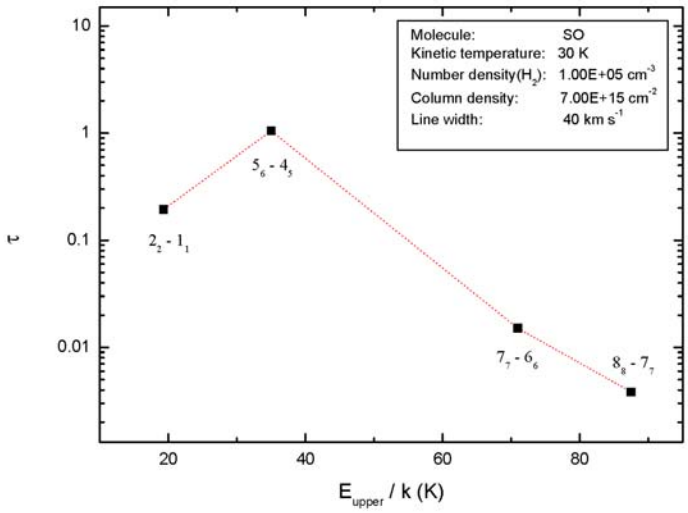

Figure D.9.: The opacities of the SO lines.

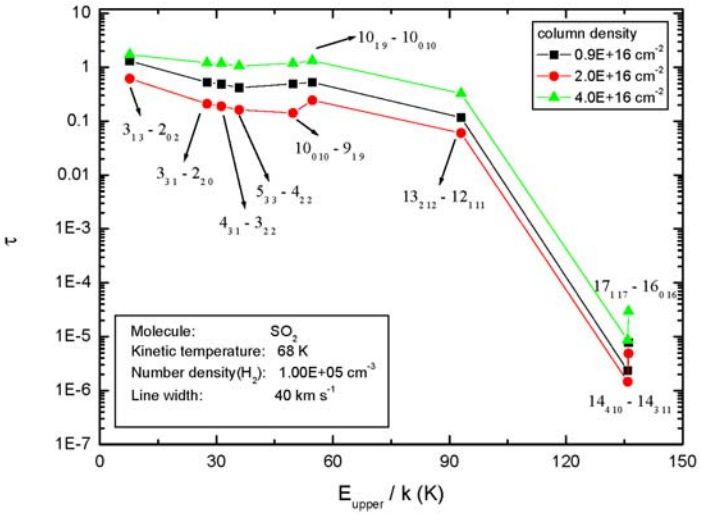

Figure D.10.: The opacities of the SO_2 lines.

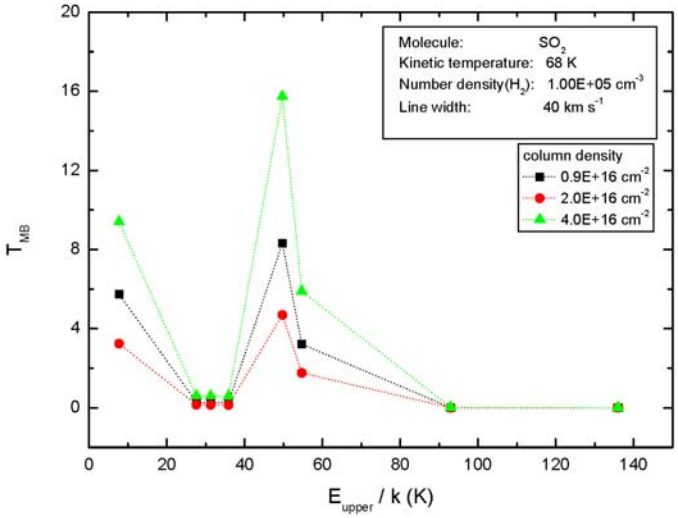

Figure D.11.: Main-beam brightness temperature of the SO_2 lines with the different column densities.

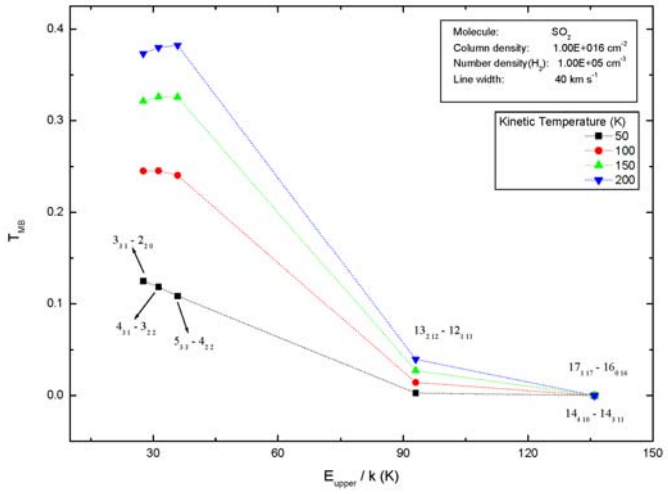

Figure D.12.: Main-beam brightness temperature of the SO_2 lines with the different kinetic temperatures.

Bibliography

Adam, R., Mikulics, M., Wu, S., et al. 2004, Proceedings of SPIE, 5352, 321 45
Alcolea, J. 2004, Proceedings of 7th European VLBI Network Symposium 81
Alcolea, J., Pardo, J., & Bujarrabal, V. 1999, ApJ, 139, 461 60
Alfrey, A. 1989, IEEE Quantum electronics, 25, 760 34
Backus, S., Durfee, C., Murnane, M., & Kapteyn, H. 1998, Rev.Scientific Instruments, 69, 1207 11
Benson, P. & Little-Marenin, I. 1996, ApJ, 106, 579 80
Bernes, C. 1979, A&*A*, 73, 67 83
Berthold, J., Jacobs, S., & Norton, M. 1977, Metrologia, 13, 9 41
Biebersdorf, A., Lingk, C., De Giorgi, M., et al. 2003, Applied Physics, 36 33
Blais-Ouellette, S., Daiglea, O., & Taylor, K. 2006, www.photonetc.com 50
Blake, G., Sutton, E., Masson, C., & Phillips, T. 1987, ApJ, 315, 621 72
Boboltz, D. & Diamond, P. 2005, A&A, 625, 978 60
Bowers, P. E., Johnston, K. J., & de Vegt, C. 1989, ApJ, 340, 479 60
Brown, E., McIntosh, K., Smith, F., Manfra, M., & Dennis, C. 1993a, American Institute of Physics, 62, 1206 43
Brown, E., Smith, F., & McIntosh, K. 1993b, Journal of Applied Physics, 73, 1480 45, 48
Bujarrabal, V. & Alcolea, J. 1991, ApJ, 251, 536 69, 75, 78
Bujarrabal, V., Fuente, A., & Omont, A. 1994, ApJ, 285, 247 60, 74, 75, 76, 91, 92
Carlstrom, J. & Zmuidzinas, J. 1996, The Oxford University press 3
Cerullo, G. & Nisoli, M. 2001, Springer 8
Cherchneff, I. 2006, A&A 99
Crosas, M. & Menten, K. 1997, ApJ, 483, 913 84
Davis, C. 1996, Cambridge university press 9
Demtröder, W. 1996, Springer-Verlag, Germany 8, 9, 10, 14
Diamond, P.J. aand Kemball, A., Junor, W., et al. 1994, ApJ, 430, L61 81
Doric, S. & Neron, J. 2005, Doric Lenses Inc. 16, 18
Duari, D., Cherchneff, I., & Willacy, K. 1999, ApJ. Letter, 341, L47 74, 76, 77, 91, 92
Duari, D. & Hatchell, J. 2000, A&A, 358, L25 99
Forveille, T., Guilloteau, S., & Lucas, R. 1989, Grenoble, IRAM 61
Fukasaku, S., Hirahara, Y., Masuda, A., et al. 1994, ApJ., 437, 410 57
Gehrz, R. 1989, Kluwer Academic Publishers, Dordrecht 59
Glassgold, A. 1996, Annu. Rev. ApJ, 34, 241 58, 59
Goldreich, P. & Scoville, N. 1976, ApJ, 205, 144 58
Green, S. 1995, ApJS, 100, 213 89
Güsten, R., Nyman, L., Schilke, P., et al. 2006, A&A 61

Habing, H. 1996, A&A Rev., 7, 97 58
Habing, H. & Olofsson, H. 2003, Springer 57, 60, 73
Hale, D. et al. 1997, ApJ, 490, 411 60
Havermeyer, F., Liu, W., Moser, C., et al. 2004, Optical Engineering, 43, 2017 49, 50
Herwig, F. 2005, Annu. Rev. Astron. Astrophys., 43, 435 58
Heyminck, S., Kasemann, C., Güsten, R., et al. 2006, A&A, 5413 2, 4, 61
Hogerheijde, M. & van der Tak, F. 2000, ApJ, 362, 697 83
Houwman, E., Godfried, H., Hall, C., et al. 2006, http://www.e6.com 41
Hsieh, H., Panotopoulos, G., Liger, M., et al. 2004, IEEE Photonics technology letters, 16, 177 49
Hyodo, M., Tani, M., Matsuura, S., Onodera, N., & Sakai, K. 1996, Electronics Letters, 32, 1589 33
Iocco, A., Limberger, H., Salathe, R., et al. 1999, J. Lightwave Technol., 17, 1217 49
Jackel, J. 1996, J. Lightwave Technol., 14, 1056 49
Johansson, L., Hu, Z., Blumenthal, D., et al. 2005, IEEE Photonics Technology Letters, 17, 285 33
Knapp, G. R. & Morris, M. 1985, ApJ., 292, 640 60, 74
Lane, A., Johnston, K., Bowers, P., et al. 1987, ApJ, 323, 756 60, 79
Lattanzio, J. 2002, New Astronomy Reviews, 46, 469 57, 58
Lattanzio, J. & Frost, C. 1997, IAU Symposium, Proc., 189 57
Lequine, M., Parmentier, R., Lemarchand, F., & Amra, C. 2002, Appl. Opt., 41, 3277 49
Lindqvist, M., Nyman, L.-A., Olofsson, H., & Winnberg. 1988, ApJ, 205, L15 60, 74, 75, 76, 91, 92
Lucas, R., Bujarrabal, V., Guilloteau, S., et al. 1992, ApJ, 262, 491 69
Marvel, K. 2005, A&A, 130, 261 69
Mayorga, I., Mikulics, M., Schmitz, A., et al. 2004, Proceedings of SPIE, 5498, 537 45
McIntosh, K., Brown, E., Nichols, K., et al. 1995, Applied Physics Letters, 67, 3844 43
Menten, K. 1996, ASPC, 93, 79M 80
Menten, K. & Young, K. 1995, ApJ, 450, L67 80
Meschede, D. 2004, Wiley-VCH 19, 20, 22
Mikulics, M. 2004, PhD thesis, Aachen 45
Mollaaghababa, R., Gottlieb, C. A., Vrtilek, J. M., & Thaddeus, P. 1991, ApJ. Lett., 368, L19 81
Morris, M., Guilloteau, S., Lucas, R., & Omont, A. 1987, ApJ, 321, 888 74
Moulton, P. 1982, Opt. News, 8, 9 11, 22
Olofsson, H., Lindqvist, M., Nyman, L., & Winnberg, A. 1998, A&A, 329, 1059 60
Olofsson, H., Lindqvist, M., Nyman, L.-A., et al. 1991, ApJ, 245, 611 73
Omont, A., Lucas, R., Morris, M., & Guilloteau, S. 1993, ApJ, 267, 490 60, 74, 75, 76, 91, 92
Ondax. 2006, Ondax Inc. http://www.ondax.com 49
Photonics. 2006, Precision Photonics Corporation 18
Reilly, S., James, S., & Tatam, R. 2002, Electron. Lett., 38, 1033 7
Roy, R., Agrawal, D., & McKinstry, H. 1989, Annu. Rev. Mater. Sci., 19, 59 41
RPPhotonics. 2006, http://www.rp-photonics.com/coherence_time.html 8
Schöier, F. L., van der Tak, F. F. S., van Dishoeck, E. F., & Black, J. H. 2005, A&A, 432, 369 89
Siegman, A. 1986, University Science Books 10, 11
Stone, J. & Stulz, L. 1987, Electron. Lett., 23, 781 49

Stone, M., Naftaly, M., Miles, E., et al. 2005, App. Physics, 97, 151 33
Tani, M., Gu, P., Hyodo, M., et al. 2004, Optical and Quantum Electronics, 32, 503 7
Tani, M., Morikawa, O., Matsuura, S., & Hangyo, M. 2005, Semicond. Sci. Technol., 20, 151 33, 43
Teyssier, D., Hernandez, R., Bujarrabal, V., et al. 2006, A&A, 450, 167 74, 81, 83, 84, 86
Tsuji, T. 1964, Annals of the Tokyo Astronomical Observatory, 9, 1 59
Tsuji, T. 1973, A&A, 23, 411 59
Vail, E. 1995, Electron. Lett., 31, 228 49
van der Tak, F., Boonman, A., Braakman, R., & van Dishoeck, E. 2003, A&A, 412, 133 83, 89
van Langevelde, H. & van der Tak, F. 2004, A guide of RADEX 107
Verdeyen, J. 1995, Prentic Hall Series in Solid State Physical Electronics, New Jersey 13
Vlemmings, W. & van Langevelde, H. 2005, A&A, 434, 1021 79
Wang, J., Omori, T., Sutou, Y., et al. 2004, ELECTRONIC MATERIALS, 33, 1098 41
Watanabe, T., Inoue, Y., Kaneko, K., et al. 1997, Electron. Lett., 33, 1547 49
Willacy, K. & Millar, T. 1997, A&A, 324, 237 60
Wing, R. & Lockwood, G. 1973, ApJ, 184, 873 60
Wyrowski, F., Walmsley, C. M., Natta, A., & Tielens, A. G. G. M. 1997, A&A, 324, 1135 5
Yamamura, I., Onaka, T., Kamijo, F., et al. 1996, ApJ., 465, 926 57
Yang, S., Hammacks, A., Fogler, M., & Butov, L. 2006, cond.mat 9
Yates, J., Cohen, R., & Hills, R. 1995, MNRAS, 273, 529 80
Zimmermann, C., Vuletic, V., Hemmerich, L., & Hansch, T. 1995, Optics Letter, 20, 297 7, 33
Zuckerman, B. 1987, IAUS, 120, 345 69

Acknowledgements

This thesis was written at the Max-Planck Institute for Radioastronomy, in the Heterodyne Receiver Division of the Millimeter and Submillimeter Astronomy group.

First of all, I sincerely would like to appreciate to Prof. Kar M. Menten for giving me the opportunity to work in the Millimeter and Submillimeter Astronomy Group. Without this opportunity, this work would not have been possible. I would also like to thank Dr. Rolf Güsten for giving me the opportunity to work in the Heterodyne Receiver Division. Many thanks go to my advisor Friedrich Wyrowski, for his kind help, guidance, and support throughout my astronomy study. Without his guidance, I would never have finished my thesis. I would also like to thank Peter van der Wal and Stefan Heyminck for providing technical advice. Peter was so kind to help me to repair my broken English. I would also like to thank Andreas Schmitz and Ivan Camara for kindly cooperation on experiments.

I am grateful to Prof. Frank Bertoldi for having consented to be the referee for my thesis. I am also grateful to Prof. Herbert Hübel (Nuclear Physics Department) and Prof. Clemens Simmer (Meterology Department), for having agreed to read my thesis.

There are many people warmly supported me during these three years. Fist of all, many thanks go to Alan Roy, for his kind help, English correction for my thesis, advice for my work. His suggestions and comments on the text were helped to improve my writing skills. I would like to thank to Frau Lahr-Nilles, Frau Lewinsky, and Frau Fingas. They were so kind to help me for all admistration work. I thank Nikhil, Jan, Anu for cheering me up during the breaks and Thushara for her kindly help when I had some questions about the modeling program. I am grateful to Rupal and Martin, for cheering and being a good company during the break. As a good friend, many thanks go to Peter (Erni), for kindly advices for the LaTex and trying to show me the right way for life. A lot of thanks go to my friends in Korea for persistently cheering for me up. They are my precious in my life.

Finally, I would like specially to thank my dear parent, my brothers, sister, sister-in-law for their support and understanding through my PhD.